

**OXIDATION RESISTANCE, THERMAL  
CONDUCTIVITY, AND SPECTRAL EMITTANCE  
OF FULLY DENSE ZIRCONIUM DIBORIDE WITH  
SILICON CARBIDE AND TANTALUM DIBORIDE  
ADDITIVES**

A Thesis  
Presented to  
The Academic Faculty

by

Gregg Thomas Van Laningham

In Partial Fulfillment  
of the Requirements for the Degree  
Doctor of Philosophy in the  
School of Materials Science and Engineering

Georgia Institute of Technology  
May 2012

**OXIDATION RESISTANCE, THERMAL  
CONDUCTIVITY, AND SPECTRAL EMITTANCE  
OF FULLY DENSE ZIRCONIUM DIBORIDE WITH  
SILICON CARBIDE AND TANTALUM DIBORIDE  
ADDITIVES**

Approved by:

Professor Robert F. Speyer,  
Advisor  
School of Materials Science and  
Engineering  
*Georgia Institute of Technology*

Professor Rosario Gerhardt  
School of Materials Science and  
Engineering  
*Georgia Institute of Technology*

Professor Thomas H. Sanders  
School of Materials Science and  
Engineering  
*Georgia Institute of Technology*

Professor George Kardomateas  
School of Aerospace Engineering  
*Georgia Institute of Technology*

Professor W. Brent Carter  
School of Materials Science and  
Engineering  
*Georgia Institute of Technology*

Date Approved: 9 January 2012

*I have met many wonderful people over the course of the past few years who have shared freely their copious knowledge with me, and who have shown patience and kindness to me. The lessons I take from them and this degree program extend far beyond these pages, and I am very grateful to all who have been a part of my life thus far.*

*There are three individuals, however, whom I am no longer able to thank in person, but without whose wisdom and tutelage my learning would be even more incomplete:*

*Dr. Elizabeth A. Judson*

*Mr. Robert E. Allison, III*

*and*

*Dr. Robert L. Snyder*

*This work is dedicated to their memory.*

## ACKNOWLEDGEMENTS

I would like to thank my advisor, Dr. Robert Speyer, whose guidance has been invaluable to me, and without whom this work would not have happened. Additional thanks go out to my committee members, each of whom has contributed greatly to the quality of my education and this work. I would also like to thank my friends and colleagues: Dr. Fei Peng, Dr. NamTae Cho, Dr. Lionel Vargas, Dr. Charles Schenck Wiley, Rebecca Erdman, Kathleen Silver, John Shupe, and David Greenlee; their helpfulness and kindness have known no bounds. In addition, my sincere gratitude is extended to Yolande Berta, a very generous soul.

My deepest thanks are extended to my family, and to my friends who have become family. My mom and dad have always believed in me, and I am grateful for their unwavering support. My twin sister Katie has always been by my side, and my little sister Kimberly is a joy of my life. My grandmother is an inspiration to me, and a source of great wisdom. Finally, there is no question that I would be lost in this world were it not for my best friends: Qate Bean, Nick Simmons, Jim Amato, and Mark Luell. I love you all.

This list is incomplete, and I apologize to the many deserving people who have gone unmentioned above. I am keenly aware, however, that the goodness in my life comes directly from the goodness of the people within it, and I thank you, kind reader, if you have been one of them.

# TABLE OF CONTENTS

DEDICATION . . . . .	iii
ACKNOWLEDGEMENTS . . . . .	iv
LIST OF TABLES . . . . .	vii
LIST OF FIGURES . . . . .	viii
SUMMARY . . . . .	xvi
<b>I INTRODUCTION . . . . .</b>	<b>1</b>
<b>II LITERATURE REVIEW . . . . .</b>	<b>5</b>
2.1 Densification . . . . .	6
2.2 Oxidation . . . . .	8
2.2.1 Protective Oxide Layer . . . . .	8
2.2.2 Environmental Effects . . . . .	13
2.2.3 Transition Metal Boride Additions . . . . .	15
2.2.4 High Temperature Study . . . . .	17
2.3 Heat Transfer . . . . .	18
2.3.1 Thermal Conductivity . . . . .	19
2.3.2 Emittance . . . . .	23
<b>III THERMOGRAVIMETRIC STUDY OF ZRB<sub>2</sub>-BASED CE- RAMIC COMPOSITES . . . . .</b>	<b>27</b>
3.1 Experimental Procedure . . . . .	27
3.2 Results and Discussion . . . . .	35
3.3 Discussion . . . . .	39
3.4 Conclusions . . . . .	42
<b>IV DETERMINATION OF THERMAL CONDUCTIVITY OF ZRB<sub>2</sub>-BASED CERAMIC COMPOSITES . . . . .</b>	<b>59</b>
4.1 Experimental Procedure . . . . .	59
4.2 Results and Discussion . . . . .	61

4.3	Conclusions . . . . .	69
<b>V</b>	<b>MEASUREMENT OF EMITTANCE OF ZRB<sub>2</sub>-BASED CERAMIC COMPOSITES . . . . .</b>	<b>75</b>
5.1	Experimental Procedure . . . . .	75
5.2	Results and Discussion . . . . .	79
5.3	Conclusions . . . . .	82
<b>VITA</b>	<b>. . . . .</b>	<b>105</b>

## LIST OF TABLES

1	Raw Material Characteristics for Oxidation Specimens . . . .	27
2	Sample Compositions for Oxidation Specimens . . . . .	28
3	Sample Compositions for Thermal Diffusivity Specimens . . .	59
4	Raw Material Characteristics for Emittance Specimens . . . .	75
5	Sample Composition for Emittance Specimens . . . . .	75

## LIST OF FIGURES

1	Diagram showing the substantial barrier layer formed by a blunt body such as NASA’s Space Shuttle moving at supersonic speed during atmospheric reentry. . . . .	6
2	Phase diagram of the Zr-B system including non-equilibrium high-temperature phases. . . . .	9
3	SEM micrograph of cross section of ZrB <sub>2</sub> -10 vol% B <sub>4</sub> C heat treated in flowing air to 1460°C. Rectangles enclose regions where EDS performed; elements detected are listed next to each rectangle. 30 μm thick zirconium oxide scale is non-protective	13
4	SEM micrograph of cross section of ZrB <sub>2</sub> -28 vol% SiC having undergone oxidation. Note the layered structure: silicate glass over SiC-depleted zone over unreacted bulk. . . . .	14
5	Isothermal mass change with varying vol% additions of TaB <sub>2</sub> . Note that the parabolic behavior at 1200 and 1400°C is not observed at 1500°C. . . . .	18
6	Photograph of samples after oxyacetylene torch testing. Left sample (a) of composition ZrB <sub>2</sub> -20 vol% SiC, right sample (b) of ZrB <sub>2</sub> -20 vol% SiC-10 vol% LaB <sub>6</sub> . . . . .	19
7	Thermal conductivities of various solids. SC indicates single crystal, “poly” indicates polycrystalline. The metals shown are polycrystalline. Thermal conductivity data are based on the reference’s recommended values determined from a critical review of a compilation of literature values, with the exception of the data for diamond, which is from a single source [37]. . . . .	20
8	Total Hemispheric Emissivity (from 0.6 to 40 μm) as a function of temperature for two UHTC compositions (ZrB <sub>2</sub> -15vol%SiC and ZrB <sub>2</sub> -15vol%SiC-10vol%HfB <sub>2</sub> ) heated under 10 Pa of air in a solar collector. . . . .	25
9	Literature values of the normal spectral emittance of ZrB <sub>2</sub> , ZrO <sub>2</sub> , and borosilicate glass demonstrating the range of reported values. The higher ZrB <sub>2</sub> values correspond to an unpolished, as-sintered sample. . . . .	26
10	Schematic of experimental setup for thermogravimetric experiments. . . . .	44

11	Compilation of thermogravimetry traces for various isothermal exposures to flowing dry air at the indicated temperatures. Circle: 15.34 mol% SiC; square: 29.74 mol% SiC; upward triangle: 58.92 mol% SiC; downward triangle: 27.91 mol% SiC – 3.32 mol% TaB <sub>2</sub> . In this figure, symbols are used only to identify traces; each TG trace is made up of ~1000 data pairs. . . . .	45
12	Weight change of various compositions exposed to flowing air at various temperatures after 100 min of oxidation. Extrapolated values were used for oxidations which were completed before 100 min. Experimental data are not corrected for buoyancy effects, which are separately displayed in the figure (dashed line). . . .	46
13	Oxide coating thicknesses based on measured weight losses. . .	47
14	Cross sections (via diamond wafering blade) of specimens heat-treated at 1800°C for ~90 min. a) 15.34 mol% SiC. b) 27.91 mol% SiC. The ruled lines are 1 mm apart. The specimen in a) was mounted in the crucible in the furnace such that the bottom of the part is out of the page, and the top extends into the page. The reaction layer in b) is not uniform as portions of it snapped off as the displayed axial cross-section was being cut.	48
15	~15 mol% SiC specimen oxidized at 1600°C for ~90 min. Marker "a" indicates the amorphous silica-containing layer, "b" the fragmented zirconia, "c" the porosity from the missing SiC, and "d" the untransformed bulk. . . . .	49
16	~15 mol% SiC specimen oxidized at 1800°C for ~90 min. Marker "a" indicates the amorphous silica-containing layer with embedded zirconia, "b" the fragmented zirconia infused with silica-containing glass, "c" the transition zone with zirconia devoid of glass, "d" the SiC-depleted zone, and "e" the untransformed bulk. . . . .	50
17	~30 mol% SiC specimen oxidized at 1700°C for ~90 min. Marked regions: a) Glassy region adjacent to the surface. b) Zirconia particles immersed in silicate glass. c) ZrB <sub>2</sub> regions depleted of SiC. d) Un-transformed ZrB <sub>2</sub> -SiC. . . . .	51
18	~30 mol% SiC specimen oxidized at 1900°C for ~90 min. Marked regions: a) Glassy region adjacent to the surface. b) ZrB <sub>2</sub> regions depleted of SiC. c) Un-transformed ZrB <sub>2</sub> -SiC. . . . .	52

19	Comparatively low-magnification of $\sim 60$ mol% SiC specimen oxidized at $1900^\circ\text{C}$ for $\sim 90$ min. a) Glassy layer with imbedded bubbles. b) $\text{ZrB}_2$ with regions which had SiC replaced by porosity. Cracks/fissures in this layer are interpreted to have resulted from stresses via differences in coefficient of thermal expansions during cooling. c) Un-transformed $\text{ZrB}_2$ -SiC. . . . .	53
20	$\sim 28$ mol% SiC - $\sim 3$ mol% $\text{TaB}_2$ specimen oxidized at $1900^\circ\text{C}$ for $\sim 90$ min. Letter markers correspond to the same region types as in Figure 17. Marked regions: a) Glassy region adjacent to the surface. b) Zirconia particles immersed in silicate glass. c) $\text{ZrB}_2$ regions depleted of SiC. d) Un-transformed $\text{ZrB}_2$ -SiC. . .	54
21	Thicknesses of various layers, as measured in the SEM, of oxidation-altered $\text{ZrB}_2$ -based ceramics. . . . .	55
22	Equilibrium constant versus temperature as calculated by the expression $\Delta G_{\text{rxn}}^\circ = -RT \ln k_p$ where $\Delta G_{\text{rxn}}^\circ$ is the standard (1 bar) Gibbs energy of reaction, $R$ is the gas constant, $T$ is absolute temperature, and $k_p$ is the equilibrium constant. $k_p = 1/p_{\text{O}_2}^{5/2}$ , $k_p = p_{\text{B}_2\text{O}_2}/p_{\text{O}_2}^2$ , $k_p = p_{\text{CO}}/p_{\text{O}_2}^{3/2}$ , $k_p = p_{\text{CO}}p_{\text{SiO}}/p_{\text{O}_2}$ , for the highest to lowest traces, respectively. Standard Gibbs energies of reactions were based on the Gibbs energies of formation of compounds [?]. . . . .	56
23	Equilibrium constant versus temperature for the indicated equilibria. For this reaction, $k_p = p_{\text{CO}}p_{\text{SiO}}$ . . . . .	57
24	$\text{SiO}_{(g)}$ partial pressure as a function of oxygen partial pressure and temperature for the equilibria: $\text{SiO}_{2(l)} = \text{SiO}_{(g)} + (1/2)\text{O}_{2(g)}$ . . . . .	58
25	Thermal diffusivity measured by the laser flash technique over the temperature range of room temperature to $\sim 2000^\circ\text{C}$ . . . . .	62
26	Temperature dependencies of specific heat and theoretical density for three compositions of $\text{ZrB}_2$ -SiC- $\text{B}_4\text{C}$ . Symbols for specific heat correspond to temperatures of JANAF heat capacity data. Symbols for theoretical density have no meaning other than curve identification. . . . .	63
27	Thermal conductivities calculated from thermal diffusivity, specific heat, and theoretical density data. . . . .	64

28	<p>Left: literature values of thermal conductivity for <math>B_4C</math> and SiC. a. Single crystal SiC (R66) plotted in Watari et al. [50], based on Slack [51]. b. Mixture of <math>\alpha</math> and <math>\beta</math> SiC hot pressed with BeO sintering aid, 100% dense [50]. c. (pre-) Hexoloy SA (Saint Gobain, Niagara Falls, NY) <math>\alpha</math>-SiC, 98% relative density [48]. d. 95 vol% <math>\alpha</math>-SiC - 5 vol% <math>\beta</math>-SiC, hot-pressed [52]. e. 76 vol% <math>\beta</math>-SiC - 24 vol% <math>\alpha</math>-SiC, hot-pressed [52]. f. <math>B_4C</math> corrected for porosity [53]. g. <math>B_4C</math> data of Gilchrist and Preston [54] as plotted by Bouchacourt [53]. h. Spark-plasma sintered <math>B_4C</math> (not isotopically enriched), 98% relative density [55]. i. EP (Eagle-Pitcher) hot-pressed <math>B_4C</math> [56]. j. Hot-pressed <math>B_4C</math>, 98% relative density [56]. Right: literature values of thermal conductivity for <math>ZrB_2</math> and <math>ZrB_2</math>-SiC. k. Hot-pressed <math>ZrB_2</math> - 20 vol% SiC [57]. l. Hot-pressed <math>ZrB_2</math> [57]. m. Hot-pressed <math>ZrB_2</math> [58]. n. Hot-pressed <math>ZrB_2</math>-30 vol% SiC [58]. . . . .</p>	66
29	<p>Fracture-surface microstructures of the three evaluated compositions. Phases are identified by compositional contrast as <math>ZrB_2</math>, SiC, and <math>B_4C</math>, light to dark, respectively. . . . .</p>	70
30	<p>a. Electron micrograph of a ZBS10 fracture surface. b. <math>80 \times 20</math> grid with colors assigned to each cell based on the majority phase in that cell. c. Cells with rainbow coloring to indicate relative temperature; violet indicates highest temperature and red indicates lowest temperature. For ZBS10 at <math>1500^\circ C</math>: <math>k_{SiC} = 21.0</math> W/m·K, <math>k_{B_4C} = 9.06</math> W/m·K, <math>k_{ZrB_2} = 73.78</math> W/m·K, based on averages of literature values. . . . .</p>	71
31	<p>Depiction of <math>80 \times 20</math> cells/nodes indicating regions for node equations: a. Interior. b. Upper edge (insulated). c. Lower edge (insulated). d. Left edge (fixed temperature of <math>5^\circ C</math> above designated temperature). e. Right edge (fixed temperature of <math>5^\circ C</math> below designated temperature). f. Upper left corner. g. Lower left corner. h. Upper right corner. i. Lower right corner. . . . .</p>	72
32	<p>Thermal conductivity of three compositions calculated using averaged literature values of <math>ZrB_2</math>, SiC, and <math>B_4C</math>, the distribution of phases based on a grid overlay of SEM micrographs, and the finite difference method. . . . .</p>	73
33	<p>Thermal conductivity of <math>ZrB_2</math> calculated based on thermal conductivities of <math>ZrB_2</math>-SiC-<math>B_4C</math> multi-phase microstructures and averaged literature thermal conductivities for SiC and <math>B_4C</math>. . . . .</p>	74
34	<p>Schematic of experimental setup for thermal emittance experiments. . . . .</p>	84

35	Experimental data taken from two ZBS10-composition ribbons at a pyrometer-reported temperature of 1200°C. Symbols are meaningless save to identify the curves; the resolution of the Batch 1 scan is 20 nm, the Batch 2 scans 10 nm. For both batches, a newly oxidized specimen was used, so the discrepancies in these results are indicative of change elsewhere in the experimental setup. . . . .	85
36	Experimental data curves from oxidized ZBS10-composition ribbons are shown beneath the calculated blackbody emittance curves as given by the Planck equation for the indicated temperatures, 1220 and 1200°C, which correspond to the Wien’s displacement law-derived temperatures for the Batch 2 and Batch 1 ribbons, respectively. Symbols are meaningless save to identify the curves; the resolution of the Batch 1 data is 20 nm, and that of the Batch 2 data is 10 nm. . . . .	86
37	Emittance values calculated by dividing the experimental data values of spectral radiance from the oxidized ZBS10-composition ribbon held at a pyrometer-reported temperature of 1100°C by the spectral radiance values of a blackbody at 1120°C obtained from the Planck equation. Shaded regions indicate wavelength ranges where atmospheric interference due to the absorption characteristics of CO <sub>2</sub> and H <sub>2</sub> O perturbed the data (positive displacement due to differences in experimental conditions with those of the calibration scan). Symbols are meaningless save to identify the curves; the resolution of the data is 10 nm. . . . .	87
38	Emittance values calculated by dividing the experimental data values of spectral radiance from the oxidized ZBS10-composition ribbons held at pyrometer-reported temperatures of 1200°C by the spectral radiance values of a blackbody at the temperatures indicated by applying Wien’s displacement law to the experimental spectra. Shaded regions indicate wavelength ranges where atmospheric interference due to the absorption characteristics of CO <sub>2</sub> and H <sub>2</sub> O perturbed the data (positive displacement due to differences in experimental conditions with those of the calibration scan). Symbols are meaningless save to identify the curves; the resolution of the Batch 1 data is 20 nm, and that of the Batch 2 data is 10 nm. . . . .	88

39	Emittance values calculated by dividing the experimental data values of spectral radiance from the oxidized ZBS10-composition ribbons held at pyrometer-reported temperatures of 1300°C by the spectral radiance values of a blackbody at the temperatures indicated by applying Wien's displacement law to the experimental spectra. Shaded regions indicate wavelength ranges where atmospheric interference due to the absorption characteristics of CO <sub>2</sub> and H <sub>2</sub> O perturbed the data (positive displacement due to differences in experimental conditions with those of the calibration scan). Symbols are meaningless save to identify the curves; the resolution of the Batch 1 data is 20 nm, and that of the Batch 2 data is 10 nm.. . . . .	89
40	Differences in the observed emittance values obtained during the subsequent observations of the second batch of oxidized ribbons held at the apparent temperatures of 1120, 1220, and 1330°C. Data points obtained by subtracting the emittance values of the first observation from those of the second; the difference corresponds to the change in apparent spectral emittance after ~30 min at the indicated temperature. Shaded regions indicate wavelength ranges where atmospheric interference due to the absorption characteristics of CO <sub>2</sub> and H <sub>2</sub> O perturbed the data (positive displacement due to differences in experimental conditions with those of the calibration scan). Symbols are meaningless save to identify the curves; the resolution of the data is 10 nm. . . . .	90
41	Optical micrographs of polished cross-sections of the ribbon specimens held for 60 min at the indicated temperatures. The untransformed bulk is visible as the bright region at the base of the images. The Si-depleted zone sits above the untransformed bulk. White hatch marks on the left hand side of the images denote the regions of observed borosilicate glass. The region above these hatch marks consists of the resin used to support the specimens during polishing. . . . .	91

- 42 Individual data points shown indicate the spectral emittance values observed during the first instance of data collection from an oxidized ZBS10-composition ribbon at 1120°C plus a linear rise of magnitude 0.02 over the range of 1-6  $\mu\text{m}$  in accordance with the decline in emittance observed by comparison with the second instance of data collection. Upper and lower error bars indicate the change to these data should the assumed temperature be lowered or raised by 5°C, respectively. Shaded regions indicate wavelength ranges where atmospheric interference due to the absorption characteristics of CO<sub>2</sub> and H<sub>2</sub>O perturbed the data (positive displacement due to differences in experimental conditions with those of the calibration scan). . . . . 92
- 43 Individual data points shown indicate the spectral emittance values observed during the first instance of data collection from an oxidized ZBS10-composition ribbon at 1220°C plus a linear rise of magnitude 0.015 over the range of 1-6  $\mu\text{m}$  in accordance with the decline in emittance observed by comparison with the second instance of data collection. Upper and lower error bars indicate the change to these data should the assumed temperature be lowered or raised by 5°C, respectively. Shaded regions indicate wavelength ranges where atmospheric interference due to the absorption characteristics of CO<sub>2</sub> and H<sub>2</sub>O perturbed the data (positive displacement due to differences in experimental conditions with those of the calibration scan). . . . . 93
- 44 Individual data points shown indicate the spectral emittance values observed during the first instance of data collection from an oxidized ZBS10-composition ribbon at 1330°C plus a linear rise of magnitude 0.01 over the range of 1-6  $\mu\text{m}$  in accordance with the decline in emittance observed by comparison with the second instance of data collection. Upper and lower error bars indicate the change to these data should the assumed temperature be lowered or raised by 5°C, respectively. Shaded regions indicate wavelength ranges where atmospheric interference due to the absorption characteristics of CO<sub>2</sub> and H<sub>2</sub>O perturbed the data (positive displacement due to differences in experimental conditions with those of the calibration scan). . . . . 94
- 45 Photograph of the observed "front" surfaces of the post-heat-treated ribbon specimens from Batch 2. From left to right, the pyrometer-reported temperatures whereat each specimen was held for 60 min in flowing Ar are 1100, 1200, 1300, 1400, and 1500°C. Note the lack of specular reflection from the central portions of the ribbons held at the two highest temperatures. The marks on the ruler at the base of the image are 1 mm apart. 95

46	Optical micrographs of polished cross-sections of the ribbon specimens held for 60 min at the indicated pyrometer-reported temperatures. The untransformed bulk is visible as the bright region at the base of the images. The Si-depleted zone sits above the untransformed bulk. For these temperatures, there is no observed borosilicate glass. The region above the Si-depleted zone consists of the resin used to support the specimens during polishing. . . . .	95
47	Portion of the XRD spectra taken from the hot zones of the second batch of heat-treated, oxidized ZBS10-composition ribbons, identified here by their pyrometer-reported dwell temperatures in degrees Centigrade, as well as a scan of an oxidized ZBS10-composition ribbon having not undergone heat treatment in the RTU. Note the presence of a slight amorphous hump for all specimens except the two held at the highest temperatures for the 60 min dwell. . . . .	96

## SUMMARY

Zirconium diboride ( $\text{ZrB}_2$ ) is a ceramic material possessing ultra-high melting temperatures. As such, this compound could be useful in the construction of thermal protection systems for aerospace applications. This work addresses a primary shortcoming of this material, namely its propensity to destructively oxidize at high temperatures, as well as secondary issues concerning its heat transport properties.

To characterize and improve oxidation properties, thermogravimetric studies were performed using a specially constructed experimental setup.  $\text{ZrB}_2$ -SiC two-phase ceramic composites were isothermally oxidized for  $\sim 90$  min in flowing air in the range 1500-1900°C. Specimens with 30 mol% SiC formed distinctive reaction product layers which were highly protective; 28 mol% SiC - 6 mol%  $\text{TaB}_2$  performed similarly. At higher temperatures, specimens containing lower amounts of SiC were shown to be non-protective, whereas specimens containing greater amounts of SiC produced unstable oxide layers due to gas evolution. Oxide coating thicknesses calculated from weight loss data were consistent with those measured from SEM micrographs.

In order to characterize one aspect of the materials' heat transport properties, the thermal diffusivities of  $\text{ZrB}_2$ -SiC composites were measured using the laser flash technique. These were converted to thermal conductivities using temperature dependent specific heat and density data; thermal conductivity decreased with increasing temperature over the range 25-2000°C. The composition with the highest SiC content showed the highest thermal conductivity at room temperature, but the lowest at temperatures in excess of  $\sim 400^\circ\text{C}$ ,

because of the greater temperature sensitivity of the thermal conductivity of the SiC phase, as compared to more electrically-conductive ZrB<sub>2</sub>. Subsequent finite difference calculations were good predictors of multi-phase thermal conductivities for the compositions examined. The thermal conductivities of pure ZrB<sub>2</sub> as a function of temperature were back-calculated from the experimental results for the multi-phase materials, and literature thermal conductivities of the other two phases. This established a relatively constant thermal conductivity of 88-104 W/m·K over the evaluated temperature range.

Further heat transport characterization was performed using pre-oxidized, directly resistively heated ZrB<sub>2</sub>-30 mol% SiC ribbon specimens under the observation of a spectral radiometer. The ribbons were heated and held at specific temperatures over the range 1100-1330°C in flowing Ar, and normal spectral emittance values were recorded over the 1-6  $\mu\text{m}$  range with a resolution of 10 nm. The normal spectral emittance was shown to decrease with loss of the borosilicate layer over the course of the data collection time periods. This change was measured and compensated for to produce traces showing the emittance of the oxidized composition rising from  $\sim 0.7$  to  $\sim 0.9$  over the range of wavelengths measured (1-6  $\mu\text{m}$ ).

# CHAPTER I

## INTRODUCTION

The existence of modern air- and spacecraft has been made possible by significant advances in the field of materials science and engineering over the course of many years. Current interest is directed towards hypersonic aircraft and reusable, agile spacecraft. These applications require materials able to regularly and reliably withstand extreme temperatures and environments: The leading edges of hypersonic aircraft experience temperatures of  $\sim 1400^{\circ}\text{C}$  at Mach 6, and this temperature rises exponentially with speed. Spacecraft reentering the atmosphere could expect to face temperatures of  $\sim 2000^{\circ}\text{C}$ . Present-day thermal protection systems are not capable of surviving such environments, and therefore concessions have had to be made in the design of modern craft [1]. Next-generation thermal protection systems could enable a sharp-nosed reentry vehicle to safely maneuver to nearly any landing strip from nearly any point in orbit [2].

Towards the end of developing materials for these next-generation systems, significant research time and effort over the past several years has been devoted to select transition metal diborides belonging to a group of materials known as Ultra High Temperature Ceramics (UHTCs), specifically zirconium diboride ( $\text{ZrB}_2$ ) and the closely-related compound hafnium diboride ( $\text{HfB}_2$ ). These materials are candidates for application in the aerospace field due to their unique set of properties: ultra-high melting temperature, high hardness and strength, and high thermal and electrical conductivities (the high thermal conductivities of the materials minimize both the detrimental temperature gradients which

can result in thermal shock and the temperature rise at the leading edges) [3]. Despite these impressive characteristics, pure  $ZrB_2$  and  $HfB_2$  have an Achilles heel in that their pure forms are not sufficiently resistant to oxidation at elevated temperature ( $>1000^\circ\text{C}$ ) to be useful for applications involving significant aerothermal heating. Much of the research towards the materials has addressed this shortcoming by providing secondary phases which preferentially oxidize and form a protective ceramic oxide scale upon the bulk ceramic.

Previous research conducted by Peng and Speyer has characterized the significant protective effect of both silicon carbide (SiC) and transition metal boride additions to  $ZrB_2$ -based compositions at temperatures from 1200 to  $1500^\circ\text{C}$  in air via the formation of a protective borosilicate surface layer [4]. This research helped to identify promising compositions, but due to technical limitations inherent in the materials used to construct the experimental setup, material behavior in the "ultra-high" temperature regime ( $>1600^\circ\text{C}$  [2]) was left unexplored. Other researchers have attempted to thermogravimetrically study similar materials at temperatures up to  $1927^\circ\text{C}$ , but these experiments were not conducted *in situ*, but rather by means of weighing ceramic coupons before and after heating [24]. Such cyclical measurements can be thwarted by factors such as specimen adhesion to setting structures. A portion of the work herein presented is derived from *in situ* measurements in the ultra-high temperature domain performed using a specially outfitted furnace.

Oxidation resistance is only one facet of the overall fitness of a material for its application in extreme environments. Ceramic parts being used in extreme aerospace applications must also dissipate the tremendous amounts of heat (likely in excess  $100\text{ W/cm}^2$ ) created by the compression of the atmosphere [2]. Survival of a material under such conditions requires that a steady state surface temperature be attained within a temperature range where the mechanical

and chemical stability of the bulk can be assured. The ability of the ceramic composite to shed heat is thus directly related to the aeronautic capabilities of the design incorporating the material. The components of air- and spacecraft dissipate heat by means of both conduction through the bulk, convection to the surrounding atmosphere, and radiation from the surface to the surroundings. The rate of heat dissipation by means of the latter method rises with the fourth power of the absolute temperature, while the rates of former are functions of the first power of the same parameter. Therefore, at high temperatures, thermal radiation is the dominant heat transfer mechanism [6].

The efficiency of heat transfer by thermal radiation is described in part by the emissivity, which is a material property which implies the existence of highly polished real surfaces; for materials which deviate from this scenario due to the presence of surface features or other confounding factors, the measure is referred to as the "emittance" of the material. The spectral emittance is a ratio of the energy emitted at a particular wavelength from a unit area of the surface into a particular solid angle to the same measure from a theoretical perfectly emitting body. For the determination of the spectral emittance behavior of multi-layered materials systems, a theoretical approach is useful only in select cases, as such modeling relies on relatively simple constructions or assumptions. The oxidized surface of a bulk ceramic such as those being considered in this research is not easily treatable from such a standpoint, so direct experimental observation becomes necessary [6].

Experimental measurement of emittance is non-trivial in that the sample must be observed in relative isolation; reflections of thermal radiation from nearby, hot regions of the experimental setup (such as heating elements or furnace walls) are indistinguishable from radiation emitted from the specimen. For ceramic compositions consisting mostly of zirconium diboride, however,

research conducted by Halloran, et al. took advantage of the fact that  $\text{ZrB}_2$  behaves as a metallic conductor itself, and thinly machined ribbons of ceramic compositions tailored for oxidation resistance studies were able to be directly resistively heated with no substrate [7]. The temperature of their ribbons is controllable via observation with a high speed pyrometer. A modification of this setup has been created to allow for the measurement of the materials' spectral emittance at temperature and was employed for the work performed for the series of experiments reported herein.

## CHAPTER II

### LITERATURE REVIEW

The ultra-high temperature regime is generally accepted to begin at  $1600^{\circ}\text{C}$ , and in the context of realistic aerospace applications exceeds  $3000^{\circ}\text{C}$ . Structures at the high end of this spectrum consist of rocket engine components which are designed to ablate over the course of normal operation; the lifetime of these materials is measured in the tens of seconds rather than the tens of thousands. The leading edges of hypersonic aircraft (defined as speeds in excess of Mach 4 or 5) experience temperatures around  $1400^{\circ}\text{C}$  at Mach 6. This temperature rises exponentially with speed. The maximum temperature encountered by NASA's space shuttles is around  $1650^{\circ}\text{C}$  at the nose cone and leading edges of the wings. The space shuttles, being reusable and thus in need of long material lifetimes, were designed to reenter the atmosphere as blunt bodies such that a broad barrier layer forms between the shockwave front and the surface of the vehicle's thermal protection system (See Figure 1). This barrier layer prevents a substantial portion of the generated heat from reaching the spacecraft, but its presence also means that the returning shuttle has very limited maneuverability during its descent and experiences a contemporaneous communications blackout. For both hypersonic craft and reentry vehicles, greater controllability at high speeds is accomplished by means of lower-radius leading and trailing edges which permit laminar airflow over control surfaces. These sharp features are subject to greater aerothermal heating due to the lack of the barrier layer; the leading edges of a maneuverable reentry vehicle would be expected to experience temperatures in excess of  $2000^{\circ}\text{C}$ , but unlike

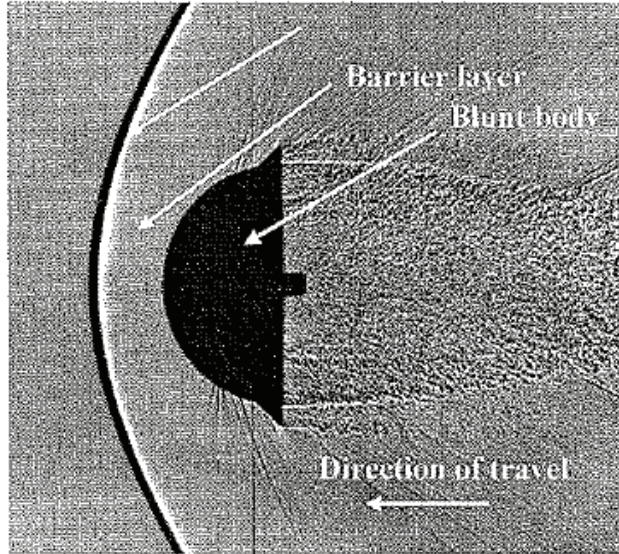


**Figure 1:** Diagram showing the substantial barrier layer formed by a blunt body such as NASA's Space Shuttle moving at supersonic speed during atmospheric reentry.

the cooler shuttles such a craft could land nearly anywhere on earth from an arbitrary reentry point [1, 2].

## ***2.1 Densification***

High relative densities are desirable in  $ZrB_2$  in order to realize its high strength and thermal conductivity, as well as to minimize any detrimental effect of surface porosity on oxidation resistance. Due to their strong covalent bonding nature and low self-diffusion, diborides have historically been densified using high temperature and pressure hot pressing techniques [3]. Gash et al. used this method in 2004 to produce theoretically dense  $HfB_2$ -20 vol% SiC at  $2200^\circ\text{C}$  for 1 hour at 25 MPa [35]. In the same year, Loehman et al. found evidence of a liquid phase sintering mechanism for UHTC densification in the form of thin silicate grain boundary phases in a hot-pressed  $ZrB_2$ -2%SiC ceramic which they attributed to oxide impurities believed present in their SiC [1]. While hot-pressing is capable of reliably forming parts with simple

geometries, the components which are desired for aerospace applications often need to have more complex geometries which would be unobtainable using hot-pressing. The machining of hot-pressed bodies is expensive, time-consuming, and wasteful. For these reasons, pressureless sintering has recently been used as a more economical means of formation capable of producing near-net shape parts. Pressureless sintering, however, requires that the driving force for densification be a result of surface interactions among contacting particles.

In studies of boron carbide ( $B_4C$ ), the formation of an oxide layer on the surface of particles interfered with this particle-to-particle contact necessary for densification [9]. Zhang et al. observed that a  $ZrB_2$  powder compact formed from commercial powder milled in air, despite having a smaller particle size (and thus, in general, a greater propensity to sinter), pressurelessly sintered to less of an extent than the same powder in its as-received state. The same milling done under an atmosphere of argon, preventing the formation of boria ( $B_2O_3$ ) and zirconia ( $ZrO_2$ ) layers upon the particles, produced a powder capable of sintering to a greater extent than the larger as-received stock. The  $B_2O_3$  was calculated to have a boiling point at 150 mTorr of approximately  $1340^\circ C$  and was found to be removable under this pressure and temperature. The  $ZrO_2$  was found to be removable via a reaction with a boron carbide ( $B_4C$ ) additive which resulted in the production of  $ZrB_2$ ,  $CO_{(g)}$ , and  $B_2O_{3(l)}$ , enabling the formation of a high density post-sintered ceramic [10]. Additions of boron-containing compounds for use as sintering aids should be done carefully within  $ZrB_2$  ceramics, as excess boron in the system can potentially result in the formation of a eutectic reaction between the line compound  $ZrB_2$  and the high-temperature phase  $ZrB_{12}$ , as evidenced in the phase diagram given in Figure 2 [1]. In other work, Zhang and his group found that the use of a WC additive and a more patient sintering schedule (540 min. at  $2150^\circ C$ ) also

resulted in a high density ( $\sim 98\%$ ). XRD analysis indicated that the tungsten and carbon had incorporated into the  $\text{ZrB}_2$  lattice, thus decreasing activation energy for densification due to the formation of atomic vacancies and electron deficiencies [11]. The effect of the formation of a liquid phase upon sintering was explored by Sciti et al. who pressureless sintered a composition of  $\text{ZrB}_2$ -20 vol%  $\text{MoSi}_2$  to achieve 99.7% of its theoretical density. Microstructural analysis suggested the formation of a Mo-rich and/or silicate glass liquid phase may have contributed to the solid-state sintering of the  $\text{ZrB}_2$  by stripping the  $\text{B}_2\text{O}_3$  from the particle surfaces [12]. Guo et al. recently explored the use of  $\text{ZrSi}_2$  as a pressureless sintering aid in  $\text{ZrB}_2$  and observed the same liquid phase effects [13]. The silicate liquid phase was found to eventually contribute to coarsening at higher temperatures by Zhang et al. but the addition of small amounts of carbon was found to result in the formation of SiC, thus allowing for solid-state sintering of  $\text{ZrB}_2$  at temperatures as low as  $1950^\circ\text{C}$  to high density [14]. Work by Peng and Speyer has resulted in the production of  $\text{ZrB}_2$  with additions of SiC,  $\text{TaB}_2$  and  $\text{TaSi}_2$  pressureless sintered (with the use of  $\text{B}_4\text{C}$  as a sintering aid) at  $2000^\circ\text{C}$  in argon for 1 hour to closed porosity and then post-hot isostatically pressed at  $1800^\circ\text{C}$  for 30 min at 207 MPa (Ar) to theoretical density [4].

## ***2.2 Oxidation***

### **2.2.1 Protective Oxide Layer**

Pure  $\text{ZrB}_2$  has not been observed to resist oxidation in high temperature regimes.  $\text{ZrB}_2$  exposed to air at elevated temperatures reacts with oxygen to form  $\text{ZrO}_2$  and  $\text{B}_2\text{O}_3$ . The  $\text{B}_2\text{O}_3$  scale is non-protective since  $\text{B}_2\text{O}_3$  has a high vapor pressure above  $\sim 1200^\circ\text{C}$  (its boiling point, i.e. 1 atm vapor

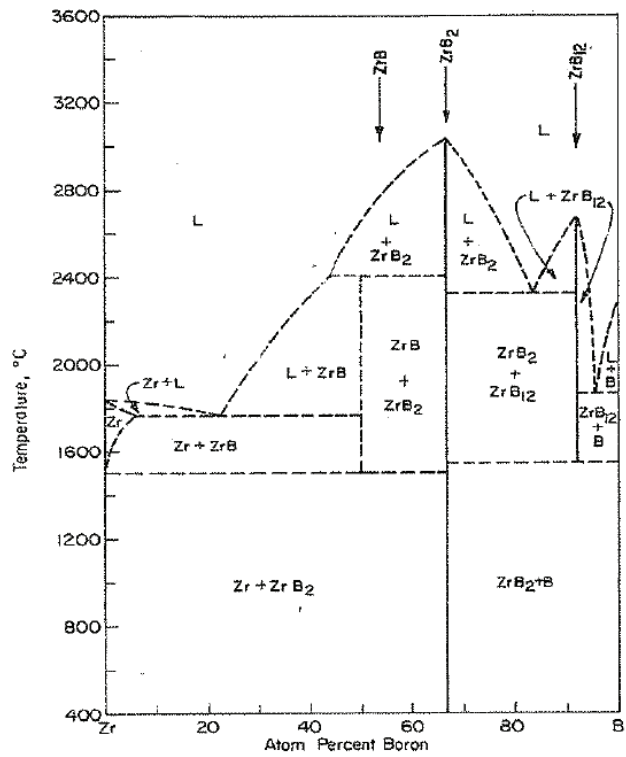


**Figure 2:** Phase diagram of the Zr-B system including non-equilibrium high-temperature phases.

pressure, is 1860°C) [5]. For ZrB<sub>2</sub> at temperatures above ~1000°C, yet below 1800°C, B<sub>2</sub>O<sub>3</sub> exists as a liquid amongst surface pores created by the formation of columnar grains of ZrO<sub>2</sub> (see Figure 3) [4]. The B<sub>2</sub>O<sub>3</sub> readily evaporates, thus exposing the fragmented zirconia and unoxidized bulk below [15]. As temperatures increase, the remaining zirconia undergoes a phase change at 1650°C from monoclinic to tetragonal capable of destroying large-scale components made from the material [16]. For ZrB<sub>2</sub>-20 vol% SiC, below 1200°C, oxidation reaction rates are similar to pure ZrB<sub>2</sub>, but above 1200°C the SiC addition improves oxidation resistance. The addition of SiC to the system confers oxidation resistance upon ZrB<sub>2</sub> via formation of an amorphous borosilicate scale which can be seen in Figure 4 as well as a disruption of the zirconia scale due to the evolution of carbon oxide gases such that the phase change is not catastrophic [17, 1, 25]. Work by Rezaie et al. uses compositional, structural, and thermogravimetric analysis to paint a timeline for the evolution of the protective oxide mechanisms of the ZrB<sub>2</sub>-SiC system undergoing heating in air, finding that between 800 and 1200°C the oxidation of ZrB<sub>2</sub> to ZrO<sub>2</sub> and B<sub>2</sub>O<sub>3</sub> was the dominant chemical process, resulting in passive oxidation behavior due to the continuous formation of the liquid boria layer (and a corresponding constant rate of weight gain  $\sim 3.3 \times 10^{-3}$  mg/cm<sup>2</sup>·°C). Around 1200°C, SiC begins to oxidize to form SiO<sub>2</sub>. In the same temperature regime, the evaporation of B<sub>2</sub>O<sub>3</sub> becomes rapid, resulting in a weight loss of  $\sim 1.0 \times 10^{-3}$  mg/cm<sup>2</sup>·°C. Above 1300°C, the depletion of the B<sub>2</sub>O<sub>3</sub> results once again in an overall weight gain due to the continued formation of SiO<sub>2</sub>, which was measured after having been heated to 1500°C to be a maximum of  $\sim 10$  μm in thickness. Beneath, a layered structure was found to have formed. Directly below the more pure silicate glass layer was a  $< 3$  μm thick layer of zirconium embedded within SiO<sub>2</sub>, and then a  $\sim 10$  μm thick layer of SiC-depleted ZrB<sub>2</sub>

and  $\text{ZrO}_2$  above the untransformed bulk. This layered structure reveals that, in order for the  $\text{SiO}_2$  layer to form, oxygen must first diffuse through the oxide layer to the bulk material beneath and oxidize  $\text{SiC}$  once to  $\text{SiO}_{(g)}$ , which must then be transported across the depleted region to the upper layers and oxidize once more to  $\text{SiO}_2$  [18]. This process can be observed by the changing composition of the glass phase. Below  $1300^\circ\text{C}$ ,  $\text{B}_2\text{O}_3$  is found to be the major component of the glass phase. Above,  $\text{SiO}_2$  is the major component, and after 24 hr at  $1400^\circ\text{C}$  partially reacted  $\text{SiC}$  has been found to remain in the scale. Reaction rate observed to be parabolic, but oxygen consumption data were not found to match a parabolic rate equation due to selective evaporation of  $\text{B}_2\text{O}_3$ , which led to a reduction in barrier layer thickness or changes in diffusion rates of the various products and reactants as the glass composition changed [17].

The nature of the diffusing species of oxygen through the silicate layer is a point of some interest, as varying routes of transport may be impacted differently by additives to the ceramic composite. At and below  $1000^\circ\text{C}$ , the rate of oxygen diffusion through vitreous silica is proportional to first power of its partial pressure, which is expected of the kinetics wherein the permeation of molecular oxygen is the dominant mechanism [19]. Using isotope labeling, Costello and Tressler confirmed the molecular diffusion at these temperatures, but observed significant incorporation of their tracer oxygen atoms ( $^{18}\text{O}$ ) into the silicate network at  $1300^\circ\text{C}$ , which suggests a significant contribution by a lattice diffusion mechanism. At odds with this interpretation is the fact that a single activation energy of 27 kcal/mol is reported for the parabolic oxidation of silicon to temperatures in excess of  $1400^\circ\text{C}$  [20]. Subsequent work has found that the presence of water in the environment can lead to exchange between the diffusing molecular oxygen and the oxygen atoms of the silica. Doremus reviewed several studies of oxygen diffusion through silica glass and

revealed a correlation between the degree of network diffusion claimed and the permissiveness of the experimenters in allowing water to be present. He shows that this exchange mechanism is capable of masquerading as network diffusion in isotope tracing studies, which had been identified as dubious due to the fact that the network diffusion kinetics at play are too slow to fully explain the oxidation rates observed [21].

Parabolic weight change may be used to track the formation of a protective oxide layer when it is present, though similar oxide scale kinetics are observed for non-protective scales of zirconia and boria [22]. Parabolic kinetics indicate that one of the reactants, in this case oxygen, must diffuse through an ever-thickening layer to react with the bulk material at the base of the scale. This results in the oxide growth rate  $dx/dt$  being inversely proportional to the scale thickness,  $x$ , and proportional to the scaling constant  $k_p$

$$\frac{dx}{dt} = \frac{k_p}{x} \quad (1)$$

Upon integration, this becomes

$$x^2 = 2k_p t \quad (2)$$

leading to the observed parabolic growth evident in Figure 3 [23]. Parabolic kinetics may be seen in the curves of the isothermal mass change plots in the lower temperatures displayed in Figure 5. Opila and Halbig fired samples of ZrB<sub>2</sub>-20 vol% SiC in stagnant air in a zirconia furnace at temperatures of 1327, 1627, and 1927°C for one, five, and ten cycles, observing the parabolic kinetic model holding valid at all temperatures [24]. *In situ* thermogravimetric studies of ZrB<sub>2</sub>-20 vol% MoSi<sub>2</sub> observed the material to exhibit (after a 300 min dwell) parabolic oxidation curves above 1200°C. Parabolic behavior was observed immediately at 1400°C. The weight gain after oxidation at 1200°C

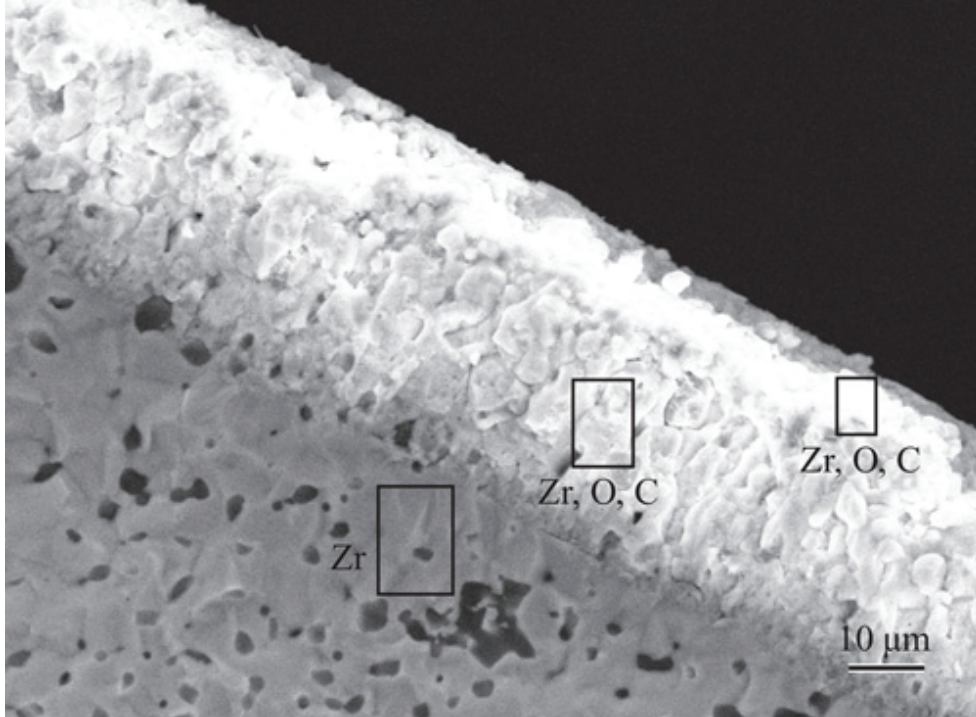


**Figure 3:** SEM micrograph of cross section of  $\text{ZrB}_2$ -10 vol%  $\text{B}_4\text{C}$  heat treated in flowing air to  $1460^\circ\text{C}$ . Rectangles enclose regions where EDS performed; elements detected are listed next to each rectangle.  $30\ \mu\text{m}$  thick zirconium oxide scale is non-protective

was found to be significantly less than that at  $1000^\circ\text{C}$ , again indicating that the formation of the amorphous silicate layer is beneficial [12].

### 2.2.2 Environmental Effects

The availability of oxygen is important for a material which forms passivating oxide scales as a means of protection in extreme environments. In an atmosphere such as the earth's at sea level with a  $pO_2 \sim 0.2\ \text{atm}$ , an increase in SiC content (30 vol% instead of 20 vol%) has been shown to improve the protection of  $\text{ZrB}_2$  by more readily forming the protective  $\text{SiO}_2$  layer, but at a  $pO_2$  of  $2 \times 10^{-4}\ \text{atm}$ , the extra SiC only oxidizes partially to the gaseous product  $\text{SiO}_{(g)}$ , which leaves the system and does not form a protective  $\text{SiO}_2$ -based layer [26]. At lower partial pressure of oxygen still,  $\text{ZrB}_2$ -30 vol% SiC in a  $pO_2 \sim 10^{-16}$

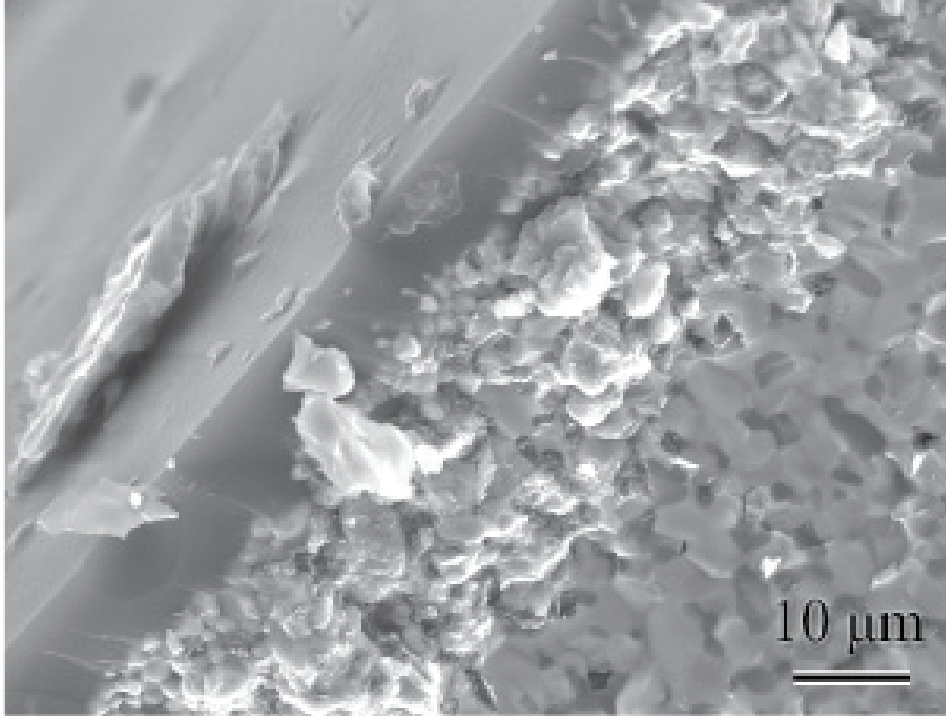


**Figure 4:** SEM micrograph of cross section of  $\text{ZrB}_2$ -28 vol% SiC having undergone oxidation. Note the layered structure: silicate glass over SiC-depleted zone over unreacted bulk.

atm environment (created by a  $\text{CO}/\text{CO}_2$  mixture) at  $1500^\circ\text{C}$  was found to also exhibit linear-with-time weight gain kinetics not suggestive of any significant protection from oxidation. At this  $pO_2$ , Rezaie et al. show that the  $\text{ZrB}_2$  oxidizes to  $\text{ZrO}_{2(s)}$  and a volatile  $\text{B}_2\text{O}_{3(l)}$ , and SiC to  $\text{CO}_{(g)}$  and  $\text{SiO}_{(g)}$  leaving a non-protective, porous  $\text{ZrO}_2$  scale [27]. It is accepted within the community of researchers studying UHTCs that most small-scale experiments do not approximate a true reentry or hypersonic environment, wherein the materials would be subjected to low-pressure and partially or fully dissociated gases, but such experimental environments are valued for their role in screening materials under often-ideal conditions for the formation of protective oxide layers [2].

Fahrenholtz has presented a thermodynamic analysis of  $\text{ZrB}_2$ -SiC oxidation in which he observes that  $pO_2$  beneath the scale should be considerably less than that in the atmosphere above due to the chemical potential gradient

necessary for diffusion. This value, though prescribed by the oxidation reaction kinetics occurring in the region, is not precisely known; it can, however, be thermodynamically bound: a  $pO_2$  too low would fall below the sooting limit, and  $CO_{(g)}$  present due to the SiC addition would spontaneously reduce to carbon. Graphite has not been reported in the SiC-depletion layer, so the value of  $pO_2$  present there is assumed to be higher. Fahrenholtz calculates the value of  $pO_2$  in the SiC-depleted layer to be between  $4.1 \times 10^{-14}$  and  $1.8 \times 10^{-11}$  Pa, forming a gradient which contributes to the migration of  $SiO_{(g)}$  from the bulk to the surface scale [28]. Opeka et al. observed that the protection provided by the  $SiO_2$  layer in limiting oxygen diffusion also provides for a back-pressure of the  $SiO_{(g)}$  to build to the point of rupturing the glass layer, resulting in a cyclic protective/non-protective scale forming pattern which overall results in a semi-protective layer. A corresponding change in the kinetics has not been observed, but the understanding of both the oxidation kinetics and oxygen transport behavior of the system remains incomplete [29].

Components made from  $ZrB_2$  and/or  $HfB_2$ -based compounds performing in the earth's atmosphere would be required to contend with the presence of water vapor. Nguyen et al. created samples of  $HfB_2$ -20 vol% SiC and  $ZrB_2$ -20 vol% SiC which they thermogravimetrically analyzed in an environment of 90% water vapor and 10% oxygen at a pressure of 1 atm. The  $HfB_2$  composition proved to be substantially more oxidation resistant in this environment over the temperatures studied (1200, 1300, and 1400°C) [30].

### **2.2.3 Transition Metal Boride Additions**

While SiC additions have proven useful for the prevention of oxidation in the temperature range of 1200 to 1500°C, at higher temperatures the silicate glass loses effectiveness. To address this issue, researchers evaluated additions

that are able to help stabilize the silicate glass layer at higher temperatures or provide a new mechanism of protection as the silicate glass layer fails. Talmy et al. began with a composition of  $\text{ZrB}_2$ -25 vol% SiC and formed several test compositions by substituting some of the  $\text{ZrB}_2$  with other Group IV-VI transition metal borides ( $\text{NbB}_2$ ,  $\text{CrB}_2$ ,  $\text{TaB}_2$ ,  $\text{TiB}_2$ , and  $\text{VB}_2$ ). Independently, each of these compounds has an oxidation resistance lower than that of  $\text{ZrB}_2$ , but when present in small amounts in the silicate glass layer, theory suggests the glassy layer will undergo liquid-liquid phase separation. Each addition was found to result in increased oxidation resistance compared to the base composition due to an increase in the liquidus temperature and viscosity, thus a decrease in the oxygen diffusivity. The effect becomes more pronounced with increasing cation field strength (defined as  $Z/r^2$ , where  $Z$  is the valence of the cation and  $r$  is the ionic radius), though by 1500°C the phase separation and oxidation resistance effects were not seen in any system due to the fact that the temperature exceeded the dome of immiscibility [31, 29]. Opila et al. created coupons of  $\text{HfB}_2$  and  $\text{ZrB}_2$  containing varying amounts of the additives SiC and  $\text{TaSi}_2$  and cyclically oxidized them in 10 min increments in stagnant air at 1627°C for a total of 100 min. They found a composition of  $\text{ZrB}_2$ -20 vol% SiC-20 vol%  $\text{TaSi}_2$  oxidized to less of an extent than either  $\text{ZrB}_2$ -20 vol% SiC,  $\text{HfB}_2$ -20 vol% SiC, or  $\text{ZrB}_2$ -33 vol% SiC, the latter having been formulated to test whether the extra silicon in the  $\text{TaSi}_2$  composition had been responsible for the improvements in oxidation resistance. Further studies using arc jet heating, however, found that liquid phases formed at 1927°C, related either to the melting of  $\text{Ta}_2\text{O}_5$  or that of a largely uncharacterized zirconium tantalate phase (termed “phase V”). These liquid phases resulted in rapid degradation of the material [32]. Later work by Talmy et al. demonstrated that even small amounts of mutual addition of  $\text{Ta}_5\text{Si}_3$  and  $\text{ZrB}_2$  resulted in

an overall densification for all intermediate compounds of the system. They observed Ta<sub>2</sub>O<sub>5</sub>-induced glass phase separation using EDS analysis of periodic glassy and crystalline regions present on a test composition surface oxidized at 1400°C [33].<sup>1</sup>

Recent work by Peng and Speyer has shown that TaB<sub>2</sub> additions above ~3 mol% or TaSi<sub>2</sub> additions above ~6.7 mol% to the ZrB<sub>2</sub>-B<sub>4</sub>C-SiC system are detrimental to oxygen resistance at 1500°C (though beneficial at 1200 and 1400°C). They hypothesize that this effect is due to the disruption to the glassy oxide layer caused by the formation of TaC in the depleted layer beneath. Mass change curves generated from this research can be seen in Figure 5. Additionally, above 1400°C no tantalum was observed via EDS in the glassy layer; consequently no evidence of liquid-liquid phase separation was observed [4].

#### 2.2.4 High Temperature Study

Above 1500°C, previous attempts at gathering thermogravimetric data have been thwarted by failure to remedy or account for a reaction between the sapphire hook (used to suspend the sample) and the oxidation products [17]. Other researches have utilized other experimental methods to collect information at these high temperature domains; Gash et al. performed arc jet testing on HfB<sub>2</sub>-20 vol% SiC at two different heat fluxes for two 10 min durations each. In lower heat flux condition, passive oxidation of SiC helped maintain a

---

<sup>1</sup>As a side-note, these same “island and lagoon” structures on the surface of the cooled ZrB<sub>2</sub>-SiC have recently been described by Karlsdottir et al. as being the result of a liquid solution of B<sub>2</sub>O<sub>3</sub>, SiO<sub>2</sub>, and ZrO<sub>2</sub> transported by means of convection cells in the oxide layer at high temperature [7]. No mention is made of the possibility that the structures arose during cooling from 1500°C, though it should be noted that the orientation of the faces of the specimens concerned with respect to the Earth’s gravitational field may play a role. Karlsdottir’s specimens were oxidized in open air, and a surface parallel to the horizontal was observed.

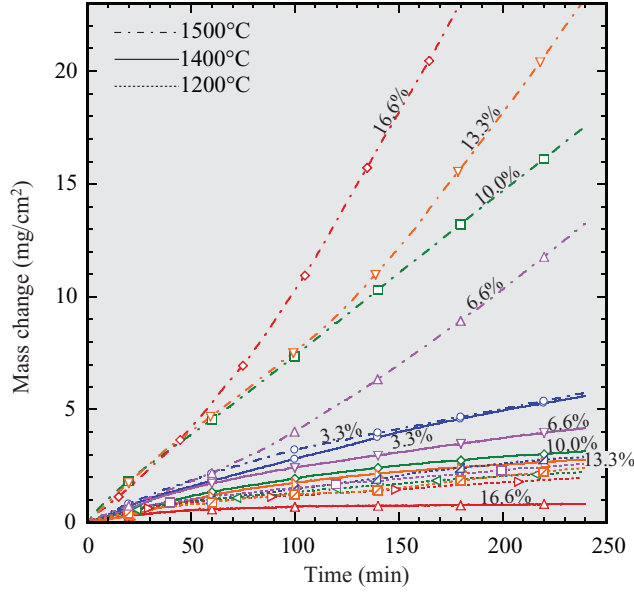


**Figure 5:** Isothermal mass change with varying vol% additions of TaB<sub>2</sub>. Note that the parabolic behavior at 1200 and 1400°C is not observed at 1500°C.

steady state surface temperature of 1700°C. Higher heat flux resulted in temperature spike to 2400°C, due to a change from passive to active oxidation of SiC and the resulting presence of a thick, porous HfO<sub>2</sub> layer. [35]. Zhang et al. explored the oxidation behavior of a coupon of composition ZrB<sub>2</sub>-20 vol% SiC-10 vol% LaB<sub>6</sub> versus that of ZrB<sub>2</sub>-20 vol% SiC under an oxyacetylene torch for 600 seconds. The former compound reached a surface temperature of 2400°C, yet was found to have a compact, adherent, protective oxidized surface ~545 μm thick, whereas the surface of the latter compound was non-adherent and marked by significant spallation and cracking as seen in Figure 6. No silicon was observed through EDS on the surface of the lanthanum-containing compound, rather, the surface was found to consist almost entirely of ZrO<sub>2</sub> and La<sub>2</sub>Zr<sub>2</sub>O<sub>7</sub> [36].

### 2.3 Heat Transfer

Understanding of a material's oxidation behavior is important, but it is only one facet of material behavior. Should these materials be used for atmospheric

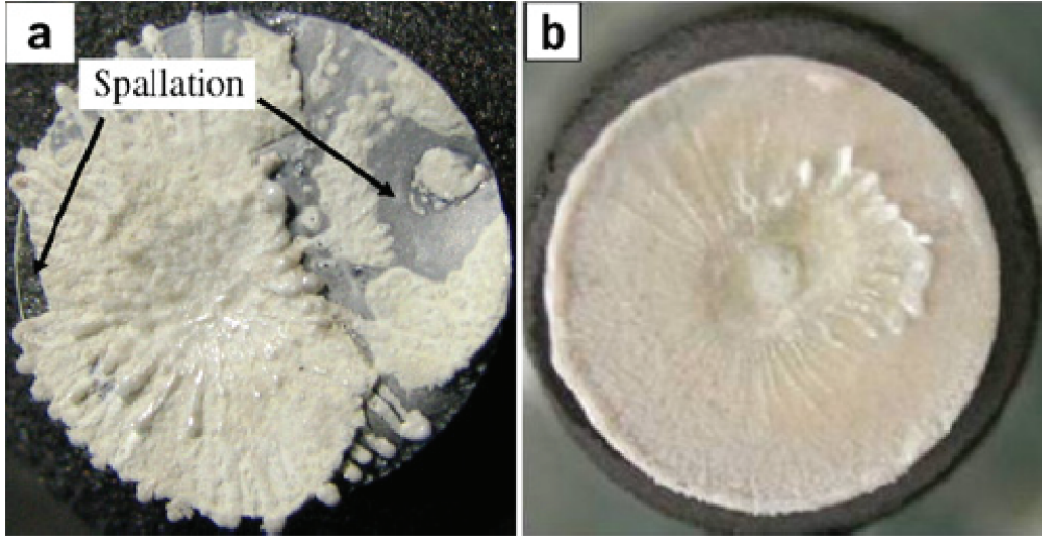


**Figure 6:** Photograph of samples after oxyacetylene torch testing. Left sample (a) of composition  $\text{ZrB}_2$ -20 vol% SiC, right sample (b) of  $\text{ZrB}_2$ -20 vol% SiC-10 vol%  $\text{LaB}_6$ .

reentry or supersonic leading edge applications, they will experience an influx of aerothermal heat, likely in excess  $100 \text{ W/cm}^2$  [2]. Assuming the thermal protection systems achieve a steady state condition, the material will be shedding heat from the surface through the processes of conduction through the bulk and radiation into the environment. These means by which the material is able to cool itself are described in part by its thermal conductivity and emissivity.

### 2.3.1 Thermal Conductivity

Thermal conduction in dielectric solids occurs by anharmonic waves, referred to as phonons, superimposed upon lattice vibrations. Conductive solids have the additional heat transfer mechanism of electron motion. Figure 7 [37] shows example thermal conductivity data for a variety of electrical conductors and dielectrics. For the typical dielectric, with rising temperature above zero Kelvin, thermal conductivity increases as  $T^3$ , reaching a maximum well below room temperature [38]. This maximum is limited by scattering of phonons with

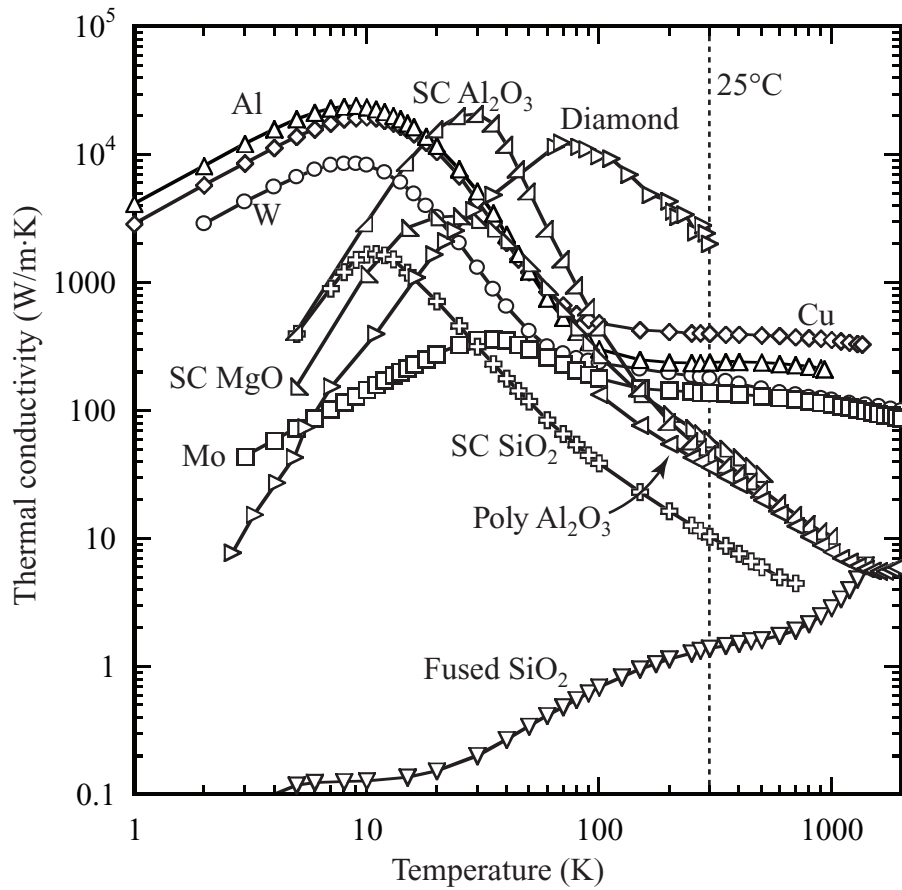


**Figure 7:** Thermal conductivities of various solids. SC indicates single crystal, “poly” indicates polycrystalline. The metals shown are polycrystalline. Thermal conductivity data are based on the reference’s recommended values determined from a critical review of a compilation of literature values, with the exception of the data for diamond, which is from a single source [37].

microstructural features which disrupt the periodicity of the lattice, e.g. dislocations and the strain fields around them, grain boundaries, and porosity. The temperature of the maximum is related to the Debye temperature, which is proportional to the maximum in the distribution of standing wave vibration frequencies. Since the Debye temperature increases with melting point and elastic modulus, diamond thermal conductivity reaches its maximum at a comparatively higher temperature. As a result, diamond has the highest known thermal conductivity at room temperature.

At low temperatures, the concentration of generated phonons is low, hence there is a long mean-free path between interactions. This mean-free path decreases with increasing temperature; the thermal conductivity maximum represents the point at which the phonon mean free path is of the same order of magnitude as scattering from microstructural imperfections. As temperature is increased above the maximum, the thermal conductivity decrease is proportional to  $1/T$  as the phonon-phonon scattering mean-free-path continues to decrease. The change in thermal conductivity with temperature tends to decrease to slopes below those predicted by  $1/T$ , as the phonon-phonon mean free path reaches atomic scale dimensions [38]. Other factors (negatively) affecting the thermal conductivity of dielectrics are the extent of solid solution and complexity of structure [39]. At the extreme, fused silica, having no lattice periodicity, has a very low thermal conductivity. Its rise with increasing temperature is from radiation contributions to heat transfer.

The electrically-conductive solids exhibit a similar maximum in thermal conductivity at cryogenic temperatures; however, at  $\sim 100$  Kelvin, thermal conductivity is relatively constant with increasing temperature, making electrically-conductive solids significantly more thermally conductive than the dielectrics (with the exception of diamond) at temperatures above room temperature.

Thermal conductivity  $k$  is typically measured under steady state conditions based on an integrated form of Fourier’s Law. For example, given a hollow cylinder of specimen, the equation for determining  $k$  is expressed as

$$k = \frac{q \ln\left(\frac{r_o}{r_i}\right)}{2\pi L(T_i - T_o)} \quad (3)$$

where  $q$  is the heat flow,  $r_i$  and  $r_o$  are the inner and outer radii of the cylinder, respectively,  $L$  is the length of the cylinder, and  $T_i$  and  $T_o$  are the inner and outer cylinder temperatures, respectively. In the experimental setup, the cylinder is placed in a furnace in the middle of three coils of heating wire, one above, one surrounding, and one below. The coils in the axial direction function as guard heaters to ensure that no axial heat gradient is seen by the specimen. A heating wire is fed through the center of the cylinder and generates heat that flows radially outward. This heat flow is monitored based upon knowing the current and voltage drop across a gauge-length of wire. Thermocouples monitor inner and outer temperature; steady state is established when inner and outer temperatures do not change with time. This method, and others similar for differing sample geometries (e.g. flat plates), can be time consuming and require large specimen sizes [40].

Thermal diffusivity  $\alpha$  is related to thermal conductivity by

$$\alpha = \frac{k}{\rho c_p} \quad (4)$$

where  $\rho$  is the specimen density and  $c_p$  is the specimen specific heat. Thermal diffusivity is appropriate for describing non-steady state heat flow; it increases with increasing thermal conductivity and decreasing thermal storage requirements of the specimen. Specific heat data may be obtained via differential scanning calorimetry, and density may be measured using pycnometry and a

sample crushed to a powder, thereby allowing thermal diffusivity data to be converted to thermal conductivity data [40].

### 2.3.2 Emittance

The energy per unit time emanating hemispherically from a unit area of surface at a given wavelength and temperature from a perfectly absorbing and emitting sample (blackbody) is given by Planck's Law:

$$R_T(\lambda) = \frac{2\pi hc^2}{\lambda^5} \frac{d\lambda}{\exp\left(\frac{hc}{\lambda kT}\right) - 1} \quad (5)$$

where  $R_T(\lambda)$  is the spectral radiosity,  $h$  is Planck's constant,  $k$  is Boltzmann's constant,  $\lambda$  is wavelength,  $c$  is the speed of light, and  $T$  is the absolute temperature. Real bodies absorb less than this ideality due to reflection (common to metals) or transmission (common to dielectrics). The ratio of the spectral radiosity of a real body (RB) to that of a blackbody (BB) is the spectral emissivity:

$$\varepsilon_T(\lambda) = \frac{R_T(\lambda)_{RB}}{R_T(\lambda)_{BB}} \quad (6)$$

The maximum value of spectral emissivity is one, which is when the real body emission equals that of a blackbody at that wavelength. The borosilicate coating of a ZrB<sub>2</sub> ceramic composite is observed to sit atop a partially oxidized, porous "SiC-depleted zone", and as such the morphology of the system prohibits the notion of a true "emissivity" measurement, but the word is found in literature addressing such measurements in this materials system. Scatteia et al. studied the radiative properties of two compositions: ZrB<sub>2</sub>-15vol%SiC and ZrB<sub>2</sub>-15vol%SiC-10vol%HfB<sub>2</sub>, and reported that total emissivity generally increased with temperature due to the formation of the protective oxide layer, and that the specimen containing no HfB<sub>2</sub> showed a comparatively higher

emissivity overall (see Figure 8). The data presented, however, were only of total emissivity, which encompasses the behavior of the material over the broad swath of wavelengths considered ( $0.6 \mu\text{m}$  to  $40 \mu\text{m}$ ) [41]. A more complete view of this important material property requires the consideration of the spectral emittance instead of total emittance. Spectral emissivity data are available in the literature for, zirconium diboride, zirconia, and borosilicate glass on their own, but the behavior of a specific material is sensitive to both the chemistry and morphology of the surface; this effect is illustrated in Figure 9, which gives, in part, two trends for the spectral emittance of  $\text{ZrB}_2$ : one sample polished and etched, the other as sintered. The emittance behavior of  $\text{ZrB}_2$  and  $\text{HfB}_2$  compounds with oxide layers is difficult to predict, as the base material behaves as an electrical conductor and the coating as a dielectric. These two classes of materials behave very differently in respect to spectral emissivity with wavelength and emissivity with temperature. Also, the interface between the base material and oxide coating is typically rough, which can increase emittance, as the crevices on the surface may behave as blackbody cavities [6].

Thermal emittance is an important consideration for UHTCs since, while many important applications involve heating via interaction at high speed with the atmosphere, the components may cool themselves by radiating to ambient surroundings. The higher the emittance, the more efficiently the absorbed heat may be disposed of, and the lower the steady state surface temperature of the component may be.

**Hemispherical Emissivity vs. Temperature for Two UHTC Compositions**

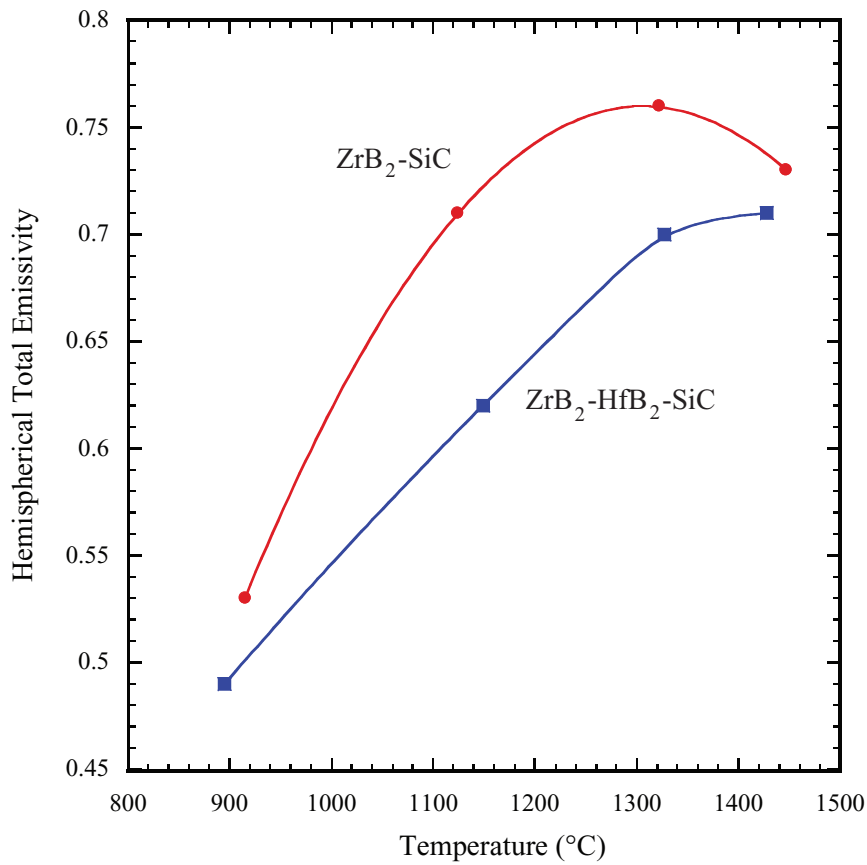


**Figure 8:** Total Hemispheric Emissivity (from 0.6 to 40  $\mu\text{m}$ ) as a function of temperature for two UHTC compositions ( $\text{ZrB}_2\text{-15vol\%SiC}$  and  $\text{ZrB}_2\text{-15vol\%SiC-10vol\%HfB}_2$ ) heated under 10 Pa of air in a solar collector.

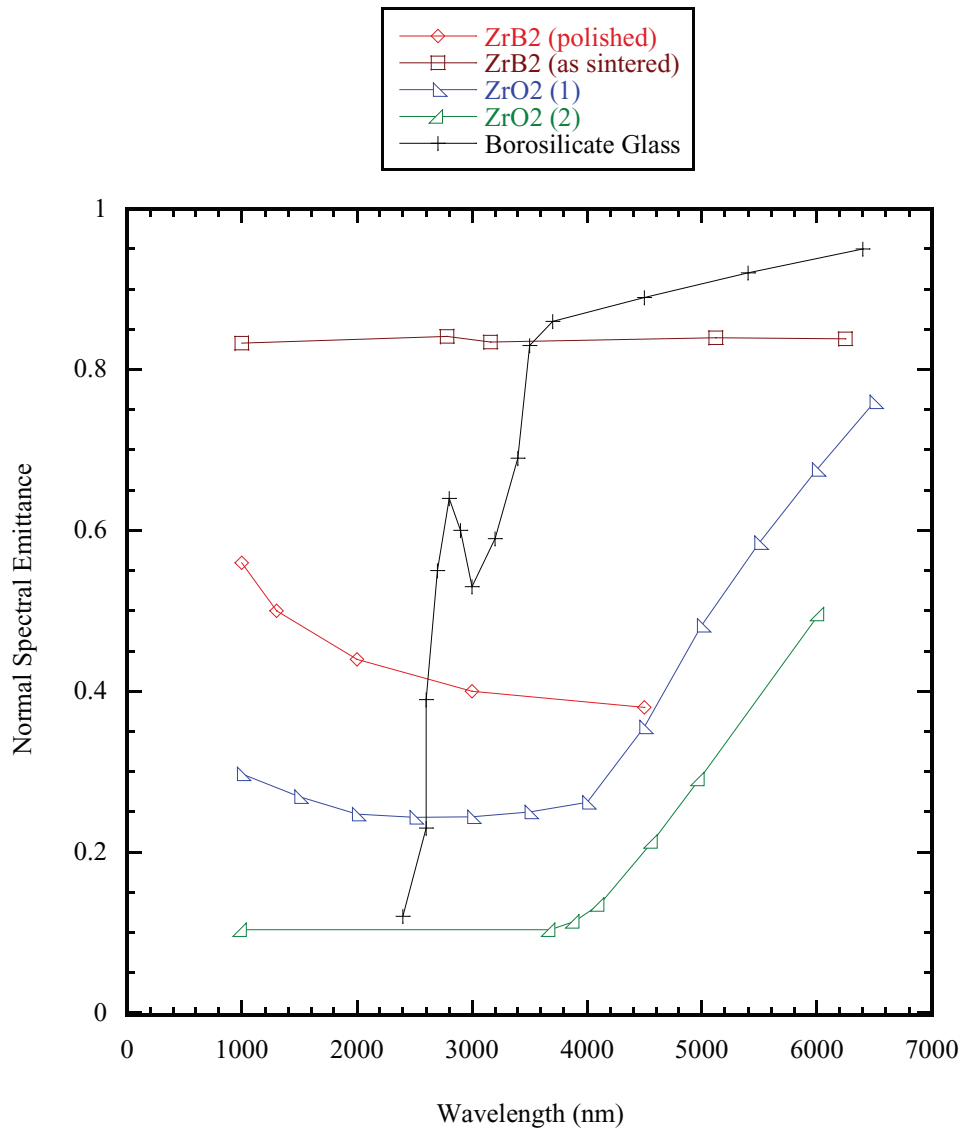


**Figure 9:** Literature values of the normal spectral emittance of  $ZrB_2$ ,  $ZrO_2$ , and borosilicate glass demonstrating the range of reported values. The higher  $ZrB_2$  values correspond to an unpolished, as-sintered sample.

## CHAPTER III

# THERMOGRAVIMETRIC STUDY OF ZRB<sub>2</sub>-BASED CERAMIC COMPOSITES

### 3.1 *Experimental Procedure*

Commercially-available powders were used for raw materials. The major crystalline phase(s), grade, and suppliers are listed for each powder in Table 1. The particle sizes of commercially-available TaB<sub>2</sub> were deemed too large for

**Table 1:** Raw Material Characteristics for Oxidation Specimens

	Phases	Particle Size	Supplier
ZrB <sub>2</sub>	ZrB <sub>2</sub>	$d_{50} = 2.20 \mu\text{m}$	Grade B, H. C. Starck, GmbH
B <sub>4</sub> C	stoichiometric B <sub>4</sub> C	$d_{50} = 0.8 \mu\text{m}$	Grade HS, H. C. Starck, GmbH
SiC	$\alpha$ -SiC	$d_{50} = 0.88 \mu\text{m}$	8S490NDP, Superior Graphite, Chicago, IL
TaB <sub>2</sub>	TaB <sub>2</sub> , Ta <sub>3</sub> B <sub>4</sub>	$< 43 \mu\text{m}$	ESPI Metals, Ashland, OR

pressureless sintering. Hence, sedimentation-based selection was used to obtain finer particles: Powders were dispersed in ethanol using an ultrasonicator (FS-14 Solid State Ultrasonicator, Fisher Laboratory Equipment Division, Pittsburgh, PA) for 10 min. The mixture was allowed to settle in ethanol for 1 h. The top 7 cm (of a total column height of 14 cm) of fluid was then extracted using a pipette. Based on laser particle size analysis (Model LS 13 320, Beckman Coulter, Fullerton, CA), decanted particles had a  $d_{50}$  of 1.1  $\mu\text{m}$ . The decanted suspensions were dried in a beaker on a hot-plate.

The compositions of synthesized powder mixtures are given in Table 2. The powder mixtures were suspended in methanol, and mixed in a ball mill for 24 h, using B<sub>4</sub>C as media. These powders were then dried in air in a free

**Table 2:** Sample Compositions for Oxidation Specimens

Composition	Mole Percent				Volume Percent			
	ZrB <sub>2</sub>	B <sub>4</sub> C	SiC	TaB <sub>2</sub>	ZrB <sub>2</sub>	B <sub>4</sub> C	SiC	TaB <sub>2</sub>
1	77.39	7.27	15.34	0	80.35	8.94	10.71	0.0
2	64.25	6.04	29.70	0	70.30	7.82	21.88	0.0
3	37.55	3.53	58.92	0	46.15	5.14	48.71	0.0
4	63.14	5.62	27.91	3.32	68.79	7.25	20.45	3.51

convection oven at 75°C. The powders were then ball milled again in water with dissolved polyvinyl alcohol (PVA, Celanese Ltd., Dallas, TX), polyethylene glycol (PEG, Alfa Aesar, Ward Hill, MA), and Darvan 821A (R.T. Vanderbilt Company Inc., Norwalk, CT), using B<sub>4</sub>C as media for 8 h. PVA functioned as a binder with PEG functioning as a plasticizer, and Darvan 821A served as a dispersing agent. The highly viscous suspension after this milling step was dried in a free convection oven at 75°C, and then sieved using a 60 mesh screen.

Approximately 400 mg of powder were uniaxially pressed into cylindrical pellets using a maximum pressure of 117 MPa, holding for 1 min. The pellets were loaded into latex encapsulants which were in turn evacuated. These were cold isostatically pressed (CIP) in a water/oil mixture at 345 MPa for 1 min. This was followed by a binder removal heat-treatment of 0.25°C/min to 500°C under a flowing argon atmosphere. Fifteen pellets were fabricated for each composition.

These pellets were fired in a graphite tube furnace (Model M11, Centorr Vacuum Industries Inc., Nashua, NH) under flowing argon, using graphite setters. The furnace was initially evacuated to  $\sim 4$  Pa (roughing pump) and backfilled with argon. The typical heating schedule was 50°C/min to 2100°C,

soaking for 1 h, and then cooling at 40°C/min to room temperature. The pellets were then hot isostatically pressed (HIP, American Isostatic Press, Columbus, OH) at 1800°C for 30 min under an argon gas pressure of 207 MPa. The densities of unfired pellets were determined from measured dimensions and mass; the densities of pressureless sintered and post-HIPed pellets were determined using Archimedes' method. All HIPed specimens were 100% dense based on theoretical densities calculated from the rule of mixtures.

All of the surfaces of the post-HIPed samples were ground away using 320 grit SiC grinding paper (Buehler, Lake Bluff, IL), and the resulting pellet dimensions were measured with calipers, from which surface areas were calculated. Pellets were ~5.3 mm in diameter and 3-4 mm in height. The oxidation behaviors were then investigated using thermogravimetric analysis. A schematic of the experimental setup is shown in Figure 10. An analytical balance (model AX205, Mettler-Toledo, Inc, Columbus OH) with a measurement precision of 0.01 mg was fully encased in a water-cooled aluminum enclosure. The enclosure had a coupling extending from its top which mated with a water-cooled coupling attached to the base of the furnace which was sealed to and supported a stabilized zirconia tube with a 4.7 cm inner diameter. This tube extended upward through the hot zone of the furnace and continued through the top of the furnace for an additional 35.5 cm into the ambient air. Loose refractory alumina fiber rested at the top of the tube to minimize air turbulence within the tube which would otherwise disturb the balance reading. A mass flow controller (Model GFC 17, Aalborg, Orangeburg, NY), attached to a cylinder of compressed dry air controlled air flow into the enclosure and then through the zirconia tube which in turn extended through the furnace. The furnace (model DT-36-VT 2000°C vertical tube furnace, Deltech, Inc, Denver, CO) was of cylindrical shape, mounted (cylindrical axis) vertically. Outer

radial positions of the furnace were heated using uniformly-spaced  $\text{MoSi}_2$  U-tube heating elements. These were partially insulated from radial positions toward the furnace center by shaped stabilized zirconia bricks. Along still more inner radial positions of the furnace, six symmetrically-placed rod-type stabilized zirconia heating elements extended vertically through the furnace. Two independent PID control systems were used, one which brought the furnace temperature up to  $\sim 1300^\circ\text{C}$  via the  $\text{MoSi}_2$  elements, at which point power was additionally applied across the semiconducting zirconia elements. The hot zone of the furnace was approximately 10 cm along the axial direction, with another 40.5 cm of length extending from the edges of the hot zone to the axial extremes of the furnace. Raising the hot-zone temperature from room temperature to  $1900^\circ\text{C}$  required  $\sim 2$  days. The furnace was brought to isothermal soak temperatures of 1500, 1600, 1700, 1800, and  $1900^\circ\text{C}$  and held at each of those temperatures while isothermal oxidation experiments were performed on all compositions. Data was collected on a personal computer through rapid polling (using Microsoft Visual Basic 4.0) through RS232 communications.

A brass tripod with set-screw feet (for orientation adjustment) was fabricated and placed on the balance stage. Inserted into this was a stabilized yttria-stabilized zirconia (McDaniel Advanced Ceramic Technologies, Beaver Falls, PA) hollow tube (6.3 mm outer diameter, 61 cm long). Placed at the top of the hollow tube were stabilized zirconia crucibles, consisting of a bottom stem which could be inserted into the stabilized zirconia tube, and a cylindrically-shaped partially hollowed cylindrical container. These were fabricated by uniaxially pressing 2 cm cylinders of stabilized zirconia powder (8 mol%  $\text{Y}_2\text{O}_3$  stabilized  $\text{ZrO}_2$ ,  $d_{50} = 0.5 \mu\text{m}$ , Inframat Advanced Materials, Manchester, CT) mixed with binder at 125 MPa. These were subsequently loaded into latex bags which were evacuated and sealed, and were then CIPed

at 345 MPa. These functioned as blanks for CNC machining (model DSLS 3000, Taig Micromill, Chandler AZ) into the aforementioned crucible shape. Binder was extracted from the green parts in static air at a heating rate of 0.5°C/min to a soak temperature 500°C, and held for 4 h. These parts were then fired in the same furnace as the oxidation experiments using soak temperatures in the range 1600-1800°C for 1 h. Specimens for oxidation experiments were placed in these crucibles (on top of zirconia chips lining the bottom of the crucible) so that the axial direction of the disks was horizontal, leaving a portion of the disk within the crucible, and a larger proportion extending above the upper lip of the crucible.

The analytical balance and its enclosure, with the specimen mounted above it, were raised using a foot-pedal-based jack system into the hot zone of the furnace. Specimens were elevated over ~5 min so as to raise the sample quickly to its soak temperature, while minimizing the propensity for thermal shock of the stabilized zirconia crucibles and supporting tube. Air flow rate upward through the tube was maintained at 0.1 l/min. Specimen weight change was based on the weight measured by the balance while the specimen was at room temperature. Weight change data during the period of elevating the balance was omitted since the balance measurement was unstable. To evaluate repeatability, 2-3 thermogravimetric oxidation heat-treatments were performed on each composition at each soak temperature. Displayed traces are those considered most representative.

Thermogravimetric analyzers show a buoyancy effect [40] in which the condensed phases of the specimen, and the structure which holds it up, applies an upward force based on the mass of gas which is displaced (Archimedes principle). As the furnace is heated, this gas expands and the displaced mass decreases, giving the impression of a weight gain on the TG trace. This mass

change can be calculated assuming an ideal gas (air), a constant temperature in the hot zone of the furnace, and a linear temperature gradient extending from the edge of the hot zone to the point of exit of the furnace, which is assumed to be at room temperature. For the specimen, crucible, and the hot-zone portion of the hollow tube the crucible is mounted on, the buoyancy mass  $m$  was calculated based on:

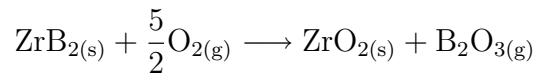
$$m = \frac{MpV_H}{RT_F}$$

where  $M$  is the molar mass of air,  $p$  is atmospheric pressure,  $V_H$  is the volume of the specimen, crucible, and support tube (1032.31 mm<sup>3</sup>),  $R$  is the gas constant, and  $T_F$  is the hot zone absolute temperature. For the hollow stabilized zirconia tube extending through the linear temperature gradient, the bouoyant mass was calculated based on:

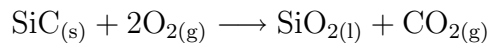
$$m = \frac{MpA}{R \left( \frac{T_F - T_R}{h} \right)} \ln \left( \frac{T_F}{T_R} \right)$$

where  $A$  is the cross-sectional area of the tube,  $T_R$  is absolute room temperature, and  $h$  is the height of the portion of the furnace associated with the linear temperature gradient going from room temperature to the hot zone temperature. The mass of displaced gas at a given hot-zone temperature minus the mass of displaced gas at room temperature was calculated.

In addition, as the samples are oxidized, due to their geometry, the surface area of untransformed bulk available for further reaction decreases. This can artificially lower the rate of the reaction, so a correction is made to account for this loss. For the reactions



and



it is assumed that boron oxide forms as an escaping gas and silica forms as a liquid/glass. These reaction stoichiometries dictate that the number of moles of  $\text{ZrO}_2$  formed are equal to the number of moles of  $\text{ZrB}_2$  consumed,  $n_{\text{ZrO}_2} = n_{\text{ZrB}_2}$ , and similarly  $n_{\text{SiO}_2} = n_{\text{SiC}}$ . Note that the latter equality holds even if the reaction produced CO as opposed to  $\text{CO}_2$ .

Let  $\Delta M$  be the measured mass change after 100 min exposure to a given oxidation temperature. Then:

$$\Delta M = (M_{\text{ZrO}_2} - M_{\text{ZrB}_2}) + (M_{\text{SiO}_2} - M_{\text{SiC}})$$

where  $M_{\text{ZrB}_2}$  and  $M_{\text{SiC}}$  are the masses of zirconium diboride and silicon carbide converted, respectively, and  $M_{\text{ZrO}_2}$  and  $M_{\text{SiO}_2}$  are the masses of zirconia and silica produced, respectively. Letting  $W$  be the molar mass:

$$\Delta M = n_{\text{ZrB}_2}(W_{\text{ZrO}_2} - W_{\text{ZrB}_2}) + n_{\text{SiC}}(W_{\text{SiO}_2} - W_{\text{SiC}})$$

We define  $X_{\text{SiC}}$  as the mole fraction of SiC in the original  $\text{ZrB}_2$ -SiC composition, thus:

$$n_{\text{SiO}_2} = \frac{\Delta M}{\left(\frac{1}{X_{\text{SiC}}} - 1\right)(W_{\text{ZrO}_2} - W_{\text{ZrB}_2}) + (W_{\text{SiO}_2} - W_{\text{SiC}})} \quad (7)$$

Let  $\rho$  be the density and  $V'$  be the volume of oxide formed:

$$V' = \frac{n_{\text{SiO}_2} W_{\text{SiO}_2}}{\rho_{\text{SiO}_2}} + \frac{n_{\text{ZrO}_2} W_{\text{ZrO}_2}}{\rho_{\text{ZrO}_2}} \quad (8)$$

Given a disk geometry for the partially oxidized specimen of diameter  $d$  and height  $h$ , with a uniform oxide coating thickness of  $T$ :

$$V' = 2\pi \left(\frac{d}{2}\right)^2 T + (h - 2T) \left( \pi \left(\frac{d}{2}\right)^2 - \pi \left(\frac{d - 2T}{2}\right)^2 \right) \quad (9)$$

The diameter  $d$  and height  $h$  of the disk vary during oxidation since the densities of the consumed phases and the corresponding formed oxide phases are not the same. Let  $\Delta V$  be the volume of products formed minus the volume

of reactants consumed; that is, the change in volume of the disk. Recognizing the equivalence of moles of  $\text{ZrB}_2/\text{ZrO}_2$  and  $\text{SiC}/\text{SiO}_2$ :

$$\Delta V = n_{\text{SiC}} \left( \frac{W_{\text{SiO}_2}}{\rho_{\text{SiO}_2}} - \frac{W_{\text{SiC}}}{\rho_{\text{SiC}}} \right) + n_{\text{ZrB}_2} \left( \frac{W_{\text{ZrO}_2}}{\rho_{\text{ZrO}_2}} - \frac{W_{\text{ZrB}_2}}{\rho_{\text{ZrB}_2}} \right) \quad (10)$$

If the dimensions of the disk before oxidation are  $d_0$  and  $h_0$ , then after partial oxidation, the change in volume is:

$$\Delta V = \pi \left( \frac{d}{2} \right)^2 h - \pi \left( \frac{d_0}{2} \right)^2 h_0$$

Assuming that the thickness of oxide scale forming on all surfaces is the same, then the change in linear dimensions from oxidation in the axial and radial directions would be the same:  $d - d_0 = h - h_0$ , thus:

$$\Delta V = \frac{\pi}{4} ((h - h_0 + d_0)^2 h - d_0^2 h_0) \quad (11)$$

Equation 8 (inserting in equation 7 and the definition of mole fraction) may be used to determine the volume of oxide formed. Inserting this into equation 9, along with calculated values of  $d$  and  $h$  from equations 10 and 11 will yield  $T$  through numerical solution.

Crystalline phases in the samples were identified using X-ray diffraction (XRD, Model X'Pert PRO Alpha-1, PANalytical, Netherlands). Scans were recorded at room temperature over a  $2\theta$  range of  $10\text{-}80^\circ$  at a scan rate of  $0.01^\circ/\text{s}$ . XRD of oxidized specimens were taken from cross sections formed via a diamond wafering blade.

Specimens were directly photographed with a digital camera after cross-sections were made via a diamond-impregnated wafering blade. Microstructures of oxidized samples were investigated using scanning electron microscopy (SEM, LEO 1530, Carl Zeiss SMT, Inc., Thornwood, NY) and energy dispersive spectrometry (EDS, Oxford Pentafet detector with ultrathin window,

Oxford Instruments, Oxfordshire, UK). For displayed micrographs, specimen cross-sections were fractured surfaces formed via impact, with the oxidized surfaces mounted on the SEM stub to be parallel with the beam axis. Specimens were coated with gold (sputtering for 2 min) to form a conductive surface. For measurement of layer thicknesses, specimens were cut perpendicular to the oxidized surfaces using a diamond-impregnated wafering blade, and then imaged in the SEM. Separate measurements of the top, sides, and bottom layer thicknesses were recorded. Side thickness measurements were generally averages of measurements from the left and right sides.

### ***3.2 Results and Discussion***

Initial experiments were performed using an alumina gas flow tube and either alumina stages or crucibles to hold the specimens. Oxidation heat-treatment in this study at and above 1700°C showed substantial reaction of specimens with their containers. For that reason, the furnace was reconstructed so that no alumina was present in the hot zone. All results which follow correspond to oxidation under that configuration.

Phases identified from XRD of oxidized specimen cross sections were  $\text{ZrB}_2$ ,  $\text{SiC}$ , and  $\text{ZrO}_2$ . For compositions in which  $\text{TaB}_2$  was a batch additive, no distinct  $\text{TaB}_2$  phase was detected, but a shift in  $2\theta$  positions of  $\text{ZrB}_2$  peaks imply the formation of a  $\text{Zr}_x\text{Ta}_{1-x}\text{B}_2$  solid solution. Trace amounts of  $\text{ZrC}$  were detected for the composition with  $\sim 60$  mol%  $\text{SiC}$  after oxidation heat-treatments at 1600 and 1700°C. Trace amounts of  $\text{ZrC}$  were also detected for the composition with  $\sim 3$  mol%  $\text{TaB}_2$  after oxidation heat-treatment at 1800°C.

Figure 11 shows TG traces of the compositions exposed to temperatures ranging from 1500 to 1900°C. At 1500 and 1600°C, all compositions are roughly grouped together with the exception of  $\sim 15$  mol%  $\text{SiC}$ , which showed a higher

initial weight gain, but roughly equal rate of weight gain with time as the other specimens. This was not the case for 1700 to 1900°C heat-treatments; the ~15 mol% SiC composition gained weight at a comparatively rapid rate, though the rate slowed over the 10-30 min time span. At 1900°C the ~30 mol% SiC and ~28 mol% SiC – ~3 mol% TaB<sub>2</sub> specimens showed a constant and remarkably small weight gain over the evaluated time span. The ~60 mol% SiC specimen showed an initial rapid rate of weight gain that decreased at longer times. The thermogravimetry trace shown for the specimen with ~60 mol% SiC was altered from the original, which displayed periodic spikes from the popping of bubbles, after which an instantaneous downward shift in mass was recorded. For the trace displayed in Figure 11, the spikes were deleted and subsequent data were adjusted upward to align with the data before the spikes.

The results of buoyancy calculations are shown in Figure 12. Also shown in this figure is a summary of the results in Figure 11 by comparing the mass change after 100 minutes of exposure at the various soak temperatures. Accounting for buoyancy effects, a weight loss for the specimen with ~30 mol% SiC occurred after heat-treatments at 1600 and 1700°C. Using the weight loss (per unit surface area) in Figure 12, the thickness of a ZrO<sub>2</sub>/SiO<sub>2</sub> oxide coating was calculated (Figure 13) based on equations developed in the appendix. Weight losses used in the calculation were based on the differences between measured values after 100 min and the weight change associated with buoyancy for a given temperature.

The oxidation resistances of all specimens except ~15 mol% SiC are remarkably good. The substantial difference between oxidation resistances of specimens with ~15 mol% SiC and ~30 mol% SiC is visually apparent when the oxidation scale was examined in cross section (Figure 14). With ~15

mol% SiC (Figure 14a) the extensive oxidation product layer is mostly zirconia (based on EDS analysis of this region of the specimen in the SEM) with a small concentration of silica, in the region nearest to unreacted ZrB<sub>2</sub>/SiC. The specimen with ~30 mol% SiC (Figure 14b) showed comparatively impressive oxidation resistance, with only a thin (~0.1 mm) reaction product layer (the makeup of which is discussed subsequently) covering an unaltered interior.

Figure 15 shows a cross-sectional fracture surface of near-surface regions of the ~15 mol% SiC specimen oxidized at 1600°C. An amorphous silica-containing layer (a) with embedded zirconia coats the specimen surface. Boron is unreliably detected with the available EDS so the extent to which the amorphous layer contained boron oxide has not been established. Slightly (~10 μm) below this layer are fragmented zirconia particles (b), making up collective shapes correlating to ZrB<sub>2</sub> grains appearing in the specimen interior. The zirconia regions were distinguished from ZrB<sub>2</sub> by presence/absence of oxygen peaks in EDS data, and the tendency for bright spots from charging effects on the non-conductive ZrO<sub>2</sub> regions. Pores (c) (of shapes similar to SiC grains seen in the specimen interior) reside in the region of transition from ZrO<sub>2</sub> to ZrB<sub>2</sub> grains. The specimen interior (d) consists of ZrB<sub>2</sub> lighter-shaded grains and darker-shaded SiC grains.

As shown in Figure 16, the ~15 mol% SiC specimen heat-treated at 1800°C showed distinct layers of oxidation products penetrating from the surface inward: a zirconia-embedded silica-containing glass surface layer (a), a region of high concentration of ZrO<sub>2</sub> particles infused with silica-containing glass (b), a region in which zirconia particles with no surrounding liquid/glass phase are elongated in the direction orthogonal with the surface (c). A transition along a distinct interface is then observed to ZrB<sub>2</sub> grains with pores taking the place of what was once SiC grains (d). The most interior region consists

of the original  $\text{ZrB}_2\text{-SiC}$  matrix (e). The  $\sim 15$  mol% SiC oxidized at  $1700^\circ\text{C}$  showed similar layers, though of diminished thicknesses. The microstructure in Figure 16 came from the top portion of the specimen.

Increasing the SiC content from 15 to 30 mol% produces a microstructure with a separate silicate glassy layer largely devoid of zirconia, and layers similar to that previously described underneath, with the exception that there was no zone of elongated  $\text{ZrO}_2$  and porosity (Figure 17). At  $1900^\circ\text{C}$  (Figure 18), the specimen with  $\sim 30$  mol% SiC developed a glassy silica-containing surface layer (a), within which the amount of embedded zirconia is difficult to determine. At greater depths, this transitions through a sharp boundary to a broad zone of  $\text{ZrB}_2$  (b), which is devoid of SiC. These particles have rounded from their appearance as grains in the original two-phase matrix, surrounded by porosity. Still deeper, at another sharp boundary, the original  $\text{ZrB}_2/\text{SiC}$  matrix can be seen (c).

The microstructure of  $\sim 60$  mol% SiC oxidized at 1700 and  $1800^\circ\text{C}$  is similar to  $\sim 30$  mol% SiC oxidized at the same temperatures, though the relative depths of the SiC-depleted  $\text{ZrB}_2$  zones are thinner, and the zone of  $\text{ZrO}_2$  surrounded by glass is more dilute in  $\text{ZrO}_2$ .

After heat-treating this composition at  $1900^\circ\text{C}$ , bubbles are observed in the glassy silica-containing layer (Figure 19).

In previous work performed by Peng and Speyer at  $1200\text{-}1500^\circ\text{C}$ , addition of  $\text{TaB}_2$  to specimens oxidized at  $1600^\circ\text{C}$  changed the appearance of the layer of  $\text{ZrO}_2$  embedded in glass to one in which the crystalline phases appear more fragmented [4]. That effect was not as visually apparent for oxidation heat-treatments at  $1700\text{-}1800^\circ\text{C}$ ; however, these specimens showed somewhat thinner layers of glass-infused zirconia and SiC-depleted  $\text{ZrB}_2$ , as compared to specimens without  $\text{TaB}_2$  additions, but similar SiC content. After oxidation

at 1900°C (Figure 20), the region of ZrB<sub>2</sub> depleted of SiC was substantially thinner than the case in which TaB<sub>2</sub> was not added (Figure 18).

There was clear visual evidence of the flow of silicate glassy phase onto the ZrO<sub>2</sub> chips on which specimens were resting, as well as down onto the bottom of the zirconia crucible. Figure 21 shows the temperature variation in thicknesses of the glassy surface layers, the oxide ZrO<sub>2</sub>/silicate liquid layers beneath them, and the SiC-depleted ZrB<sub>2</sub> regions still further into specimen interiors. For ~15 mol% SiC composition, distinct glass layers were not apparent. The layers of predominantly ZrO<sub>2</sub> were coarser than the SiC-depleted layers; both layers generally coarsened with increasing soak temperatures. The ZrO<sub>2</sub> layer became generally coarser in going from top to bottom of the specimen. For the ~30 mol% SiC specimens, the thickness of the layer at the specimen bottom was again coarser than the sides or top. Glassy surface layers were apparent, whose thickness did not vary substantially with soak temperature. The composition with ~60 mol% SiC showed a substantial increase in layer thicknesses in going from 1800 to 1900°C soaking temperatures. Layer thicknesses were generally least coarsened for the compositions with ~28 mol% SiC and ~ 3 mol% TaB<sub>2</sub>. For both ~30 mol% SiC and the composition with ~28 mol% SiC and ~3 mol% TaB<sub>2</sub>, glassy layer thicknesses appeared to decrease slightly in going from 1700 to 1800°C soak temperatures.

### ***3.3 Discussion***

Up through oxidation temperatures of 1600°C, all evaluated compositions developed a passivating glassy surface layer along with an oxide layer beneath it which were protective for the evaluated time period. Starting at 1700°C, the composition with ~15 mol% SiC lacked enough SiC to form an adequate volume of silica/borosilicate glass for passivation.

Silicate liquid phase was drawn into the crucible either by gravity, or by capillary action at the contact points. The capillary removal mechanism would imply preferential removal of liquid in close proximity, which is near the bottom of the specimen. This in turn would make this region more vulnerable to oxidation, the coarser the oxide layers observed in these regions.

The  $\sim 15$  mol% SiC specimen shows a slowing of weight gain after  $\sim 30$  min to a near-linear weight gain with time (Figure 11). If oxidation were occurring through a diffusion-resistive layer which was coarsening with time, TG traces with a more continuous parabolic shape would have been expected. It is interpreted that initial parabolic behavior changed to a linear weight gain as the formation of silica liquid through oxidation was matched by its capillary extraction.

Calculated oxide layer thicknesses from weight loss data were within the spread of the three measured (top, middle, bottom) thicknesses of the oxide portion of the microstructure (Figure 21). Compared to the total thicknesses of all the characteristic layers, the calculated thicknesses were roughly lower. The differences may be attributable to the inaccuracy of assumptions in the buoyancy calculations (e.g. linear temperature gradient), development of porosity (e.g. vapor pressure within the specimen pushing liquid toward the surface), and/or preferential oxidation of SiC in interior regions near unaltered ZrB<sub>2</sub>-SiC (which was not accounted for in the calculation).

Figure 22 is a plot of equilibrium constants as a function of temperature for differing versions of the oxidation of SiC and ZrB<sub>2</sub>, showing that all indicated reactions are highly favorable. The equilibrium constants are so large at all temperatures, that a buildup of product gas partial pressures to and exceeding ambient would not stop reactants from going toward products. It is reasonable to assume that in the gaseous environment within the SiC-depleted

ZrB<sub>2</sub> region, that the partial pressure of oxygen is substantially lower than the ambient, as it is being consumed through oxidation and its supply is limited by diffusion through layers closer to the surface. In the reduction of metal oxides, plots such as Figure 22 can be used to specify the  $p_{O_2}$  for which certain metals will oxidize while other metal oxides will reduce. In this case; however, the equilibrium constants do not represent the same ratio of partial pressures, making such evaluations difficult.

The SiC-depleted ZrB<sub>2</sub> zone is seen ubiquitously for oxidation temperatures of 1700°C and above. Figure 23 shows the stability of reaction product SiO<sub>2(l)</sub> in contact with reactant SiC<sub>(s)</sub>. If it assumed that a pressure within the SiC-depleted ZrB<sub>2</sub> layer cannot exceed atmospheric (since a bubble would otherwise form and burst), and equimolar amounts of SiO and CO gaseous products form, then as shown in the figure, SiO<sub>2(l)</sub> will react with SiC to form vapor phases above ~1525°C. Thus for temperatures above this, any SiO<sub>2</sub> which forms immediately reacts with the SiC in contact with it to form gas phases which escape from the reaction zone. In contrast, oxidation of ZrB<sub>2</sub> forms B<sub>2</sub>O<sub>2</sub> vapor and a zirconia scale; this scale impedes subsequent oxidation of the ZrB<sub>2</sub> beneath it. Hence, available oxygen preferentially attacks constantly-exposed SiC, rather than neighboring ZrB<sub>2</sub> grains (protected by even a thin layer of ZrO<sub>2</sub>). This analysis is consistent with the observation that SiC-depleted ZrB<sub>2</sub> regions are not visually apparent until oxidation temperatures of 1700°C were used. The same result would be expected if the immediate oxidation product of SiC was SiO<sub>(g)</sub> rather than SiO<sub>2(l)</sub>. Figure 24 shows that SiO<sub>(g)</sub> production is favored by high temperatures and low oxygen partial pressures. The extent to which SiO<sub>2(l)</sub> spontaneously decomposes to SiO<sub>(g)</sub> depends on the rate of escape of SiO<sub>(g)</sub> through the layers closer to the specimen exterior.

The formation of bubbles in the specimen with ~60 mol% SiC oxidized at

1900°C, implying the formation of vapor pressures exceeding ambient, may be attributed to a number of contributing factors. Gaseous products of oxidation, e.g.  $\text{CO}_{(g)}$  and  $\text{B}_2\text{O}_{2(g)}$  are not thought to be a major contributor since these gases form only in equimolar quantities to the amount of oxygen consumed, and the oxygen partial pressure in these buried layers is interpreted to be quite low. Only if the diffusion of these gaseous products through layers closer to the surface is significantly hindered as compared to the diffusion of oxygen, would significant partial pressures of these reaction products form. A more significant contributor would be the volatilization of  $\text{B}_2\text{O}_{3(l)}$  whose equilibrium vapor pressure is  $\sim 0.3$  atm at 1900°C. The high concentration of SiC would imbue relatively close proximity of SiC and  $\text{SiO}_{2(l)}$  (since there is a vast SiC source near the surface, its consumption to form the passivating glass/liquid layer does not require much penetration into the specimen interior), and the lower viscosity of the fluid at this temperature would facilitate liquid migration to contact interior SiC, facilitating reaction. These condensed phase to gaseous phase reactions would form copious amounts of  $\text{SiO}_{(g)}$  and  $\text{CO}_{(g)}$ .

### ***3.4 Conclusions***

The minimum SiC content for passivization in pore-free  $\text{ZrB}_2$ -SiC mixtures is between 15 and 30 mol% SiC. The passivating near-surface microstructure for isothermal heat-treatments at and above 1700°C consists of consecutive layers of a silicate liquid/glass,  $\text{ZrO}_2$  infused with liquid/glass,  $\text{ZrB}_2$  devoid of SiC, and then an unaltered  $\text{ZrB}_2$ -SiC microstructure. When more rapid oxidation is observed, a layer of zirconia and porosity is observed, which can be quite extensive. Use of  $\sim 6$  mol%  $\text{TaB}_2$  along with the  $\sim 28$  mol% SiC resulted in what appeared to be thinner oxide passivating layers and equally good oxidation resistance. Bubbles observed in the glassy layer and their periodic

bursting implied from thermogravimetry in the 60 mol% SiC specimen heat-treated at 1900°C indicate the buildup of product gases and/or condensed phase vapors which exceeded ambient pressure. The selective removal of SiC from near-surface ZrB<sub>2</sub>-SiC microstructure was proposed to be the result of reaction products of SiC oxidation being unprotective to yet-unreacted SiC, as compared to reaction products of ZrB<sub>2</sub>.

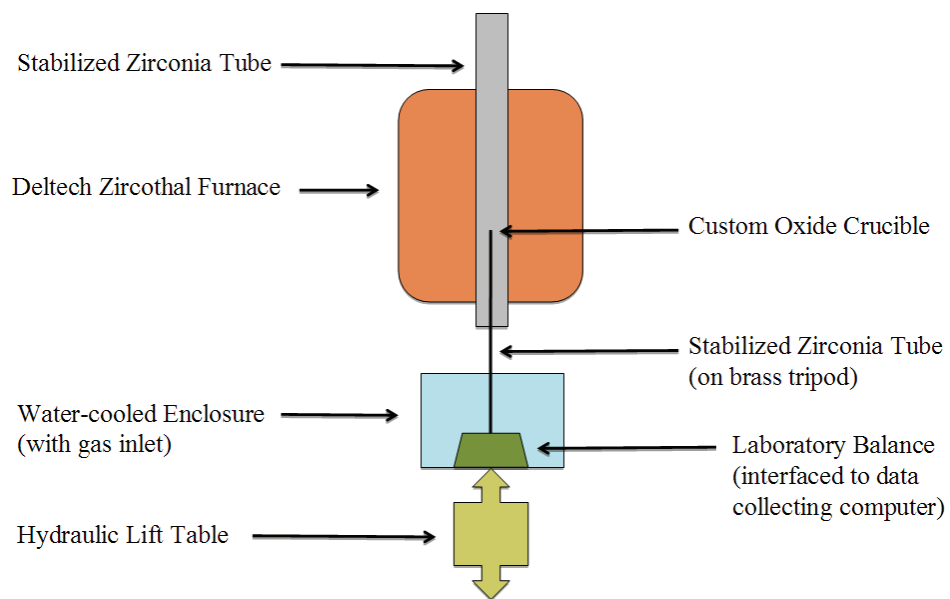


**Figure 10:** Schematic of experimental setup for thermogravimetric experiments.

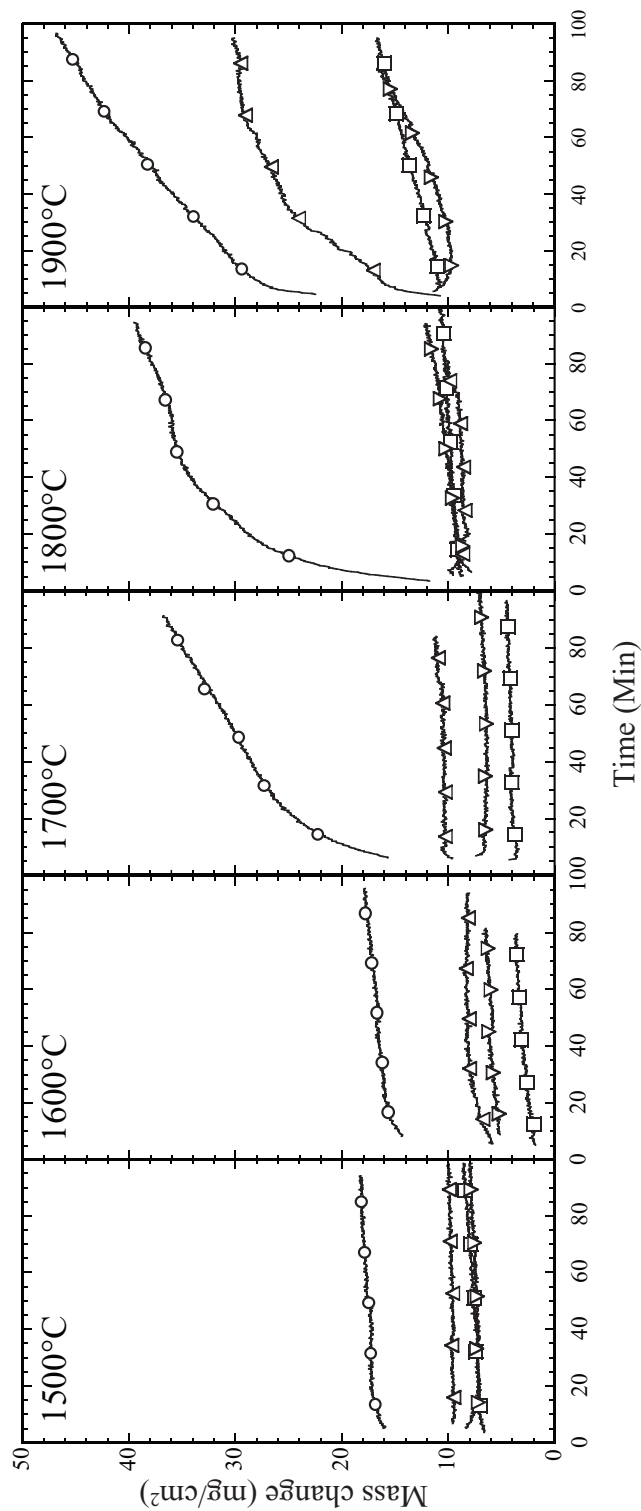


**Figure 11:** Compilation of thermogravimetry traces for various isothermal exposures to flowing dry air at the indicated temperatures. Circle: 15.34 mol% SiC; square: 29.74 mol% SiC; upward triangle: 58.92 mol% SiC; downward triangle: 27.91 mol% SiC – 3.32 mol% TaB<sub>2</sub>. In this figure, symbols are used only to identify traces; each TG trace is made up of ~1000 data pairs.

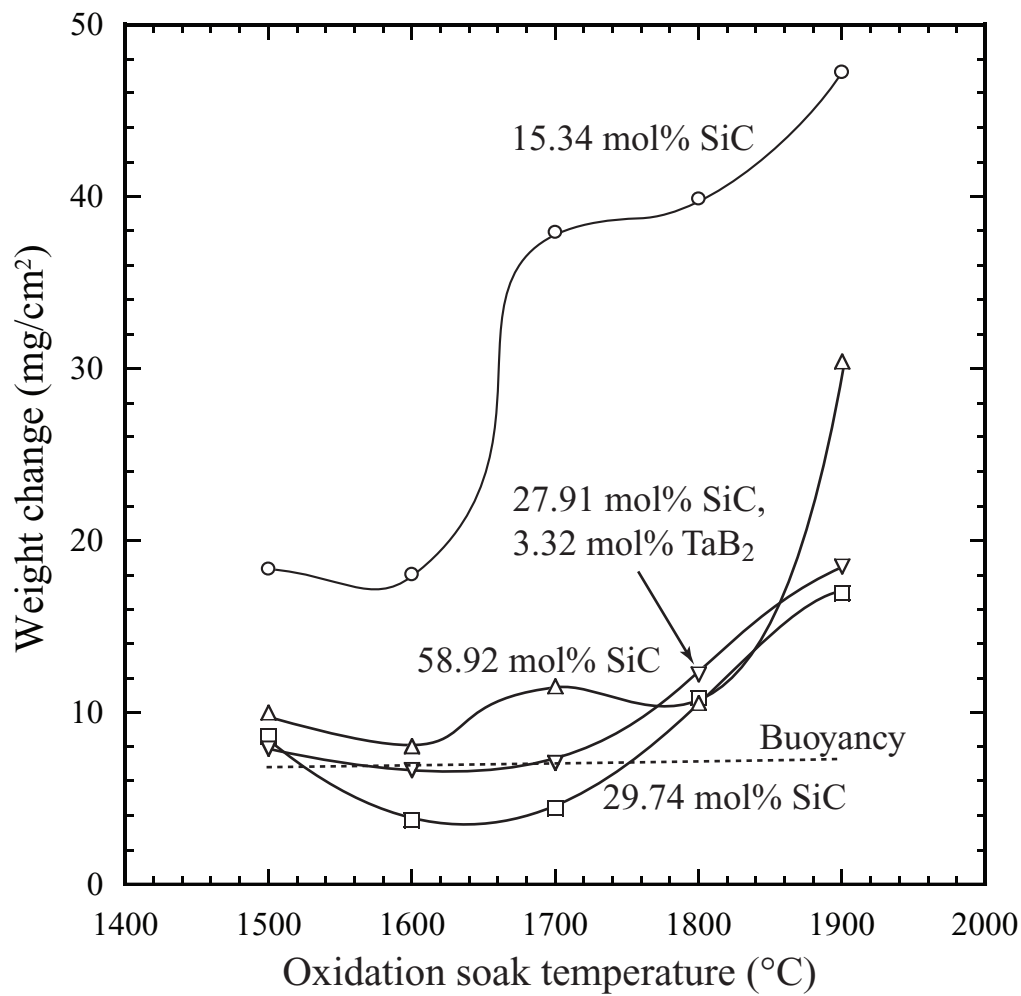


**Figure 12:** Weight change of various compositions exposed to flowing air at various temperatures after 100 min of oxidation. Extrapolated values were used for oxidations which were completed before 100 min. Experimental data are not corrected for buoyancy effects, which are separately displayed in the figure (dashed line).

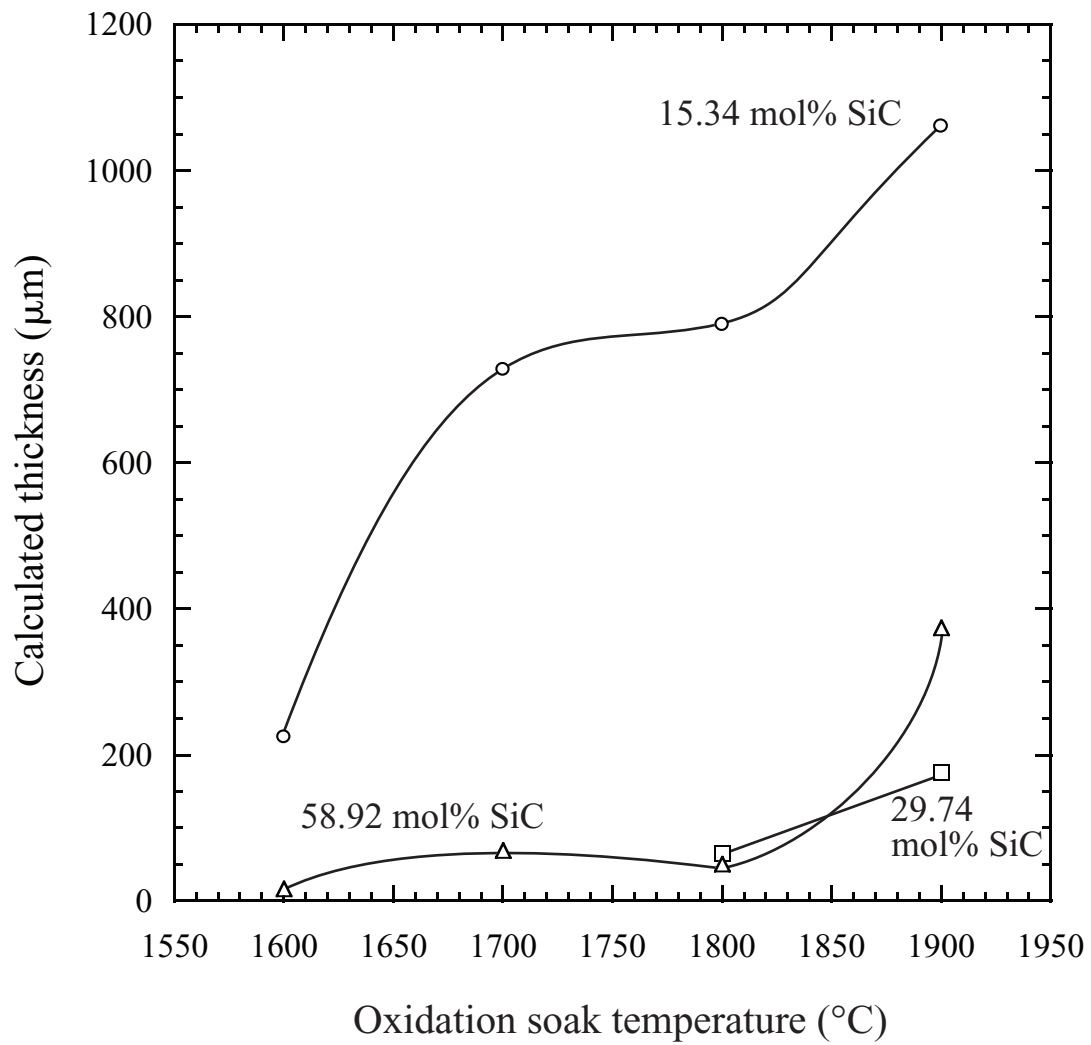


**Figure 13:** Oxide coating thicknesses based on measured weight losses.

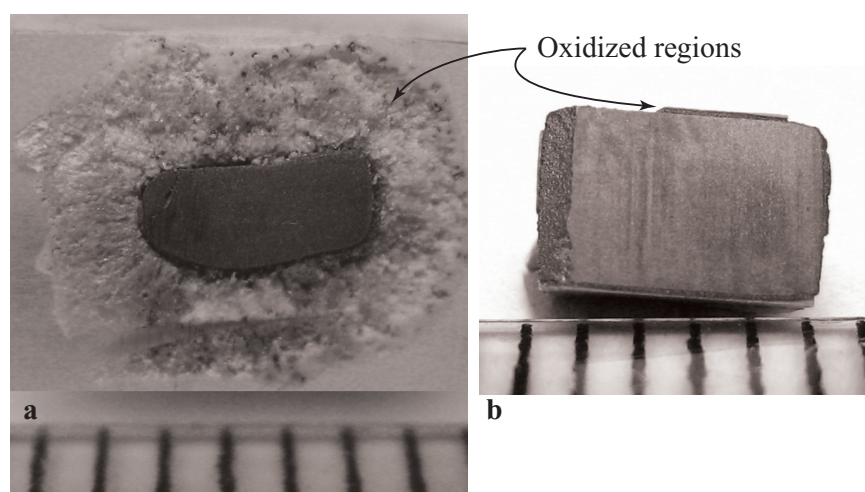


**Figure 14:** Cross sections (via diamond wafering blade) of specimens heat-treated at  $1800^{\circ}\text{C}$  for  $\sim 90$  min. a) 15.34 mol% SiC. b) 27.91 mol% SiC. The ruled lines are 1 mm apart. The specimen in a) was mounted in the crucible in the furnace such that the bottom of the part is out of the page, and the top extends into the page. The reaction layer in b) is not uniform as portions of it snapped off as the displayed axial cross-section was being cut.

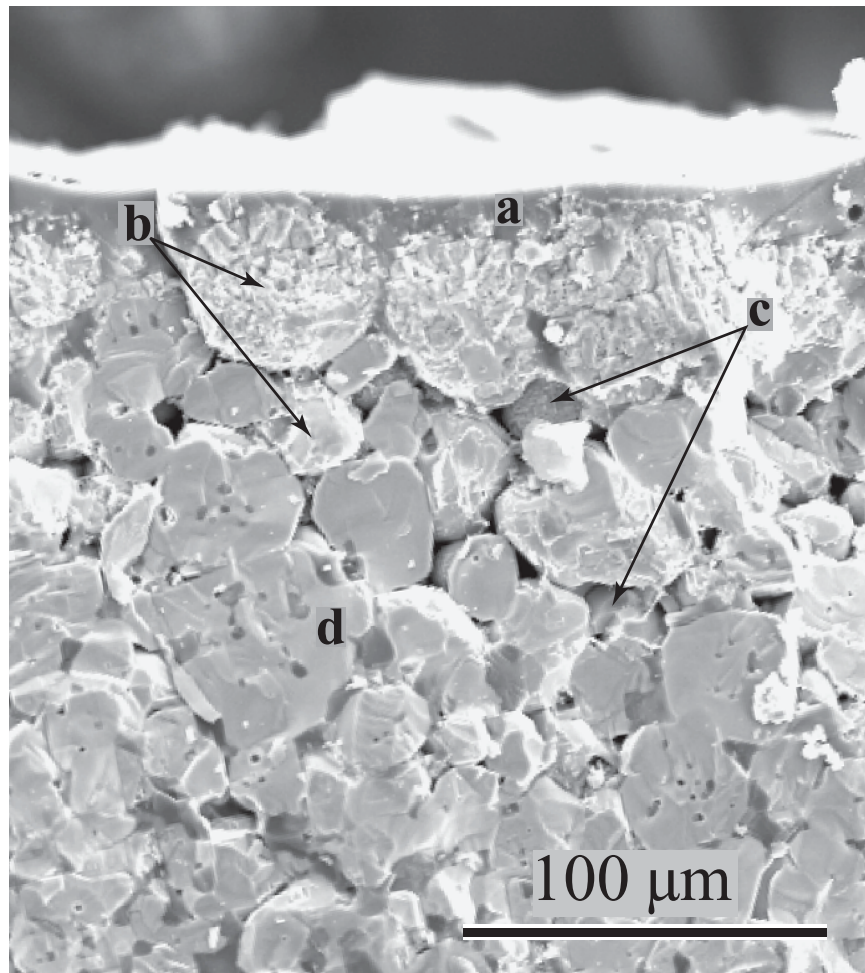


**Figure 15:** ~15 mol% SiC specimen oxidized at 1600°C for ~90 min. Marker "a" indicates the amorphous silica-containing layer, "b" the fragmented zirconia, "c" the porosity from the missing SiC, and "d" the untransformed bulk.

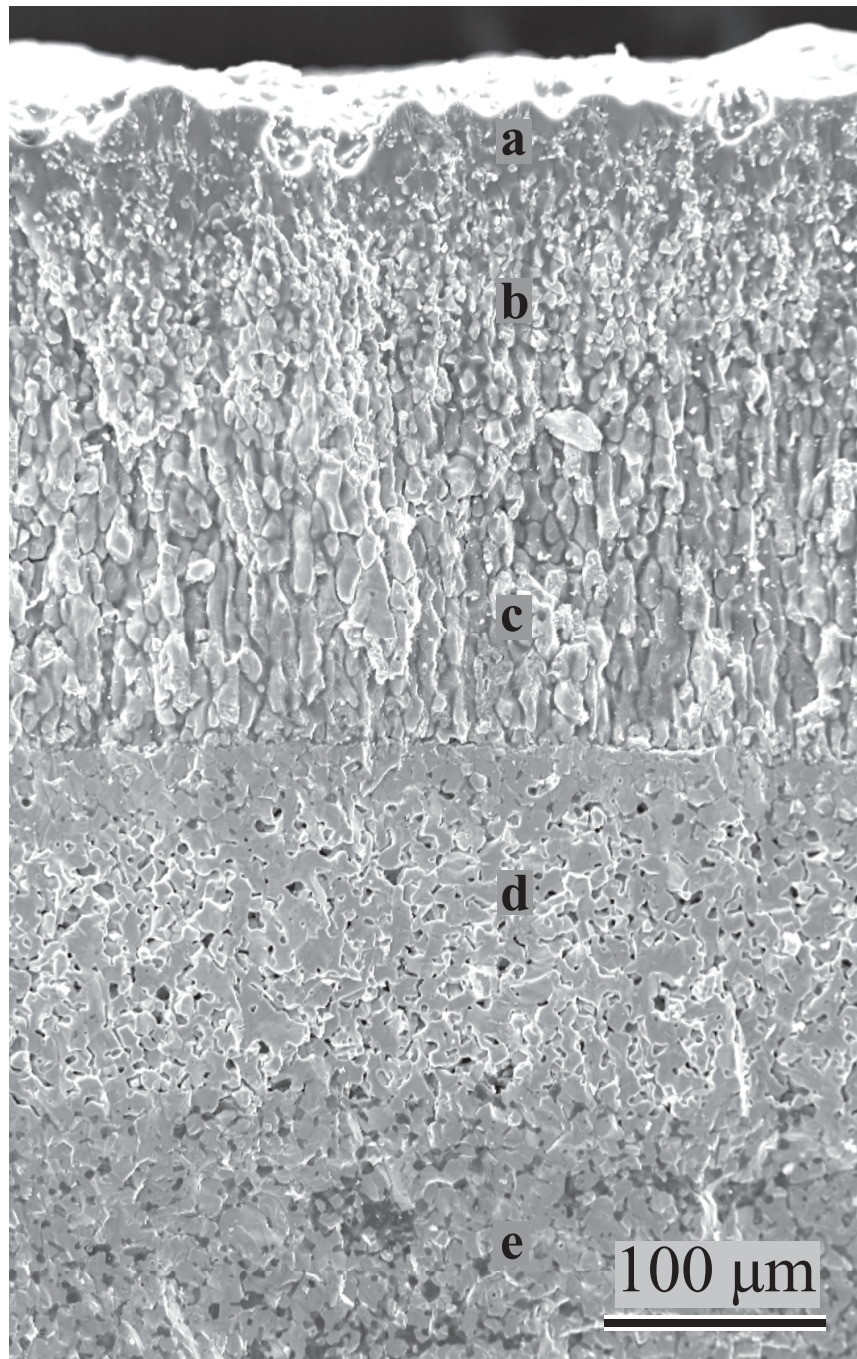


**Figure 16:** ~15 mol% SiC specimen oxidized at 1800°C for ~90 min. Marker "a" indicates the amorphous silica-containing layer with embedded zirconia, "b" the fragmented zirconia infused with silica-containing glass, "c" the transition zone with zirconia devoid of glass, "d" the SiC-depleted zone, and "e" the untransformed bulk.

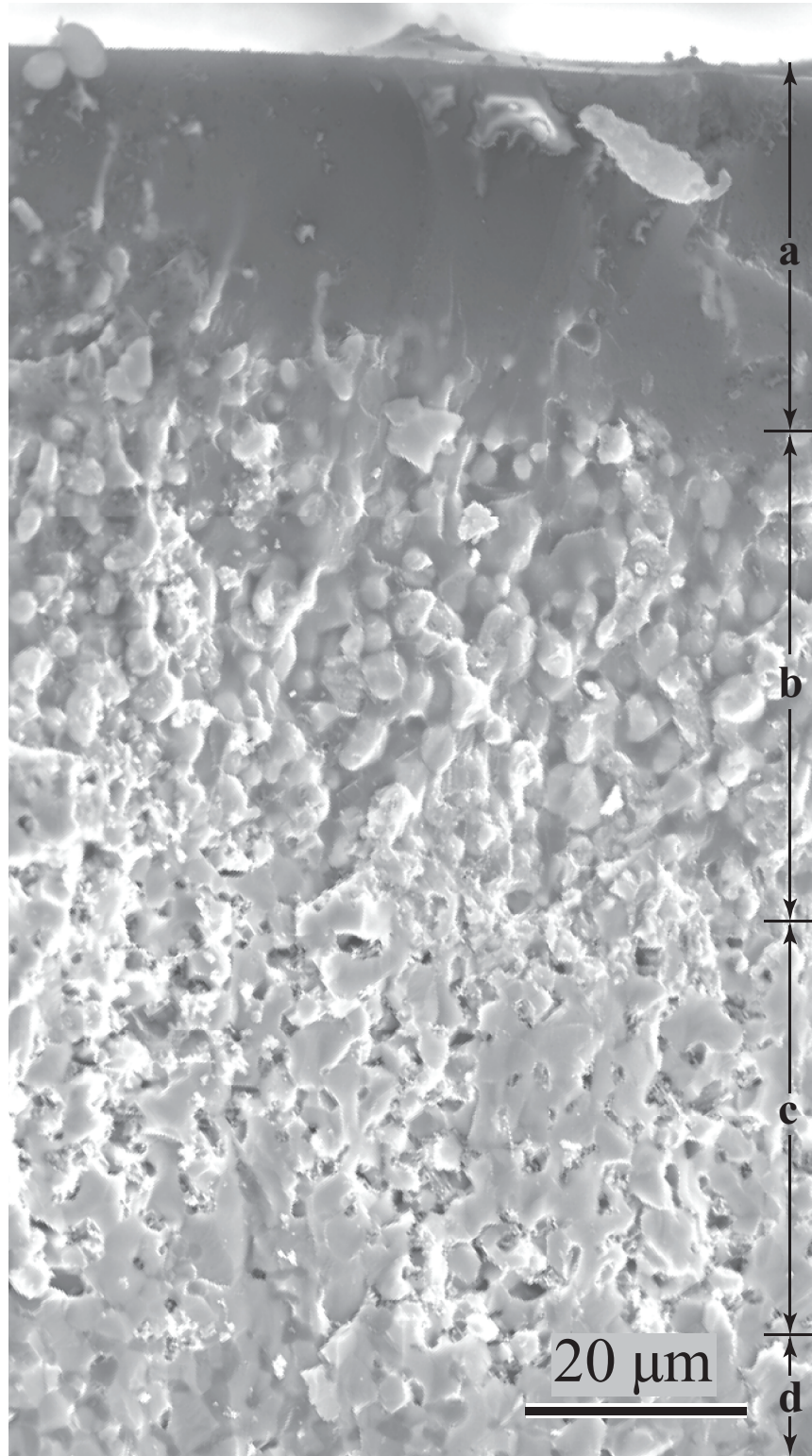


**Figure 17:** ~30 mol% SiC specimen oxidized at 1700°C for ~90 min. Marked regions: a) Glassy region adjacent to the surface. b) Zirconia particles immersed in silicate glass. c) ZrB<sub>2</sub> regions depleted of SiC. d) Un-transformed ZrB<sub>2</sub>-SiC.

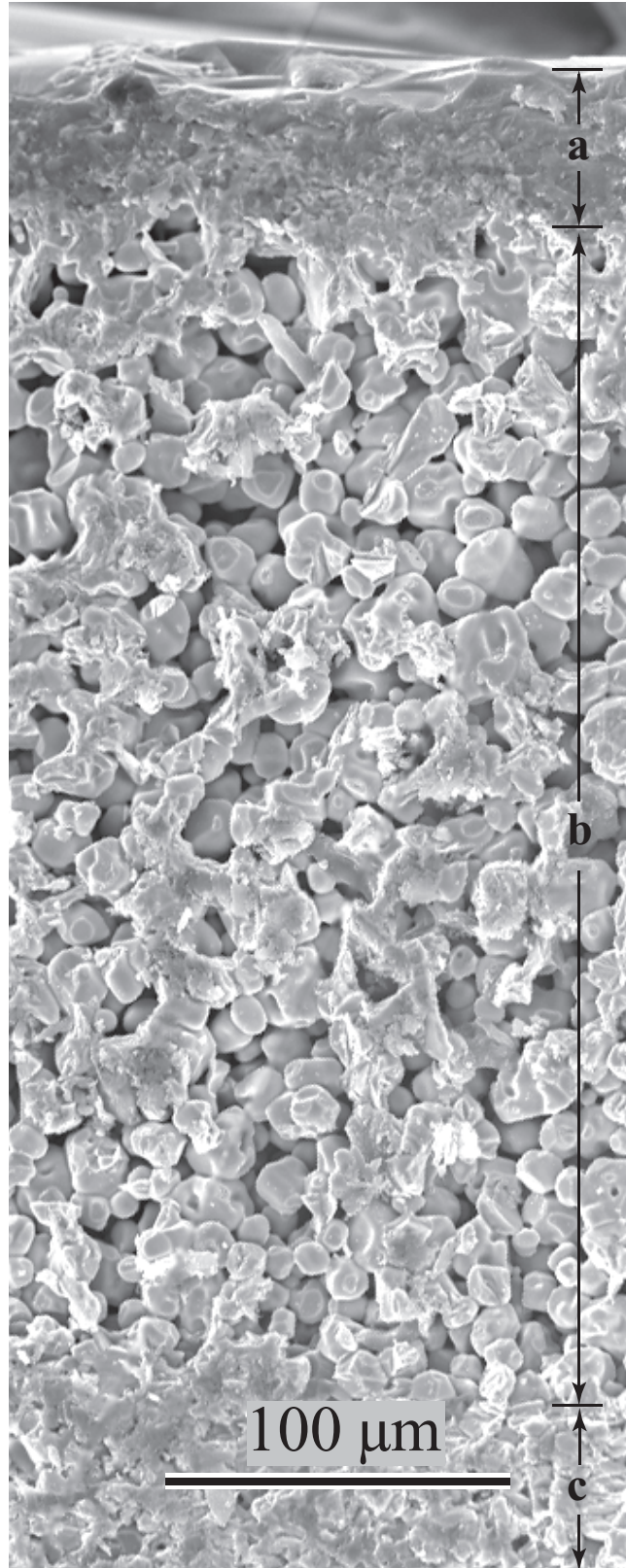


**Figure 18:** ~30 mol% SiC specimen oxidized at 1900°C for ~90 min. Marked regions: a) Glassy region adjacent to the surface. b) ZrB<sub>2</sub> regions depleted of SiC. c) Un-transformed ZrB<sub>2</sub>-SiC.

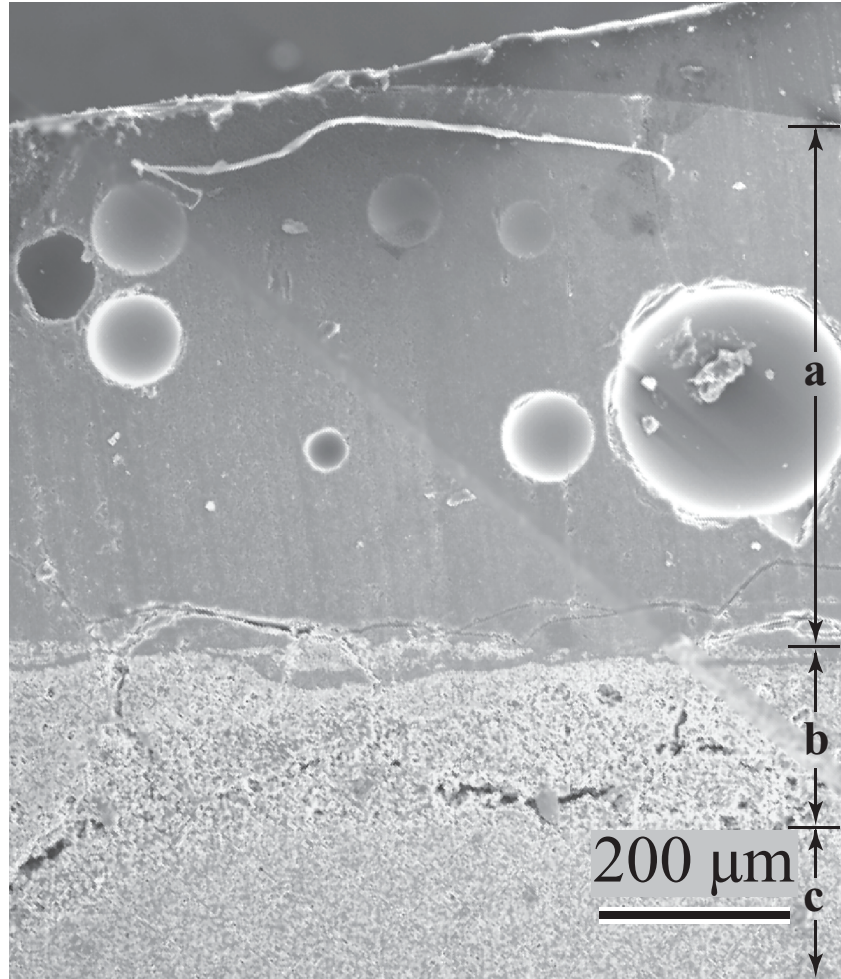


**Figure 19:** Comparatively low-magnification of  $\sim 60$  mol% SiC specimen oxidized at  $1900^\circ\text{C}$  for  $\sim 90$  min. a) Glassy layer with imbedded bubbles. b)  $\text{ZrB}_2$  with regions which had SiC replaced by porosity. Cracks/fissures in this layer are interpreted to have resulted from stresses via differences in coefficient of thermal expansions during cooling. c) Un-transformed  $\text{ZrB}_2$ -SiC.

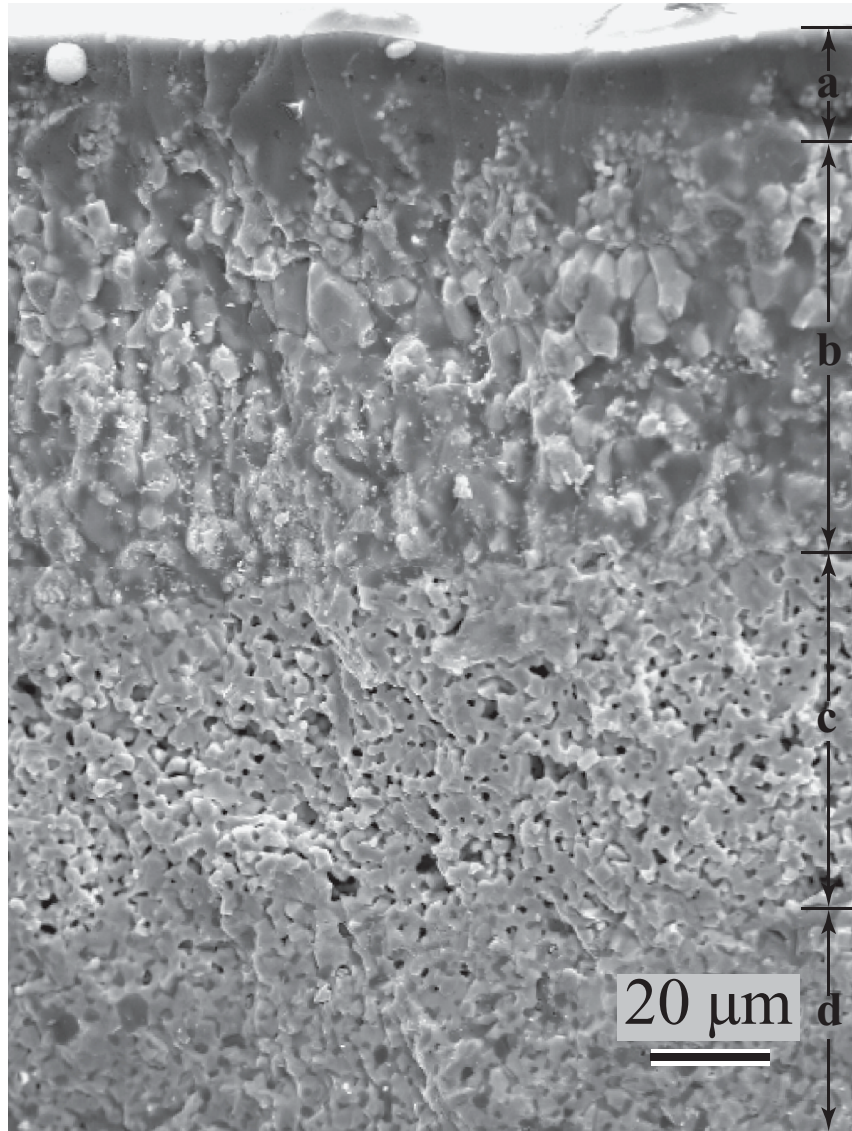


**Figure 20:**  $\sim 28$  mol% SiC -  $\sim 3$  mol% TaB<sub>2</sub> specimen oxidized at 1900°C for  $\sim 90$  min. Letter markers correspond to the same region types as in Figure 17. Marked regions: a) Glassy region adjacent to the surface. b) Zirconia particles immersed in silicate glass. c) ZrB<sub>2</sub> regions depleted of SiC. d) Un-transformed ZrB<sub>2</sub>-SiC.

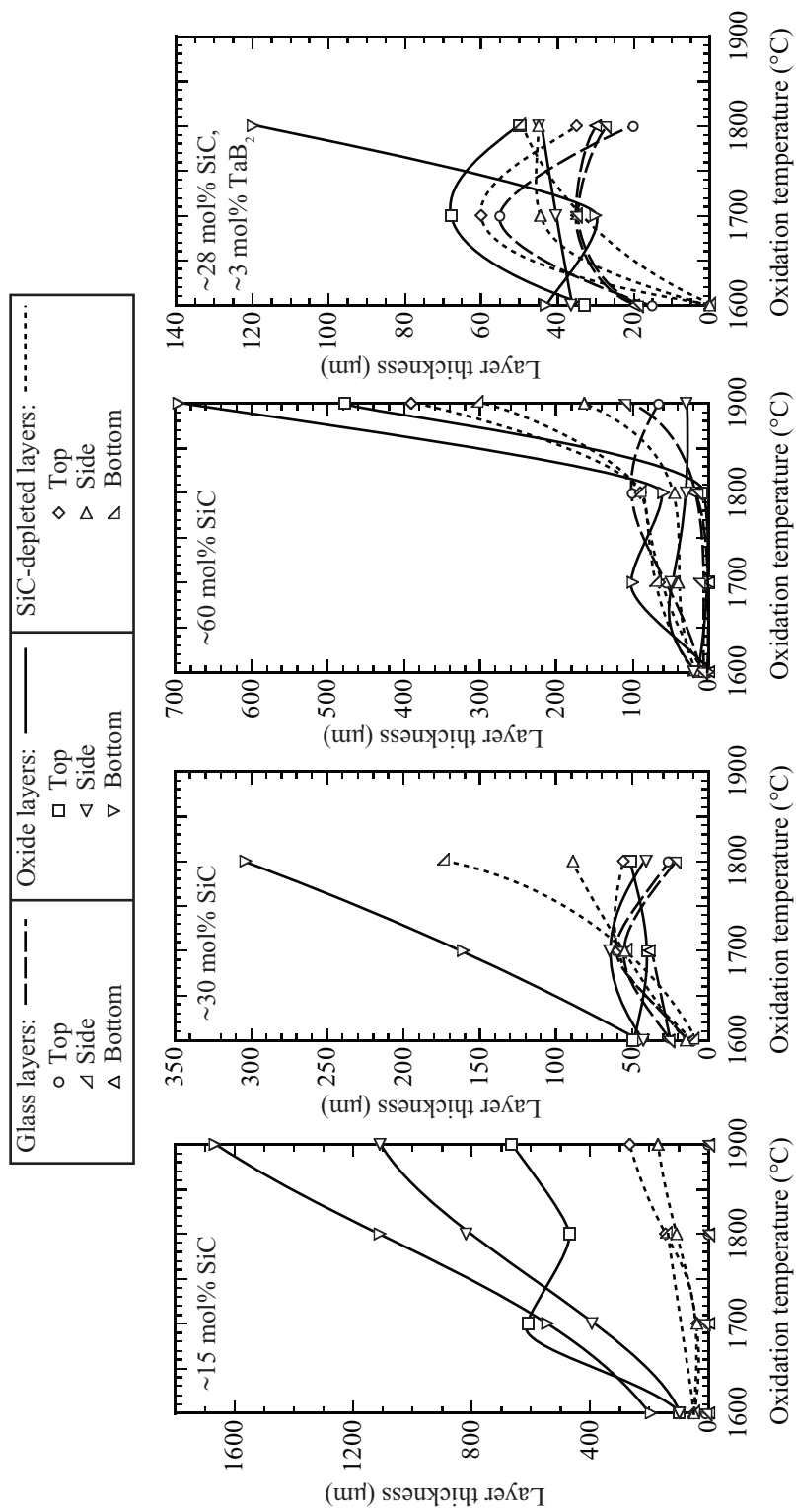


**Figure 21:** Thicknesses of various layers, as measured in the SEM, of oxidation-altered ZrB<sub>2</sub>-based ceramics.

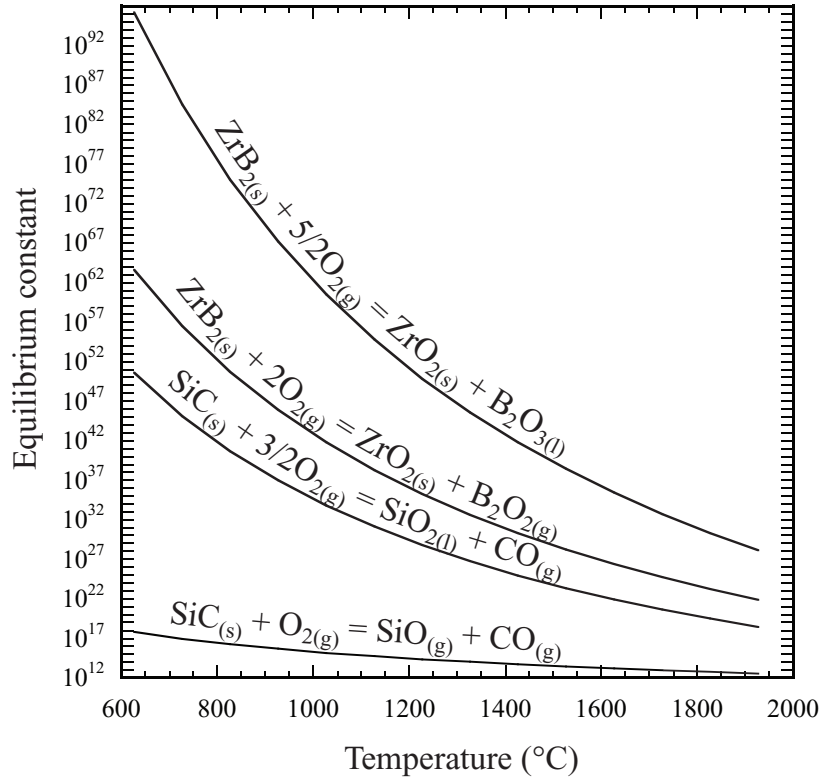


**Figure 22:** Equilibrium constant versus temperature as calculated by the expression  $\Delta G_{\text{rxn}}^{\circ} = -RT \ln k_p$  where  $\Delta G_{\text{rxn}}^{\circ}$  is the standard (1 bar) Gibbs energy of reaction,  $R$  is the gas constant,  $T$  is absolute temperature, and  $k_p$  is the equilibrium constant.  $k_p = 1/p_{\text{O}_2}^{5/2}$ ,  $k_p = p_{\text{B}_2\text{O}_2}/p_{\text{O}_2}^2$ ,  $k_p = p_{\text{CO}}/p_{\text{O}_2}^{3/2}$ ,  $k_p = p_{\text{CO}}p_{\text{SiO}}/p_{\text{O}_2}$ , for the highest to lowest traces, respectively. Standard Gibbs energies of reactions were based on the Gibbs energies of formation of compounds [?].

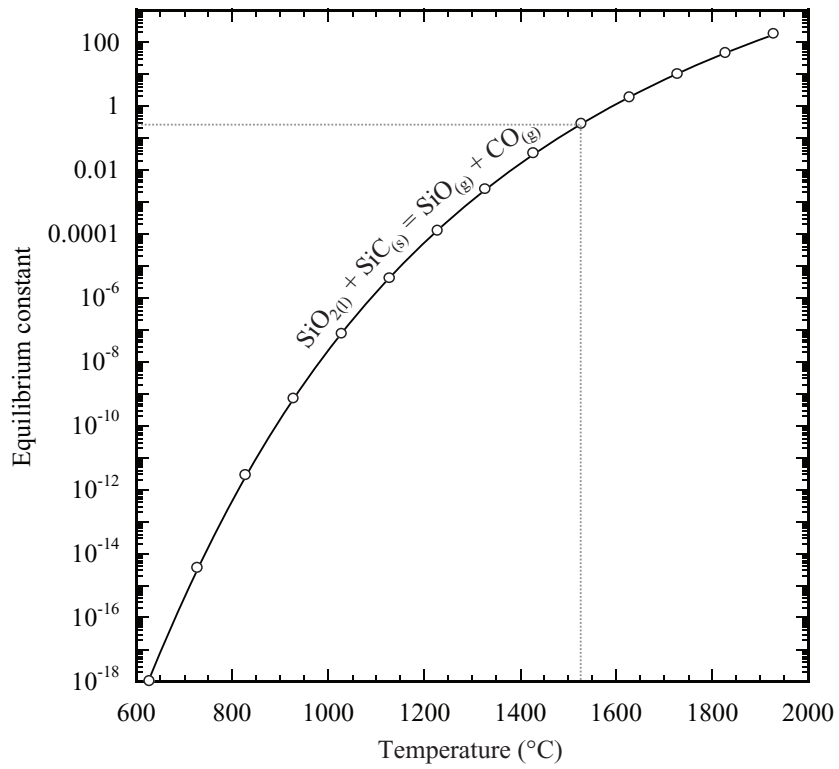


**Figure 23:** Equilibrium constant versus temperature for the indicated equilibria. For this reaction,  $k_p = p_{\text{CO}}p_{\text{SiO}}$

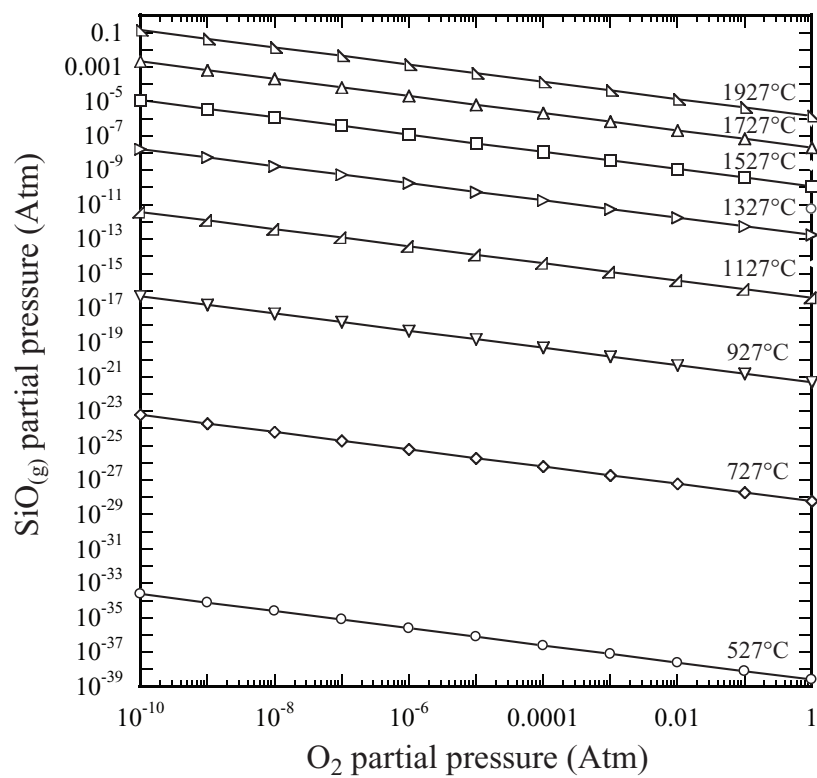


**Figure 24:** SiO<sub>(g)</sub> partial pressure as a function of oxygen partial pressure and temperature for the equilibria:  $\text{SiO}_{2(l)} = \text{SiO}_{(g)} + (1/2)\text{O}_{2(g)}$ .

## CHAPTER IV

### DETERMINATION OF THERMAL CONDUCTIVITY OF ZrB<sub>2</sub>-BASED CERAMIC COMPOSITES

#### 4.1 *Experimental Procedure*

Commercially-available ZrB<sub>2</sub> (Grade B,  $d_{50} = 2.20 \mu\text{m}$ , H. C. Starck, GmbH),  $\alpha$ -SiC (Grade 8S490NDP,  $d_{50} = 0.88 \mu\text{m}$ , Superior Graphite, Chicago, IL), and B<sub>4</sub>C (Grade HS,  $d_{50} = 0.8 \mu\text{m}$ , H. C. Starck) powders were used for raw materials. The compositions of synthesized powder mixtures are given in Table 3. Powders were ethanol-washed, and then mixed in aqueous suspension

**Table 3:** Sample Compositions for Thermal Diffusivity Specimens

Code	Mole Percent			Volume Percent			Mass Percent		
	ZrB <sub>2</sub>	B <sub>4</sub> C	SiC	ZrB <sub>2</sub>	B <sub>4</sub> C	SiC	ZrB <sub>2</sub>	B <sub>4</sub> C	SiC
ZBS2	77.39	7.27	15.34	80.36	8.92	10.72	89.57	4.12	6.31
ZBS10	64.25	6.04	29.70	70.32	7.82	21.87	82.63	3.80	13.57
ZBS26	37.55	3.53	58.92	46.15	5.13	48.72	62.36	2.87	34.77

with binder, dried, screened, uniaxially pressed into cylindrical pellets, cold isostatically pressed, and then exposed to thermolysis, sintering, and hot isostatic pressing heat (and pressure) treatment steps to form fully dense multi-phase bodies. This synthesis methodology is described in detail in the previous section. All HIPed specimens were 100% dense based on theoretical densities calculated from the rule of mixtures. The specimens were 12.7 mm in diameter by 2.0-2.1 mm in thickness.

Thermal diffusivity was measured by the flash method using a Netzsch

LFA 427 instrument, following the “Standard Test Method for Thermal Diffusivity by the Flash Method” standard ASTM E1461-01. The principle of the measurement is to irradiate (neodymium YAG laser, 1.06  $\mu\text{m}$ ) one radial face of the specimen with a short burst of energy (0.3-1.2 ms pulse width). An infrared pyrometer (InSb IR detector) measures the back face temperature, which quickly rises from the ambient temperature (established with a surrounding furnace, feedback controlled via a thermocouple). If the specimen is adiabatic with respect to its surroundings during the time period of the experiment, then the back face temperature would rise to a saturation temperature as temperature equilibrated throughout the part (generally 0.5-2°C). In one embodiment, the time required to reach the mid-point in temperature between the starting ambient temperature and the saturation temperature,  $t_{1/2}$  would be measured from the data. If it was further assumed that the energy pulse time period was negligible compared to  $t_{1/2}$ , then the Parker [42] expression may be used to determine the thermal diffusivity:

$$D = \frac{0.1388a^2}{t_{1/2}}$$

where  $a$  is the specimen thickness.

In this work, the above assumptions were not made; rather, the software accounted for radial and axial heat loss and the effect of a finite pulse period [43, 44]. A non-linear regression routine was used, fitting to the entire time-temperature curve ( $\sim 2000$  points), adjusting both diffusivity and loss factor to best fit the data.

All the samples were coated with approximately 10  $\mu\text{m}$  graphite to improve the absorption of radiation. Samples of each of the three compositions were evaluated at 25, 400, 800, 1200, 1600, and 1950°C, with some variation, with multiple measurements made at each temperature.

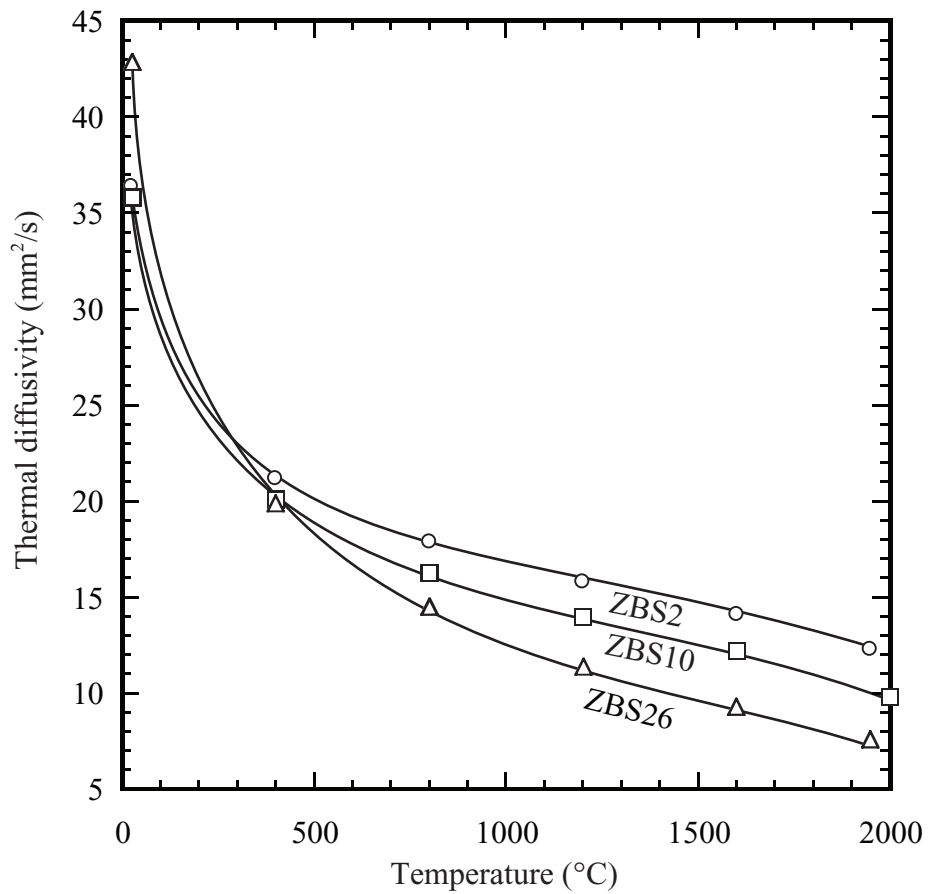
## 4.2 Results and Discussion

Figure 25 shows the results of the laser flash thermal diffusivity measurements on the three compositions. At any given temperature above 400°C, thermal diffusivity decreased with increasing SiC concentration. At room temperature, the composition with the highest SiC concentration had the highest thermal diffusivity.

Thermal diffusivity  $D$  (m<sup>2</sup>/s) was translated to thermal conductivity  $k$  (W/m·K) using the specific heat  $c_p$  (J/g·K) and density  $\rho$  (g/m<sup>3</sup>):  $k = D\rho c_p$ . Heat capacities for the individual phases (ZrB<sub>2</sub>, SiC, and B<sub>4</sub>C) were taken from JANAF [45] data, and converted to specific heats using molar masses. The specific heats of the three compositions (shown in Figure 26) were calculated from a mass-based rule of mixtures using the as-batched compositions. Room temperature theoretical densities of the individual phases [46] were converted to values at other temperatures using thermal expansion data for ZrB<sub>2</sub> [47],  $\alpha$ -SiC [48], and B<sub>4</sub>C [49]. Linear coefficients of thermal expansion  $\alpha_l$  were converted to volume coefficients  $\alpha_V$  by:  $\alpha_V = 3\alpha_l$ . The temperature-dependence of theoretical densities were then determined by:

$$\rho = \frac{\rho_0}{1 + \alpha_V \Delta T}$$

where  $\rho_0$  is the 25°C density, and  $\Delta T$  is the temperature difference with 25°C. These values were then used in a volume-based rule of mixtures calculation of the temperature-dependent theoretical densities for the three compositions (Figure 26). Using these data, the thermal conductivities of the three compositions were calculated (using linear interpolation to line-up data points), and are shown in Figure 27. The temperature and compositional dependencies of thermal conductivities followed similar trends as those followed by the original thermal diffusivity data.



**Figure 25:** Thermal diffusivity measured by the laser flash technique over the temperature range of room temperature to  $\sim 2000^{\circ}\text{C}$ .

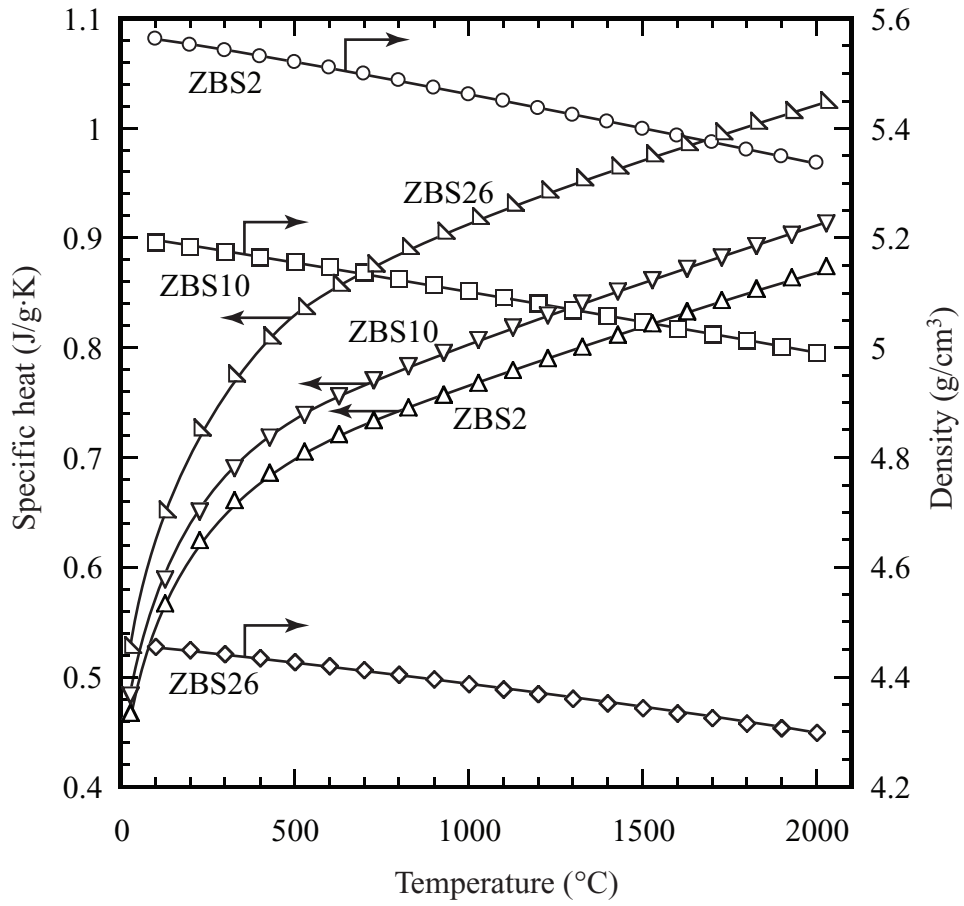


**Figure 26:** Temperature dependencies of specific heat and theoretical density for three compositions of  $\text{ZrB}_2\text{-SiC-B}_4\text{C}$ . Symbols for specific heat correspond to temperatures of JANAF heat capacity data. Symbols for theoretical density have no meaning other than curve identification.

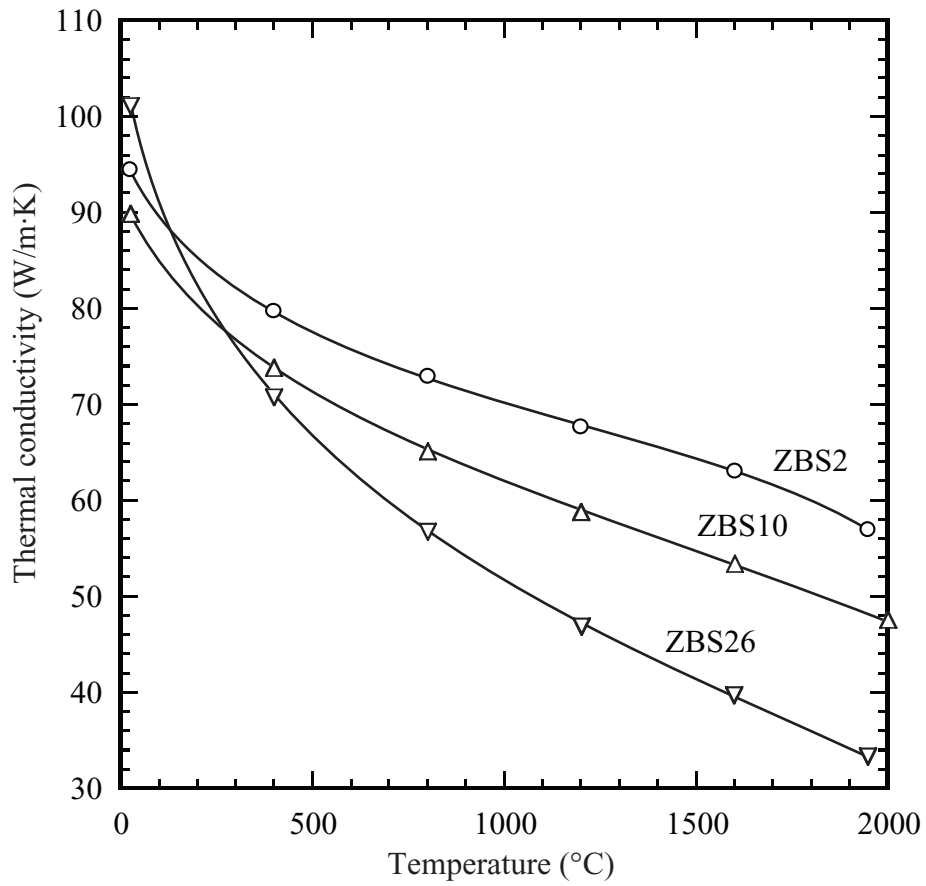


**Figure 27:** Thermal conductivities calculated from thermal diffusivity, specific heat, and theoretical density data.

Figure 28 shows the thermal conductivities of SiC, B<sub>4</sub>C, ZrB<sub>2</sub> and ZrB<sub>2</sub>-SiC mixtures from the literature. The agreement among the various sources for SiC and B<sub>4</sub>C is relatively good, while the two sources of ZrB<sub>2</sub> and ZrB<sub>2</sub>-SiC data are relatively more divergent. Above room temperature, the decrease in thermal conductivity of SiC emulates that of a dielectric (though it is actually a semiconductor), while ZrB<sub>2</sub> behavior is more typical of an electrical conductor. Thus for a multi-phase microstructure at room temperature, SiC is thermally conductive relative to ZrB<sub>2</sub>, while at the high end of the measured spectrum, SiC is thermally insulating relative to ZrB<sub>2</sub>. This is consistent with the trends observed in Figure 27. Thermal conductivities in ZBS10 are  $\sim 10$  W/m·K lower than Tye et al.'s results [57] for a similar composition.

The literature data in Figure 28 were used in a finite-difference [59] calculation. The microstructures of the three compositions fabricated in this work are shown in Figure 29. These microstructures were mathematically divided up into  $80 \times 20$  grids, and the majority phase in each cell was assigned to be the thermal conductivity of that cell (shown as distinct colors in Figure 30b). In the case of ZBS26, a small amount of porosity (likely grain pull-outs) was indicated in the microstructure; cells with this as the predominant phase were assigned a thermal conductivity of 0.05 W/m·K. Based on this construction, the microstructures indicate compositions for ZBS2 (80.2% ZrB<sub>2</sub>, 10.9% SiC, 8.9% B<sub>4</sub>C), ZBS10 (68.2% ZrB<sub>2</sub>, 22.8% SiC, 9.0%B<sub>4</sub>C), and ZBS26 (47.9% ZrB<sub>2</sub>, 48.0% SiC, 4.1% B<sub>4</sub>C), which are remarkably close to the as-batched compositions (volume percent) listed in Table 3.

The finite difference method was applied as depicted in Figure 31. Nodes were assigned to be at the centers of each cell. The temperatures at the left and right edges of the microstructure (cell array) were assigned to fixed values of 5°C above (left side) and 5°C below (right side) a specified temperature. Heat

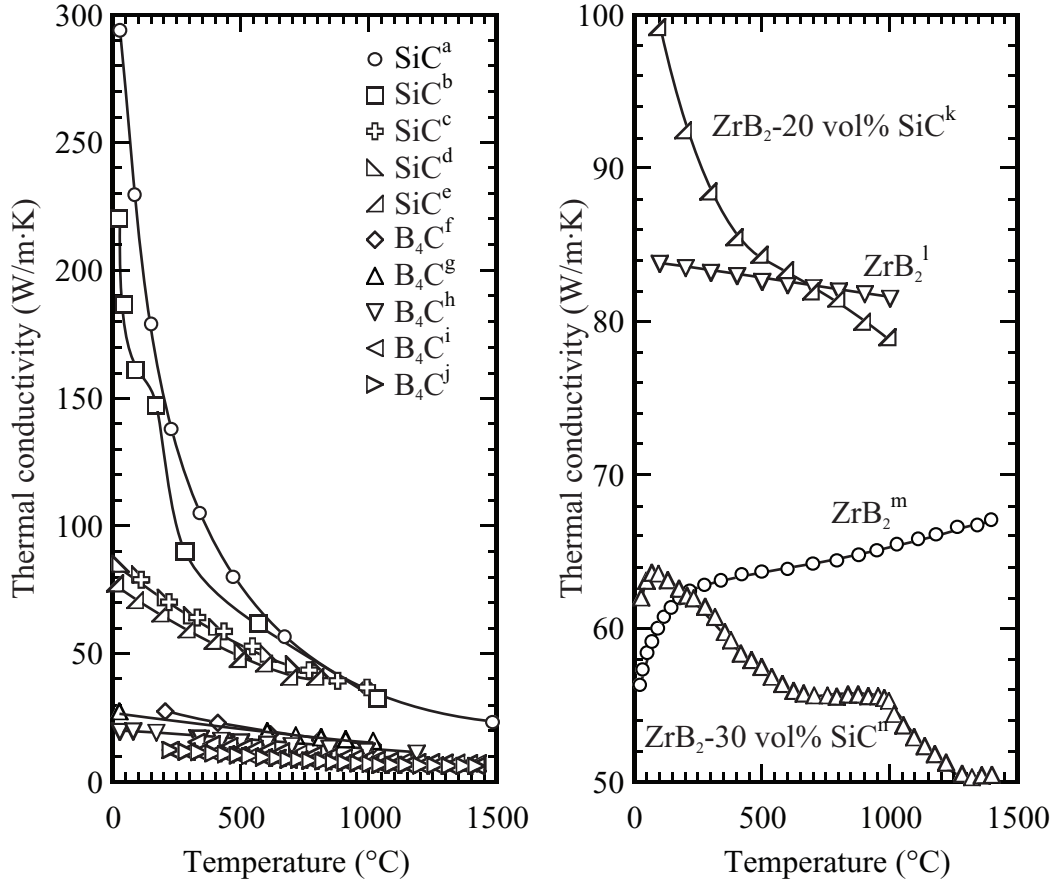


**Figure 28:** Left: literature values of thermal conductivity for B<sub>4</sub>C and SiC. a. Single crystal SiC (R66) plotted in Watari et al. [50], based on Slack [51]. b. Mixture of  $\alpha$  and  $\beta$  SiC hot pressed with BeO sintering aid, 100% dense [50]. c. (pre-) Hexoloy SA (Saint Gobain, Niagara Falls, NY)  $\alpha$ -SiC, 98% relative density [48]. d. 95 vol%  $\alpha$ -SiC - 5 vol%  $\beta$ -SiC, hot-pressed [52]. e. 76 vol%  $\beta$ -SiC - 24 vol%  $\alpha$ -SiC, hot-pressed [52]. f. B<sub>4</sub>C corrected for porosity [53]. g. B<sub>4</sub>C data of Gilchrist and Preston [54] as plotted by Bouchacourt [53]. h. Spark-plasma sintered B<sub>4</sub>C (not isotopically enriched), 98% relative density [55]. i. EP (Eagle-Pitcher) hot-pressed B<sub>4</sub>C [56]. j. Hot-pressed B<sub>4</sub>C, 98% relative density [56]. Right: literature values of thermal conductivity for ZrB<sub>2</sub> and ZrB<sub>2</sub>-SiC. k. Hot-pressed ZrB<sub>2</sub> - 20 vol% SiC [57]. l. Hot-pressed ZrB<sub>2</sub> [57]. m. Hot-pressed ZrB<sub>2</sub> [58]. n. Hot-pressed ZrB<sub>2</sub>-30 vol% SiC [58].

flow was assumed to be two-dimensional, with the third dimension being of unit dimension. The upper and lower edges were assumed to be adiabatic. The adiabatic boundary for the upper and lower edges was positioned directly on the nodes for mathematical convenience. Steady state heat flow was assumed, and the temperature gradients between neighboring cells was assumed to be linear. Under these conditions, the sum of heat flows into and out of each node must be zero. Such equations fall into categories a-i, as shown in Figure 31 and the following expressions:

$$a. \quad \frac{T_{m,n} - T_{m,n+1}}{\frac{1}{k_{m,n+1}} + \frac{1}{k_{m,n}}} + \frac{T_{m,n} - T_{m,n-1}}{\frac{1}{k_{m,n-1}} + \frac{1}{k_{m,n}}} + \frac{T_{m,n} - T_{m-1,n}}{\frac{1}{k_{m-1,n}} + \frac{1}{k_{m,n}}} + \frac{T_{m,n} - T_{m+1,n}}{\frac{1}{k_{m+1,n}} + \frac{1}{k_{m,n}}} = 0$$

$$b. \quad \frac{T_{m,n} - T_{m+1,n}}{\frac{1}{k_{m+1,n}} + \frac{1}{k_{m,n}}} + \frac{T_{m,n} - T_{m-1,n}}{\frac{1}{k_{m-1,n}} + \frac{1}{k_{m,n}}} + \frac{2(T_{m,n} - T_{m,n-1})}{\frac{1}{k_{m,n-1}} + \frac{1}{k_{m,n}}} = 0$$

$$c. \quad \frac{T_{m,n} - T_{m-1,n}}{\frac{1}{k_{m-1,n}} + \frac{1}{k_{m,n}}} + \frac{T_{m,n} - T_{m+1,n}}{\frac{1}{k_{m+1,n}} + \frac{1}{k_{m,n}}} + \frac{2(T_{m,n} - T_{m,n+1})}{\frac{1}{k_{m,n+1}} + \frac{1}{k_{m,n}}} = 0$$

$$d. \quad k_{m,n}(T_{m,n} - T_{\text{left}}) + \frac{T_{m,n} - T_{m+1,n}}{\frac{1}{k_{m+1,n}} + \frac{1}{k_{m,n}}} + \frac{T_{m,n} - T_{m,n-1}}{\frac{1}{k_{m,n-1}} + \frac{1}{k_{m,n}}} + \frac{T_{m,n} - T_{m,n+1}}{\frac{1}{k_{m,n+1}} + \frac{1}{k_{m,n}}} = 0$$

$$e. \quad k_{m,n}(T_{m,n} - T_{\text{right}}) + \frac{T_{m,n} - T_{m-1,n}}{\frac{1}{k_{m-1,n}} + \frac{1}{k_{m,n}}} + \frac{T_{m,n} - T_{m,n-1}}{\frac{1}{k_{m,n-1}} + \frac{1}{k_{m,n}}} + \frac{T_{m,n} - T_{m,n+1}}{\frac{1}{k_{m,n+1}} + \frac{1}{k_{m,n}}} = 0$$

$$f. \quad k_{m,n}(T_{m,n} - T_{\text{left}}) + \frac{T_{m,n} - T_{m+1,n}}{\frac{1}{k_{m+1,n}} + \frac{1}{k_{m,n}}} + \frac{2(T_{m,n} - T_{m,n-1})}{\frac{1}{k_{m,n-1}} + \frac{1}{k_{m,n}}} = 0$$

$$g. \quad k_{m,n}(T_{m,n} - T_{\text{left}}) + \frac{T_{m,n} - T_{m+1,n}}{\frac{1}{k_{m+1,n}} + \frac{1}{k_{m,n}}} + \frac{2(T_{m,n} - T_{m,n+1})}{\frac{1}{k_{m,n+1}} + \frac{1}{k_{m,n}}} = 0$$

$$h. \quad k_{m,n}(T_{m,n} - T_{\text{right}}) + \frac{T_{m,n} - T_{m-1,n}}{\frac{1}{k_{m-1,n}} + \frac{1}{k_{m,n}}} + \frac{2(T_{m,n} - T_{m,n-1})}{\frac{1}{k_{m,n-1}} + \frac{1}{k_{m,n}}} = 0$$

$$i. \quad k_{m,n}(T_{m,n} - T_{\text{right}}) + \frac{T_{m,n} - T_{m-1,n}}{\frac{1}{k_{m-1,n}} + \frac{1}{k_{m,n}}} + \frac{2(T_{m,n} - T_{m,n+1})}{\frac{1}{k_{m,n+1}} + \frac{1}{k_{m,n}}} = 0$$

For the  $80 \times 20$  matrix, this generated 1600 simultaneous equations. Code for setting up the matrix and solving the simultaneous equations by matrix inversion was written in Visual Basic 4.0. The temperature-dependent thermal conductivities of the individual phases were taken as the average of the literature values (single-crystal SiC excluded). A depiction of the solution set of node temperatures for ZBS10 at  $1500^\circ\text{C}$  is shown in Figure 30c.

From these temperatures, the thermal conductivities of the multi-phase microstructures were then determined by calculating the heat flux from the left-end reservoir to the left edge nodes, and then determining an effective thermal conductivity through the entire microstructure based on a  $10^\circ\text{C}$  temperature gradient. The results of this calculation are shown in Figure 32. These data are consistent with those experimentally derived for these compositions (Figure 27); above  $400^\circ\text{C}$ , thermal conductivity decreased with increasing SiC concentration, and at room temperature, the specimen with the highest SiC content had the highest thermal conductivity. These data were lower in thermal conductivity for a given composition and temperature than those experimentally determined; agreement was closer at higher temperatures.

The finite difference method was used for a separate calculation in which the thermal conductivities of SiC and  $\text{B}_4\text{C}$  were taken as the average of literature values, as before. The thermal conductivities of the three compositions were taken from the experimentally-derived results herein, and the values of the thermal conductivities of the  $\text{ZrB}_2$  phase was back calculated. The determination was based on a numerical search routine written into the code, iterating seed values of  $k_{\text{ZrB}_2}$ , comparing the resulting calculated multi-phase thermal conductivity to that experimentally determined, generating a corrected seed

value, and so on, until the calculated and measured composite thermal conductivities were within 0.1 W/m·K. The results of these calculations are shown in Figure 33. With one exception (ZrB<sub>2</sub>:ZBS26 at 1600°C), calculated thermal conductivities were relatively constant at ~88-104 W/m·K, which is higher than the two literature data sets in Figure 28, being closer to the results of Tye et al. [57] than Zimmermann et al. [58]. The solution for ZBS26 at 1600°C was based on an extrapolated value of the averaged literature thermal conductivity for SiC from lower temperature values, which is likely unreliable. Since ZBS26 had the highest concentration of SiC, the 1600°C calculated thermal conductivity of ZrB<sub>2</sub>, now a minority phase, was substantially shifted upward to compensate for the assumed value of thermal conductivity of SiC.

### ***4.3 Conclusions***

Thermal conductivities in the temperature range 25-2000°C were calculated from laser-flash thermal diffusivity data, using specific heat, theoretical density, and thermal expansion data. The more dielectric-like behavior of the SiC imbued a greater temperature sensitivity to ZrB<sub>2</sub>-SiC-B<sub>4</sub>C multiphase ceramics with increasing SiC content. Finite difference calculations, using averaged literature values for the thermal conductivities of individual ZrB<sub>2</sub>, SiC, and B<sub>4</sub>C phases, correctly predicted the trends observed from experimental measurements; the composition with the highest SiC content (48.7 vol%) showed the highest room temperature thermal conductivity, but above ~400°C, demonstrated the lowest thermal conductivity. The temperature-dependent thermal conductivity of pure ZrB<sub>2</sub> was back-calculated using finite-difference calculations, experimental results for multi-phase compositions, and averaged literature values for SiC and B<sub>4</sub>C; it was relatively constant (88-104 W/m·K) over the full evaluated temperature range.

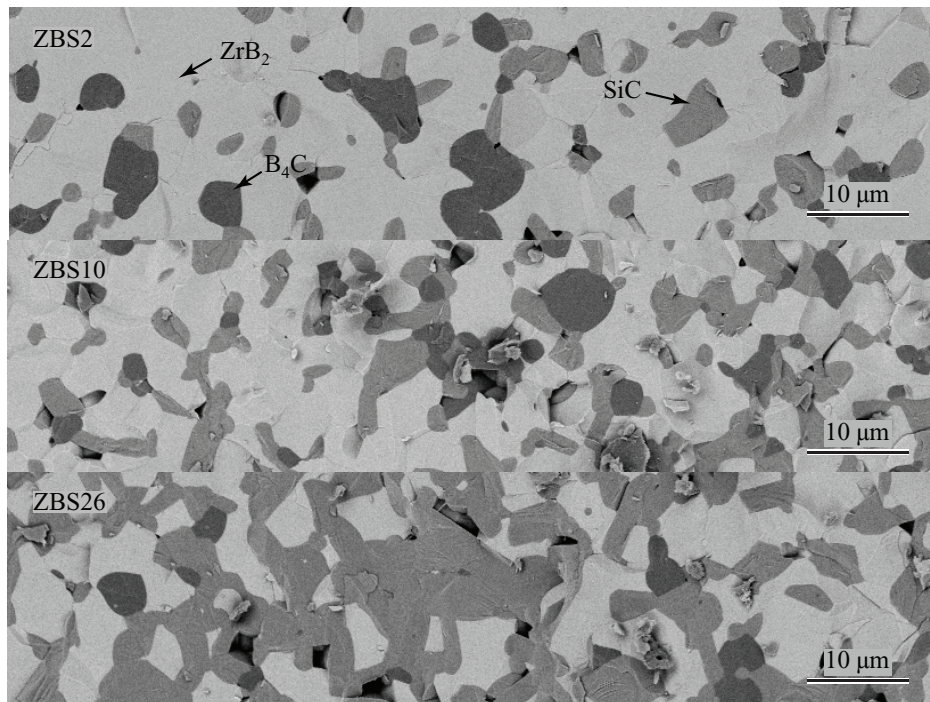


**Figure 29:** Fracture-surface microstructures of the three evaluated compositions. Phases are identified by compositional contrast as  $\text{ZrB}_2$ ,  $\text{SiC}$ , and  $\text{B}_4\text{C}$ , light to dark, respectively.

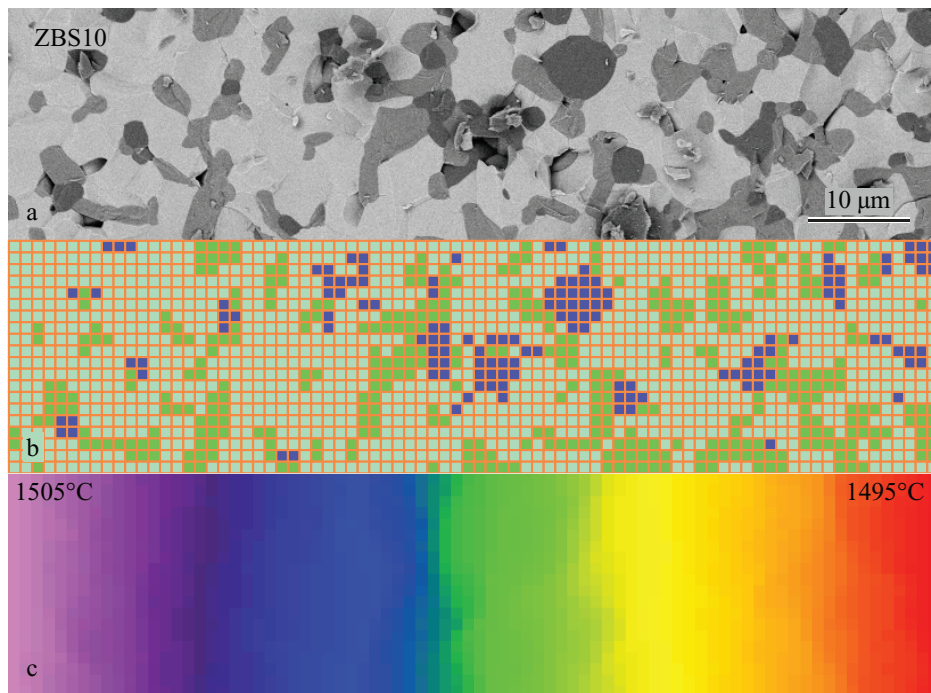


**Figure 30:** a. Electron micrograph of a ZBS10 fracture surface. b.  $80 \times 20$  grid with colors assigned to each cell based on the majority phase in that cell. c. Cells with rainbow coloring to indicate relative temperature; violet indicates highest temperature and red indicates lowest temperature. For ZBS10 at  $1500^\circ\text{C}$ :  $k_{\text{SiC}} = 21.0 \text{ W/m}\cdot\text{K}$ ,  $k_{\text{B}_4\text{C}} = 9.06 \text{ W/m}\cdot\text{K}$ ,  $k_{\text{ZrB}_2} = 73.78 \text{ W/m}\cdot\text{K}$ , based on averages of literature values.

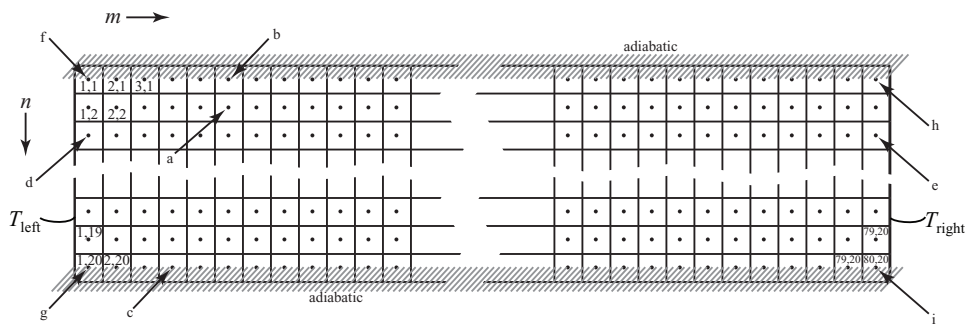


**Figure 31:** Depiction of  $80 \times 20$  cells/nodes indicating regions for node equations: a. Interior. b. Upper edge (insulated). c. Lower edge (insulated). d. Left edge (fixed temperature of  $5^\circ\text{C}$  above designated temperature). e. Right edge (fixed temperature of  $5^\circ\text{C}$  below designated temperature). f. Upper left corner. g. Lower left corner. h. Upper right corner. i. Lower right corner.

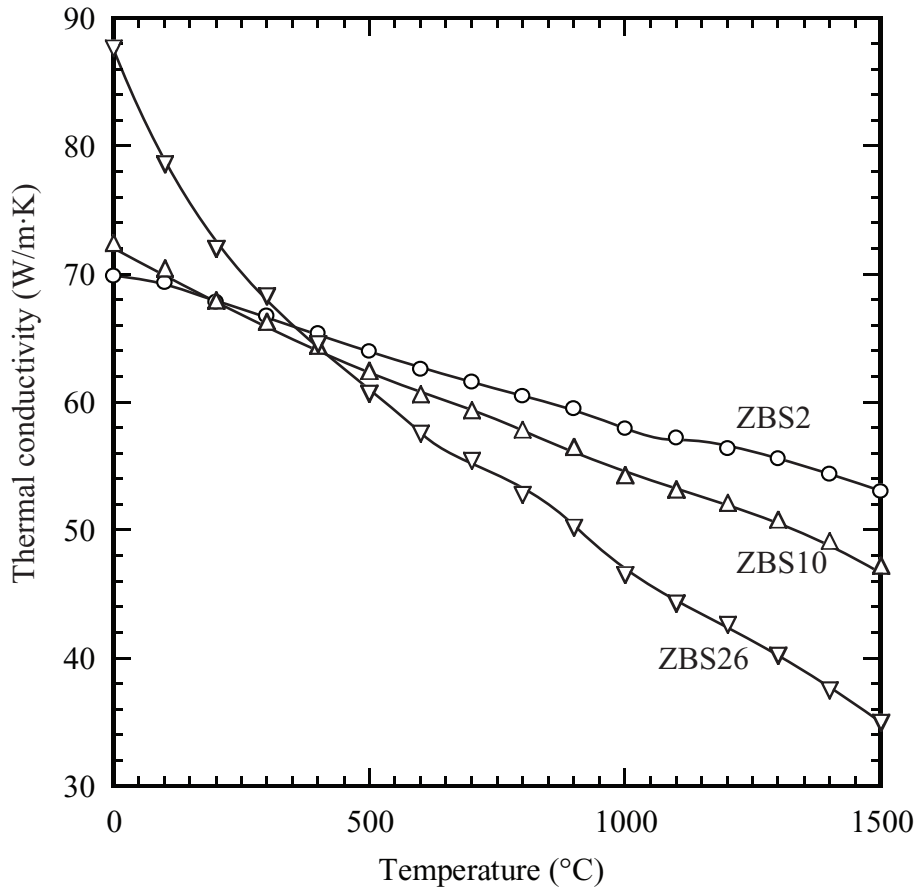


**Figure 32:** Thermal conductivity of three compositions calculated using averaged literature values of  $ZrB_2$ ,  $SiC$ , and  $B_4C$ , the distribution of phases based on a grid overlay of SEM micrographs, and the finite difference method.

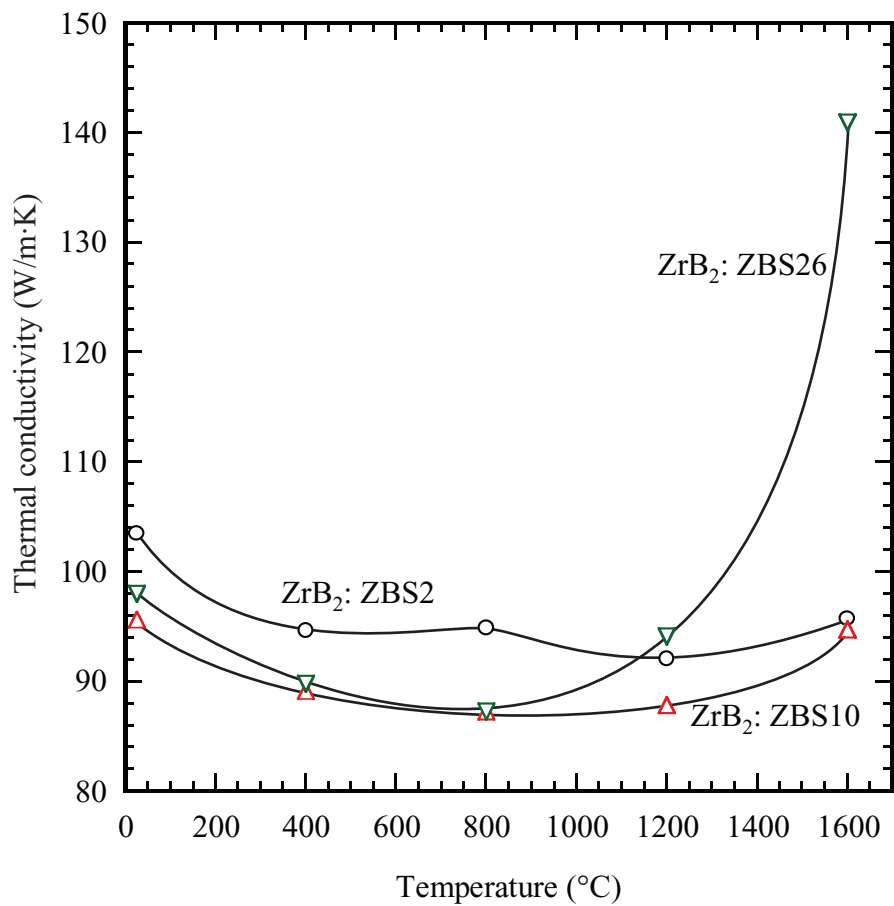


**Figure 33:** Thermal conductivity of ZrB<sub>2</sub> calculated based on thermal conductivities of ZrB<sub>2</sub>-SiC-B<sub>4</sub>C multi-phase microstructures and averaged literature thermal conductivities for SiC and B<sub>4</sub>C.

## CHAPTER V

### MEASUREMENT OF EMITTANCE OF ZRB<sub>2</sub>-BASED CERAMIC COMPOSITES

#### 5.1 *Experimental Procedure*

Theoretically dense test specimens were fabricated using techniques developed by Peng and Speyer [4]. Commercially available powders were used for raw materials. The major crystalline phase(s), grade, and suppliers are listed for each powder in Table 4.

**Table 4:** Raw Material Characteristics for Emittance Specimens

	Phases	Particle Size	Supplier
ZrB <sub>2</sub>	ZrB <sub>2</sub>	$d_{50} = 2.20 \mu\text{m}$	Grade B, H. C. Starck, GmbH
B <sub>4</sub> C	stoichiometric B <sub>4</sub> C	$d_{50} = 0.8 \mu\text{m}$	Grade HS, H. C. Starck, GmbH
SiC	$\alpha$ -SiC	$d_{50} = 0.88 \mu\text{m}$	8S490NDP, Superior Graphite, Chicago, IL

The composition of the synthesized powder mixture is given in Table 5. The specimens were produced following the same procedures as are detailed

**Table 5:** Sample Composition for Emittance Specimens

Code	Mole Percent			Volume Percent			Mass Percent		
	ZrB <sub>2</sub>	B <sub>4</sub> C	SiC	ZrB <sub>2</sub>	B <sub>4</sub> C	SiC	ZrB <sub>2</sub>	B <sub>4</sub> C	SiC
ZBS10	64.25	6.04	29.70	70.32	7.82	21.87	82.63	3.80	13.57

in the High Temperature Study portion of this document. Rectangular specimens were commercially machined (Advanced Ceramics Manufacturing, Tucson, AZ) to their final dimensions as self-supporting ribbons sized roughly 1 cm in height, 3 cm in length, and 0.3 mm in thickness in the thinned regions.

The experimental setup consisted of three main components: the Ribbon Testing Unit (RTU), the power control system, and the data collection apparatus. A schematic of the experimental setup can be seen in Figure 34.

The Ribbon Testing Unit (RTU) is a custom-designed and built chamber which supported the specimens and allowed observation of the specimens while they were at temperature (generally 1200°C) in a controlled atmosphere. The specimens were positioned in the center of the unit upon two large copper feed-through bus bars and held in place by a custom copper clamping system which provided an electrical connection to the thickened ends on either side of the thinned region. The specimens were oriented such that the broad sides of the ribbons (considered to be the "front" and "back") faced modular viewports through which a spectral radiometer and a pyrometer, respectively, could make observations (an accessory viewport vantage point was designed to observe the front of the ribbon at an angle of 45° from the surface normal, but this was not used in this work). The viewports were of a modular configuration to accommodate the full range of the measurement capabilities of the spectral radiometer. Specimens were loaded into the RTU via an O-ring sealed plate on the top of the unit. Accessory instrumentation could be mounted within the chamber and controlled via a 12-pin data passthrough attached to an accessory modular access port. Atmosphere control was accomplished via two 6.35 mm gas flow tubes on opposite sides of the ribbon. The inlet tube provided ultra-high purity argon at a known flowrate, and the outlet tube led to either a mechanical vacuum pump or a bubble flowback check valve, selected via a 3-way junction. Internal pressure of the chamber was monitored with a mechanical pressure guage mounted downstream on the outlet line.

The power control system itself consisted of three basic parts: a pyrometer

input, a computer running a control program, and a power supply unit controlled by output from the computer. Beginning with the input: the temperature of the specimens was observed from their "back" face through a fused silica viewport by a two-color pyrometer (Modline 5R, IRCON, Inc, Santa Cruz, CA) focused on a circle approximately 4 mm diameter in the center of the heated ribbon. These data were rapidly queried by a custom "PI" control program written in Visual Basic (the control software was capable of "PID" control, but no derivative control was deemed necessary given the negligible thermal momentum of the ribbon specimens). The two-color pyrometer was blind to temperatures below 1000°C, so specimens were heated to this point by a gradual linear power ramp until a valid signal was reported by the pyrometer. The output of the control system consisted of a 4-20 mA signal to an SCR which moderated the power delivered from a 280 V 60 Hz single-phase wall source to a series of two step-down transformers rigged to provide ~10 V potential across the ribbon samples.

Data collection was accomplished with a computer-controlled spectral radiometer (OL Series 750 Automated Spectroradiometric Measurement System, Gooch & Housego (formally Optronic Laboratories), Orlando, FL) which diffracts incoming radiation on a grated mirror mounted on a rotating turret, thereby directing specific wavelengths to a detector. The unit was capable of evaluating the spectral radiance of the specimens over a range of wavelengths from 350 to 16000 nm using one of two detectors: a silicon detector (350 to 1000 nm), and a liquid nitrogen-cooled CdHgTe detector (1000 to 16000 nm)(at 1400 K, over 98 percent of blackbody radiation is emitted at wavelengths less than 14000 nm [6]). The spectral radiometer itself was calibrated against a specially-constructed steel blackbody cavity mounted within a MoSi<sub>2</sub> furnace at 1500°C (verified independently with a trusted thermocouple) and

shielded from excess oxidation by a flow of dry argon gas. The radiometer was equipped with two reflex telescopes: one with optics constructed from fused silica, the other with optics of ZnSe, which allowed measurements over the entire detectable spectrum to be made upon a target area less than 1 cm in diameter from a distance of 90 cm. The spectral radiometer itself was not air-tight, but instead featured a purge gas port through which a positive pressure of shield gas could be provided to flood the unit. The optical path from the radiometer to the RTU was contained by a length of PVC pipe which was itself outfitted with a purge gas port. To minimize the effect of atmospheric absorption due to the presence of H<sub>2</sub>O and CO<sub>2</sub> across some bands of the infrared spectrum on the measurements made in those ranges, a shield gas of dry synthetic air was flooded through the radiometer and its line of sight to the specimen for a period of no less than four hours prior to measurement, and continued throughout each measurement. A typical experiment would begin with a prepared ribbon specimen. Samples first underwent oxidation in a MoSi<sub>2</sub> furnace in stagnate air on a zirconia setter at 1500°C for 1 hour (*in situ* oxidation of the ribbons was attempted by running a ribbon with the RTU open to the atmosphere to 1400°C, but the specimens broke near the setpoint and the aforementioned higher-yield oxidation procedure was selected). The oxide coating on these samples was ground by hand from the top and bottom surfaces of the thickened regions with dry 220 grit SiC sandpaper such that an electrical connection could be achieved in the RTU (a handheld multimeter set to measure the resistance of the sample was used to check the progress of the oxide removal, with sub-ohm readings being considered indicative of a fully cleaned surface). Samples were loaded into the copper clamping system (which was periodically sanded with 220 grit SiC paper to remove trace oxidation at the contact points) and the chamber was evacuated and backfilled with

ultra-pure argon three times. The argon was then set to flow through the RTU at a typical rate of 100 cc/min, and a measurement program was prepared on the computer's proprietary software suite which controlled the radiometer and collected its data. A typical control program for the power supply system was then loaded on its controlling computer: linear power ramp to pyrometer detection range (1000°C), then 200°C per minute to 1200°C, and a dwell period of 60 minutes before a transition to zero power instruction. The overhead lights in the room were lowered both to limit signal pollution and to allow for better observation of the sample through the auxiliary viewport of the RTU in order to anticipate or troubleshoot failures.

Most ribbon specimens which were tested over the course of this project failed during heating to the setpoint. More cautious heating rates (30°C/min from pyrometer control to setpoint) were attempted, but did not yield a lower specimen mortality rate; the cause of failure is believed to have been associated with defects within the specimens resulting in regions of uneven heating which then led to local thermal shock cracking which quickly resulted in catastrophic failure. Emittance measurements were not begun until the specimens had attained a temperature within 3°C of the specified setpoint (the control system was found to reliably hold the observed specimen temperature to within this range of the setpoint during steady operation). Due to the changing nature of the surfaces, identical measurements were conducted one after the other to characterize any changes over the time at temperature.

## ***5.2 Results and Discussion***

Spectral radiosity measurements were performed in two separate batches corresponding to the availability of machined ribbon specimens. Due to unexpected damage to the original control pyrometer necessitating lengthy repairs,

the first batch of measurements were performed under the control of a different pyrometer than that which was used for the second batch (the first batch pyrometer being a unit on loan from the distributor). The make, model, and settings of the pyrometers were identical, however the calibrations of the two units, performed by the supplier, were seemingly different. Figure 35 shows the spectra from 1-6  $\mu\text{m}$  of two similarly-oxidized ZBS10 ribbons held at a pyrometer-reported temperature of 1200°C. Attempts to independently measure the temperature of the incandescent ribbon samples by means of a thermocouple were thwarted both by inadequate thermal contact between the weld point and the ribbon to be measured, as well as a reaction between the metal leads of the thermocouple and the oxide surface at temperature.

A less-independent measure of actual ribbon temperature can be made using Wien’s displacement law,

$$\lambda_{max} = \frac{b}{T} \tag{12}$$

Wherein  $\lambda_{max}$  is the peak wavelength, b Wien’s displacement constant (here 2897768.5 nm·K), and T the absolute temperature.

While Wien’s displacement law assumes blackbody or greybody behavior with constant emittance, the resulting deviation is slight ( $\sim 5^\circ\text{C}$  at the temperatures considered) if the slope of the emittance is modest at and around the wavelength of peak radiance,  $\lambda_{max}$ . Assuming applicability of Wien’s displacement law for the spectra collected at a pyrometer-reported temperature of 1200°C, the spectra collected in the first batch indeed indicates a temperature of  $\sim 1200^\circ\text{C}$  ( $\lambda_{max} \sim 1.97\mu\text{m}$ ), while the spectra collected in the second batch indicate a temperature of  $\sim 1220^\circ\text{C}$  ( $\lambda_{max} \sim 1.94\mu\text{m}$ ). Figure 36 displays these data beneath the respective blackbody values as described by the Planck equation for the temperatures indicated. The spectral emittance values, calculated

as a ratio of observed radiance to that of a blackbody at equal temperature, are displayed among Figures 37, 38, and 39. These figures indicate a good correspondence between the data gathered across the two batches for the 1200 and 1300°C-range specimens (data were not collected at 1100°C in the first batch).

Countering the effect of the increasing emittance with wavelength is an observed decline in emittance over time, as evidenced by the lower radiance values of the secondary runs from the second batch. All data presented were collected under a flowing Ar atmosphere, within which the borosilicate oxide layer is unstable. At each temperature, the two emittance datasets were collected over the course of a single heating of a newly oxidized ZBS10 ribbon. Two identical data collection programs were run by the spectral radiometer, each lasting  $\sim 30$  min and occurring immediately one after the other. Comparison of the differences in emittance between these two runs (Fig 40) reveals a fairly constant drop of magnitude  $\sim 0.02$  in emittance between the first and second observations at 1120°C,  $\sim 0.015$  at 1220°C, and  $\sim 0.01$  at 1330°C. The alteration of the emitting surfaces of the ribbon specimens is evident in optical cross-sections shown in Figure 41. As the time span between measurement at each wavelength value was effectively equal, an effectively constant drop in the emittance is indicative of an overall consistent, linear decline in emittance with time at the temperatures considered. Assuming a linear drop in emittance at the constant rates displayed by the traces in Figure 40, spectral emittance plots may be modified to account for the decline in emittance values, which models the anticipated spectrum of a specimen not undergoing loss of its borosilicate layer. The results of this correction are displayed in Figures 42, 43, and 44. Error bars have been placed upon the data points to acknowledge the aforementioned uncertainty in precisely determining temperature.

Observations at higher temperatures were attempted, but the entirety of the borosilicate oxide layers was apparently lost from the ribbon surfaces over the course of the 60 min holds at pyrometer-reported temperatures of "1400" and "1500"°C, resulting in significant change to the spectral emittance over time, which serves to invalidate any attempt at accurate temperature determination by optical examination. The lack of a borosilicate layer upon the specimens which received such heat treatment is suggested by the absence of a specularly-reflecting characteristic of their surfaces (as shown in Figure 45) and an absence of such a layer in optical micrographs of their cross sections (Figure 46, as compared to the samples in Figure 41). A striking difference is evident in the comparison of XRD spectra taken from the hot zone surfaces of the ribbons (Figure 47), which suggests a complete lack of an amorphous phase upon the specimens heat treated at the two highest temperatures.

### ***5.3 Conclusions***

Due to unanticipated difficulties encountered with the data collected from the Ribbon Testing Unit as well as unexpectedly low yields of usable ribbon specimens, the results of this portion of the overall research project failed to meet many of the objectives which had been outlined in the proposal of this work, which called for a precise determination of spectral emittance from a variety of compositions from the thermogravimetric portion of the study. Despite these shortcomings, the data which were generated and interpreted do demonstrate that the most successful composition identified by the oxidation studies, ZBS10, when oxidized, has a fairly high value of emittance as compared to those reported in the literature for the constituents of the oxide layer. The high, near-grey emittance appears to result from the rough zirconia structures supported within the borosilicate matrix which forms the oxide scale, as

loss of the borosilicate is commensurate with a decline in observed emittance.

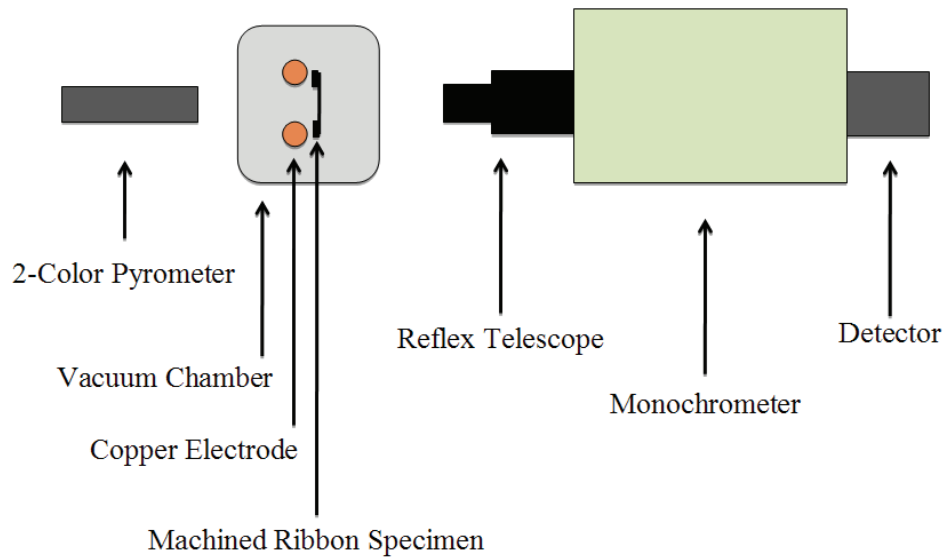


**Figure 34:** Schematic of experimental setup for thermal emittance experiments.

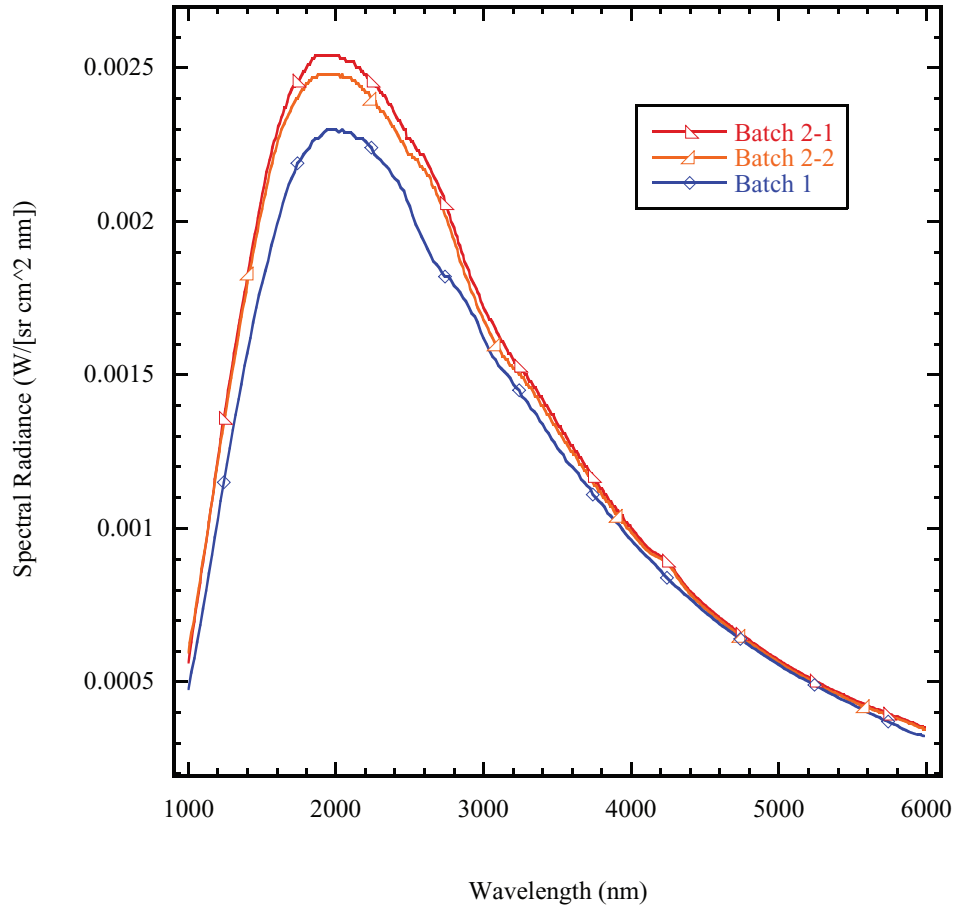


**Figure 35:** Experimental data taken from two ZBS10-composition ribbons at a pyrometer-reported temperature of 1200°C. Symbols are meaningless save to identify the curves; the resolution of the Batch 1 scan is 20 nm, the Batch 2 scans 10 nm. For both batches, a newly oxidized specimen was used, so the discrepancies in these results are indicative of change elsewhere in the experimental setup.

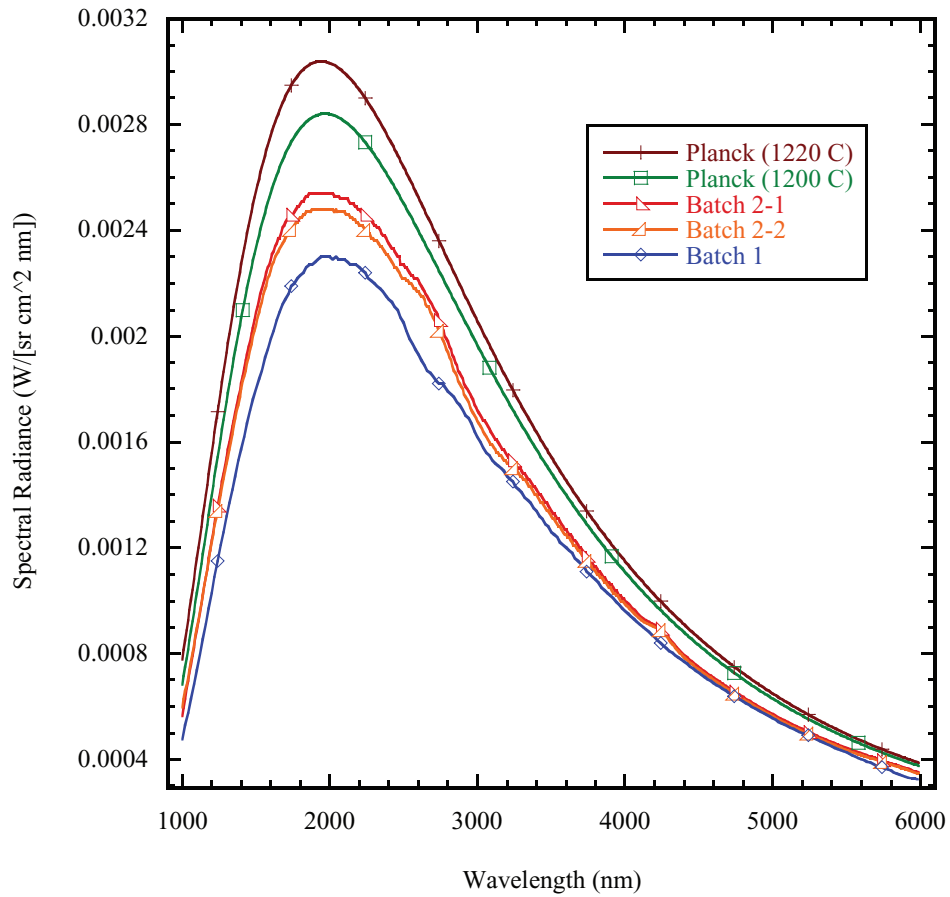


**Figure 36:** Experimental data curves from oxidized ZBS10-composition ribbons are shown beneath the calculated blackbody emittance curves as given by the Planck equation for the indicated temperatures, 1220 and 1200°C, which correspond to the Wien’s displacement law-derived temperatures for the Batch 2 and Batch 1 ribbons, respectively. Symbols are meaningless save to identify the curves; the resolution of the Batch 1 data is 20 nm, and that of the Batch 2 data is 10 nm.

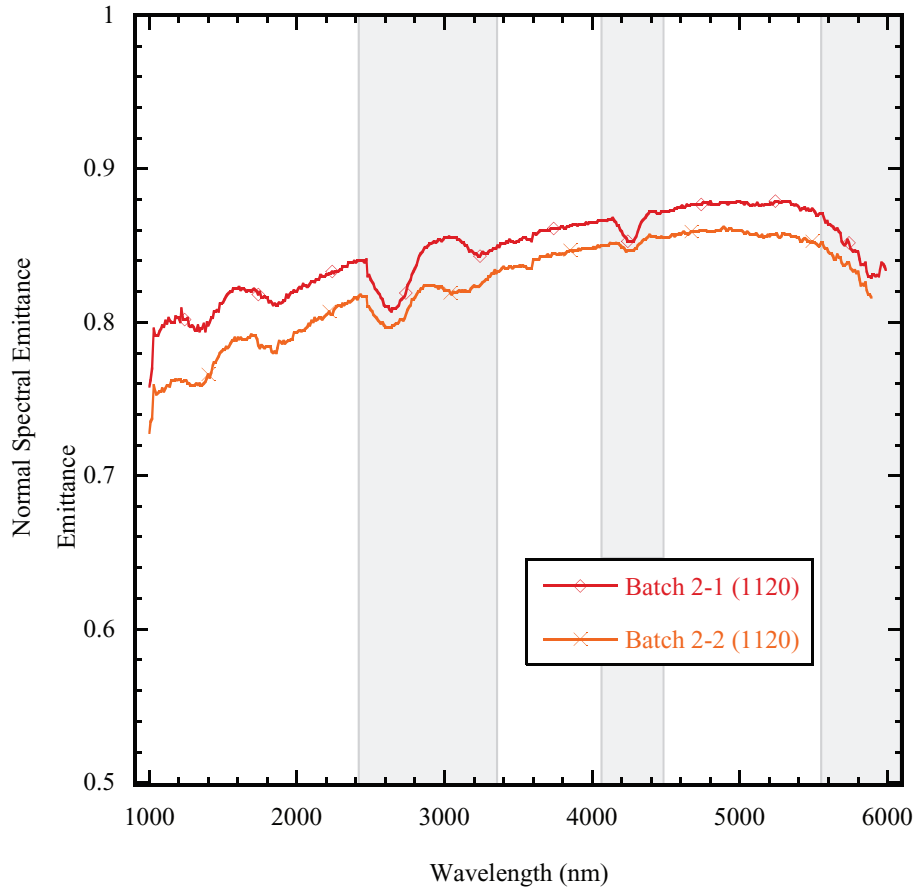


**Figure 37:** Emittance values calculated by dividing the experimental data values of spectral radiance from the oxidized ZBS10-composition ribbon held at a pyrometer-reported temperature of 1100°C by the spectral radiance values of a blackbody at 1120°C obtained from the Planck equation. Shaded regions indicate wavelength ranges where atmospheric interference due to the absorption characteristics of CO<sub>2</sub> and H<sub>2</sub>O perturbed the data (positive displacement due to differences in experimental conditions with those of the calibration scan). Symbols are meaningless save to identify the curves; the resolution of the data is 10 nm.

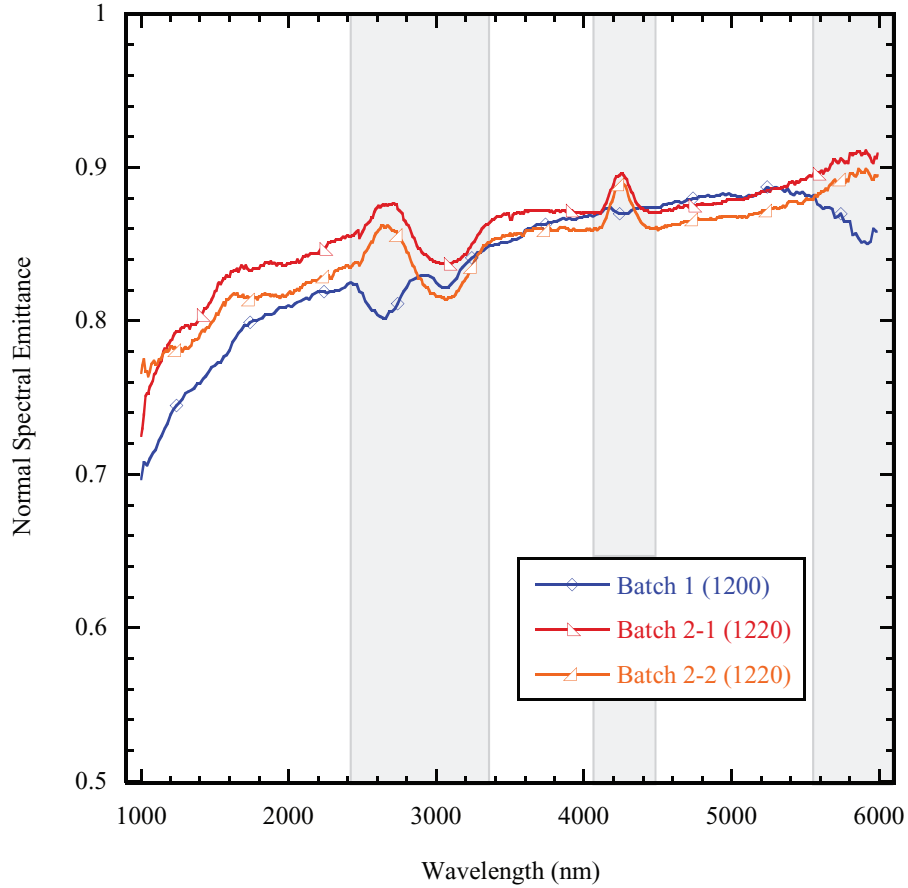


**Figure 38:** Emittance values calculated by dividing the experimental data values of spectral radiance from the oxidized ZBS10-composition ribbons held at pyrometer-reported temperatures of 1200°C by the spectral radiance values of a blackbody at the temperatures indicated by applying Wien’s displacement law to the experimental spectra. Shaded regions indicate wavelength ranges where atmospheric interference due to the absorption characteristics of CO<sub>2</sub> and H<sub>2</sub>O perturbed the data (positive displacement due to differences in experimental conditions with those of the calibration scan). Symbols are meaningless save to identify the curves; the resolution of the Batch 1 data is 20 nm, and that of the Batch 2 data is 10 nm.

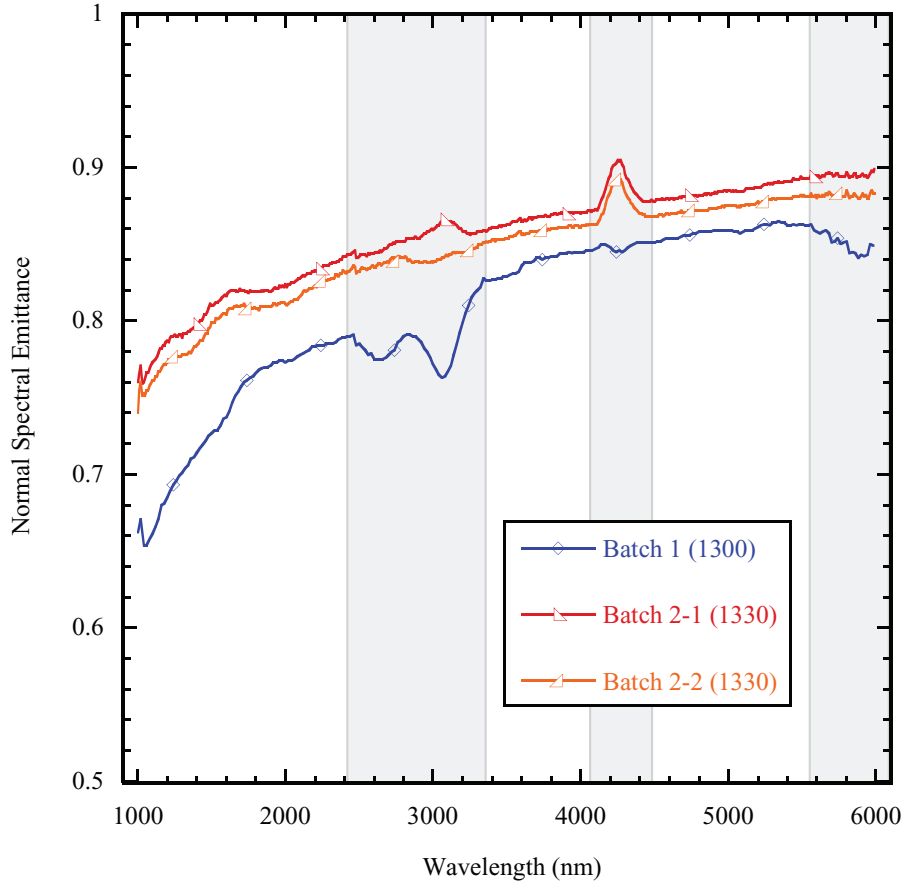


**Figure 39:** Emittance values calculated by dividing the experimental data values of spectral radiance from the oxidized ZBS10-composition ribbons held at pyrometer-reported temperatures of 1300°C by the spectral radiance values of a blackbody at the temperatures indicated by applying Wien’s displacement law to the experimental spectra. Shaded regions indicate wavelength ranges where atmospheric interference due to the absorption characteristics of CO<sub>2</sub> and H<sub>2</sub>O perturbed the data (positive displacement due to differences in experimental conditions with those of the calibration scan). Symbols are meaningless save to identify the curves; the resolution of the Batch 1 data is 20 nm, and that of the Batch 2 data is 10 nm..

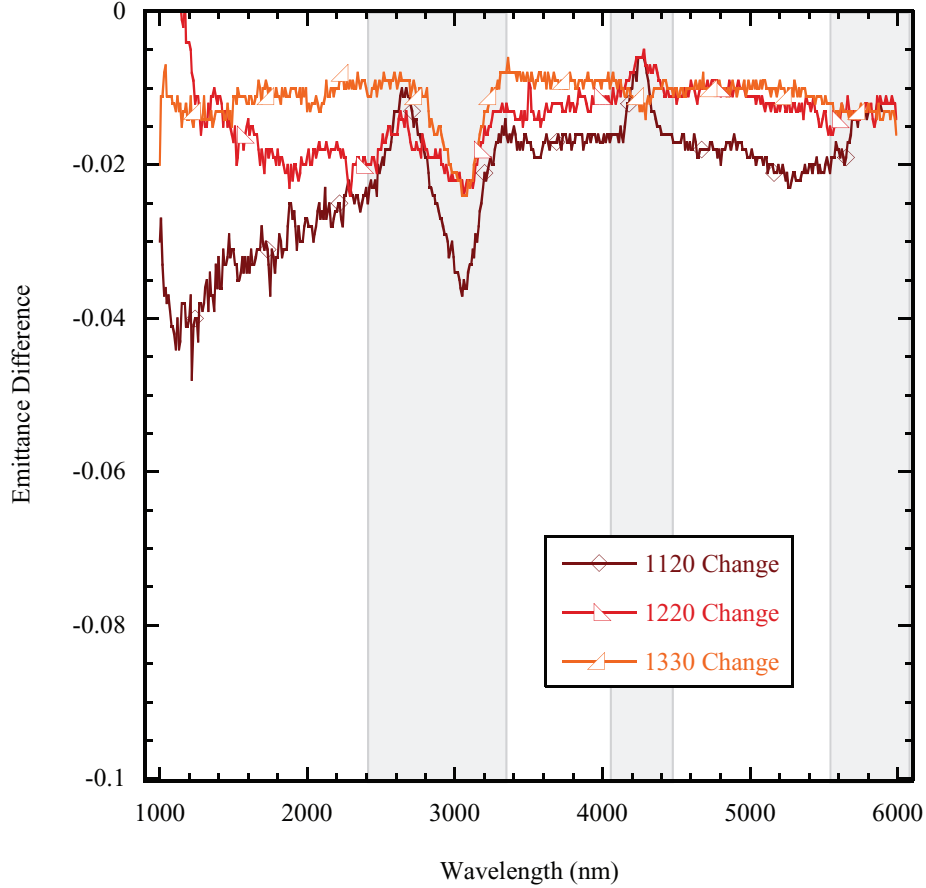


**Figure 40:** Differences in the observed emittance values obtained during the subsequent observations of the second batch of oxidized ribbons held at the apparent temperatures of 1120, 1220, and 1330°C. Data points obtained by subtracting the emittance values of the first observation from those of the second; the difference corresponds to the change in apparent spectral emittance after  $\sim 30$  min at the indicated temperature. Shaded regions indicate wavelength ranges where atmospheric interference due to the absorption characteristics of  $\text{CO}_2$  and  $\text{H}_2\text{O}$  perturbed the data (positive displacement due to differences in experimental conditions with those of the calibration scan). Symbols are meaningless save to identify the curves; the resolution of the data is 10 nm.

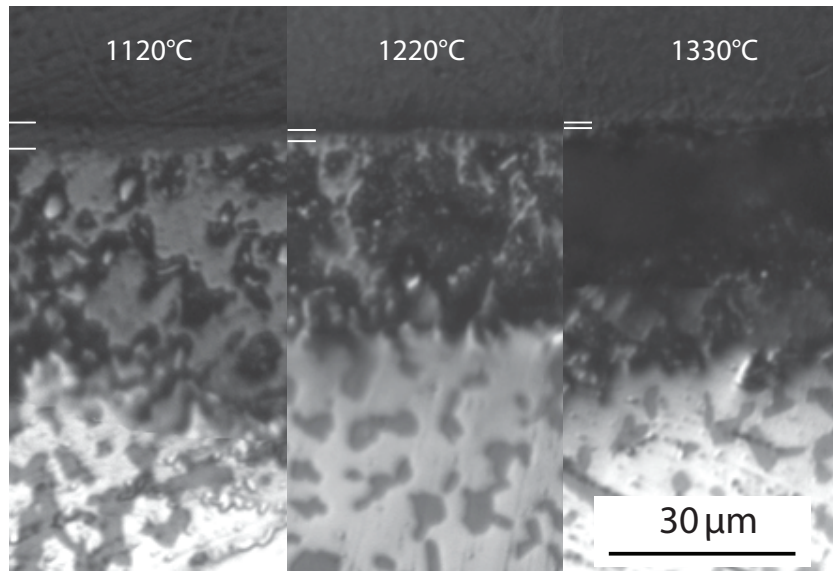


**Figure 41:** Optical micrographs of polished cross-sections of the ribbon specimens held for 60 min at the indicated temperatures. The untransformed bulk is visible as the bright region at the base of the images. The Si-depleted zone sits above the untransformed bulk. White hatch marks on the left hand side of the images denote the regions of observed borosilicate glass. The region above these hatch marks consists of the resin used to support the specimens during polishing.

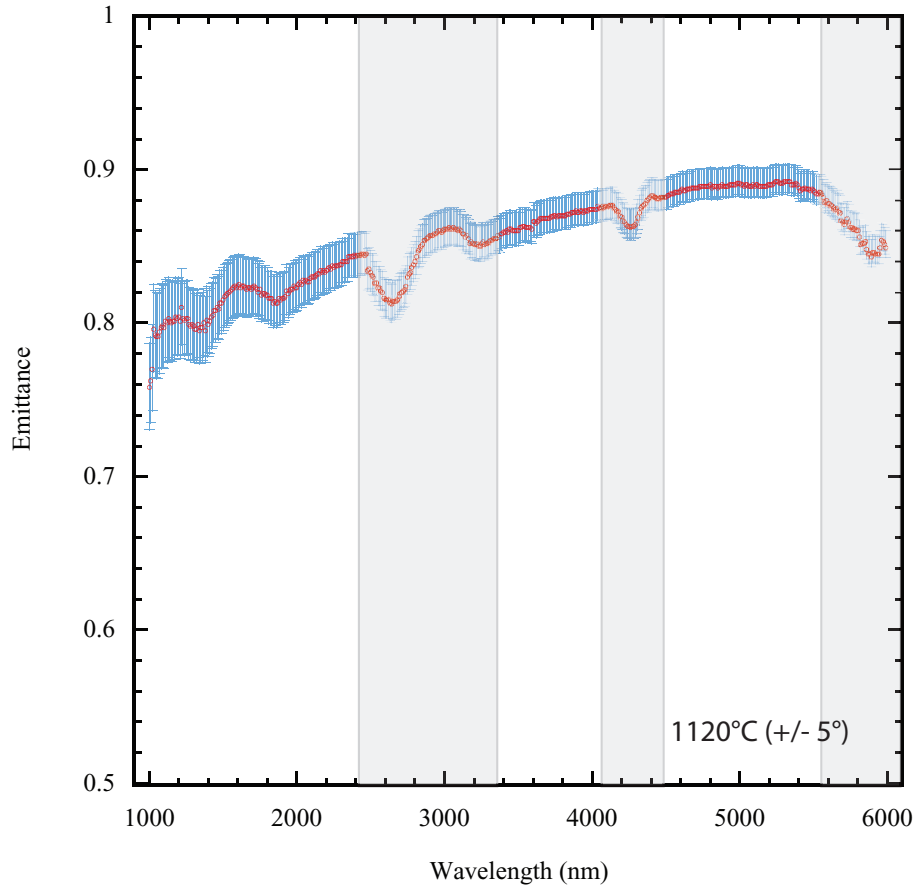


**Figure 42:** Individual data points shown indicate the spectral emittance values observed during the first instance of data collection from an oxidized ZBS10-composition ribbon at  $1120^{\circ}\text{C}$  plus a linear rise of magnitude 0.02 over the range of  $1\text{-}6\ \mu\text{m}$  in accordance with the decline in emittance observed by comparison with the second instance of data collection. Upper and lower error bars indicate the change to these data should the assumed temperature be lowered or raised by  $5^{\circ}\text{C}$ , respectively. Shaded regions indicate wavelength ranges where atmospheric interference due to the absorption characteristics of  $\text{CO}_2$  and  $\text{H}_2\text{O}$  perturbed the data (positive displacement due to differences in experimental conditions with those of the calibration scan).

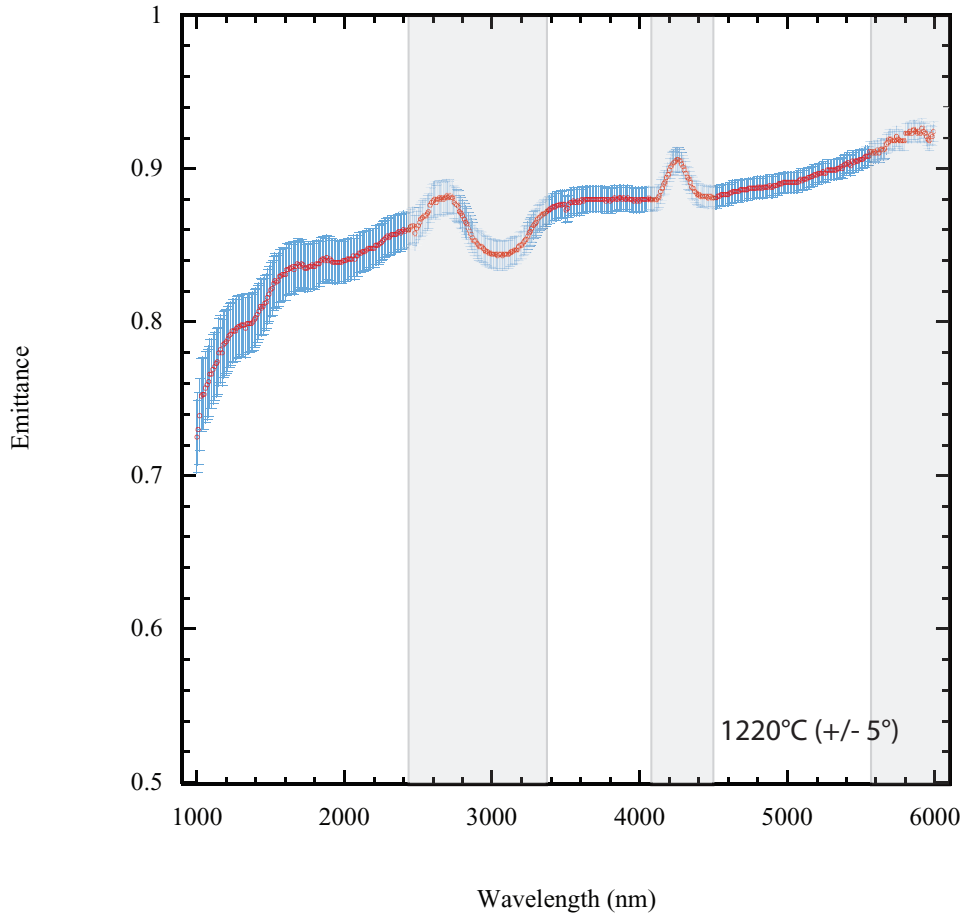


**Figure 43:** Individual data points shown indicate the spectral emittance values observed during the first instance of data collection from an oxidized ZBS10-composition ribbon at 1220°C plus a linear rise of magnitude 0.015 over the range of 1-6  $\mu\text{m}$  in accordance with the decline in emittance observed by comparison with the second instance of data collection. Upper and lower error bars indicate the change to these data should the assumed temperature be lowered or raised by 5°C, respectively. Shaded regions indicate wavelength ranges where atmospheric interference due to the absorption characteristics of  $\text{CO}_2$  and  $\text{H}_2\text{O}$  perturbed the data (positive displacement due to differences in experimental conditions with those of the calibration scan).

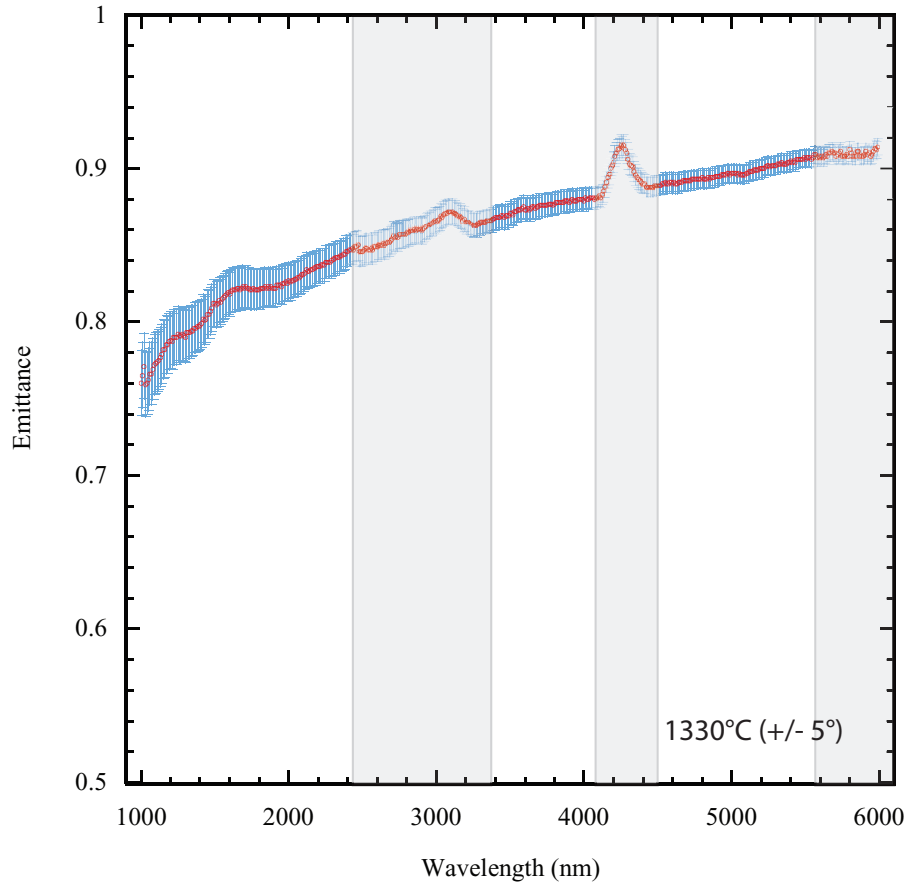


**Figure 44:** Individual data points shown indicate the spectral emittance values observed during the first instance of data collection from an oxidized ZBS10-composition ribbon at 1330°C plus a linear rise of magnitude 0.01 over the range of 1-6  $\mu\text{m}$  in accordance with the decline in emittance observed by comparison with the second instance of data collection. Upper and lower error bars indicate the change to these data should the assumed temperature be lowered or raised by 5°C, respectively. Shaded regions indicate wavelength ranges where atmospheric interference due to the absorption characteristics of  $\text{CO}_2$  and  $\text{H}_2\text{O}$  perturbed the data (positive displacement due to differences in experimental conditions with those of the calibration scan).

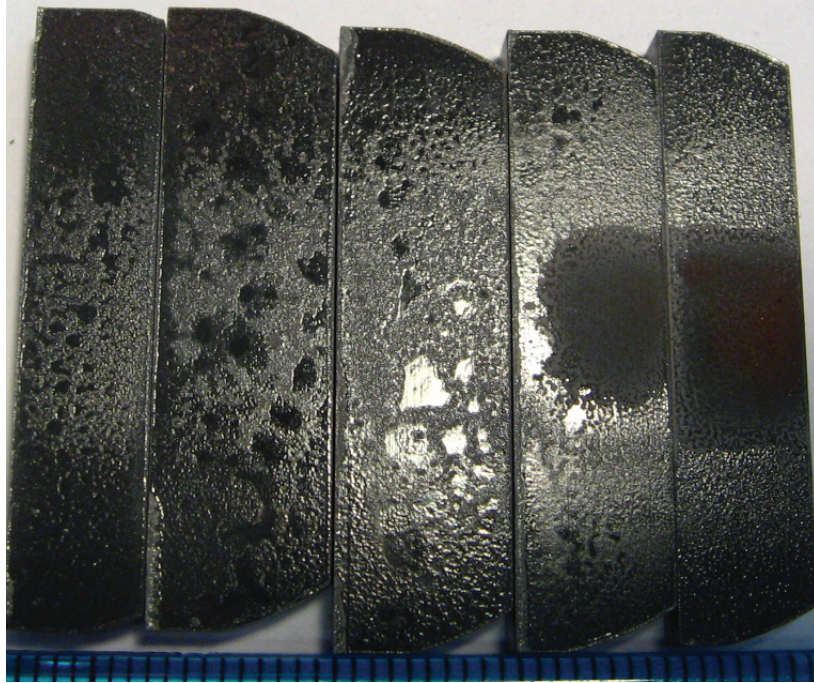


**Figure 45:** Photograph of the observed "front" surfaces of the post-heat-treated ribbon specimens from Batch 2. From left to right, the pyrometer-reported temperatures whereat each specimen was held for 60 min in flowing Ar are 1100, 1200, 1300, 1400, and 1500°C. Note the lack of specular reflection from the central portions of the ribbons held at the two highest temperatures. The marks on the ruler at the base of the image are 1 mm apart.

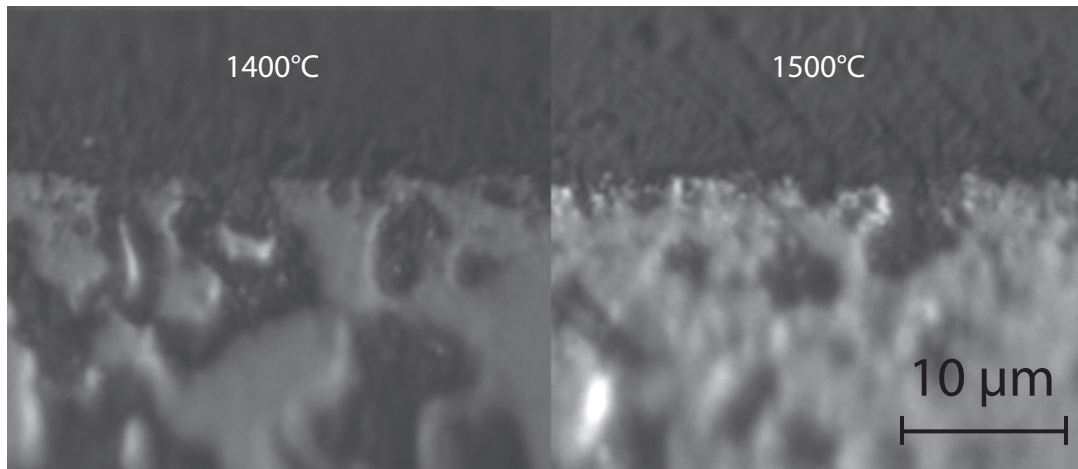


**Figure 46:** Optical micrographs of polished cross-sections of the ribbon specimens held for 60 min at the indicated pyrometer-reported temperatures. The untransformed bulk is visible as the bright region at the base of the images. The Si-depleted zone sits above the untransformed bulk. For these temperatures, there is no observed borosilicate glass. The region above the Si-depleted zone consists of the resin used to support the specimens during polishing.

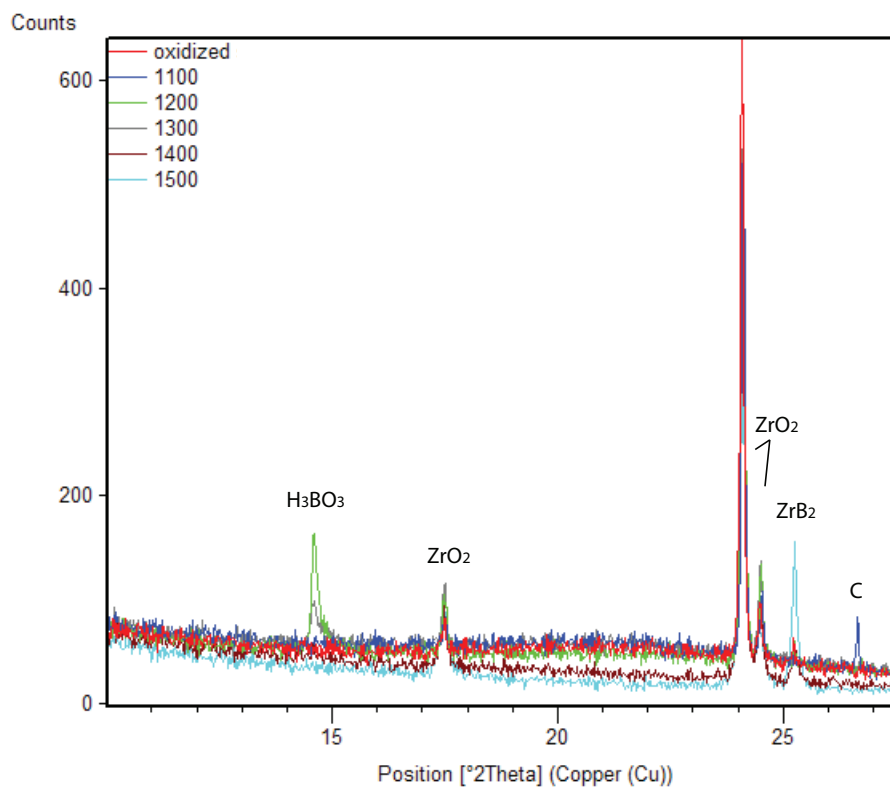


**Figure 47:** Portion of the XRD spectra taken from the hot zones of the second batch of heat-treated, oxidized ZBS10-composition ribbons, identified here by their pyrometer-reported dwell temperatures in degrees Centigrade, as well as a scan of an oxidized ZBS10-composition ribbon having not undergone heat treatment in the RTU. Note the presence of a slight amorphous hump for all specimens except the two held at the highest temperatures for the 60 min dwell.

## REFERENCES

- [1] R. Loehman, *et al.*, “Ultra High Temperature Ceramics for Hypersonic Vehicle Applications” *Sandia Report*, SAND 2006-2925, Sandia National Laboratories, June 2006.
- [2] W. G. Fahrenholtz, G. E. Hilmas, organizers, “Draft: NSF-AFOSR Joint Workshop on Future Ultra-High Temperature Materials” *National Science Foundation Workshop*, Arlington, VA, 13-14 January 2004.
- [3] W. G. Fahrenholtz, G. E. Hilmas, I. G. Talmy, and J. A. Zaykoski, “Refractory Diborides of Zirconium and Hafnium,” *J. Am. Ceram. Soc.*, **90** [5] 1347-1364 (2007)
- [4] F. Peng and R. F. Speyer, “Oxidation Resistance of Fully Dense  $ZrB_2$  with SiC,  $TaB_2$ , and  $TaSi_2$  Additives,” *J. Am. Ceram. Soc.*, **91** [5] 1489-1494 (2008).
- [5] M. M. Opeka, I. G. Talmy, E. J. Wuchina, J. A. Zaykosi, and S. J. Causey, “Mechanical, Thermal, and Oxidation Properties of Refractory Hafnium and Zirconium Compounds,” *J. Eur. Ceram. Soc.*, **19** 2405-2414 (1999).
- [6] Touloukian, Y. S. *Thermophysical Properties of Matter: [the TPRC Data Series; a Comprehensive Compilation of Data*. New York: IFI/Plenum, 1970.

- [7] S. N. Karlsdottir, J. W. Halloran, and A. N. Grundy, "Zirconia Transport by Liquid Convection during Oxidation of Zirconium Diboride-Silicon Carbide," *J. Am. Ceram. Soc.*, **91** [1] 272-277 (2008).
- [8] M. Gash, D. Ellerby, E. Irby, S. Beckman, M. Gusman, and S. Johnson. "Processing, Properties, and Arc Jet Oxidation of Hafnium Diboride/Silicon Carbide Ultra High Temperature Ceramics," *J. Mater. Sci.*, **39** 5925-37 (2004).
- [9] H. Lee and R. F. Speyer, "Pressureless Sintering of Boron Carbide," *J. Am. Ceram. Soc.*, **86** [9] 1468-1473 (2003).
- [10] S. C. Zhang, G. E. Hilmas, and W. G. Fahrenholtz, "Pressureless Densification of Zirconium Diboride with Boron Carbide Additions." *J. Am. Ceram. Soc.*, **89** [5] 1544-1550 (2006).
- [11] A. L. Chamberlain, W. G. Fahrenholtz, and G. E. Hilmas, "Pressureless Sintering of Zirconium Diboride," *J. Am. Ceram. Soc.*, **89** [2] 450-456 (2006).
- [12] D. Sciti, M. Brach, and A. Bellosi, "Oxidation Behavior of a Pressureless Sintered  $ZrB_2$ - $MoSi_2$  Ceramic Composite," *J. Mat. Res.*, **20** [4] 922-930 (2005).
- [13] S. Guo, Y. Kagawa, T. Nishimura, and H. Tanaka, "Pressureless Sintering and Physical Properties of  $ZrB_2$ -based composites with  $ZrSi_2$  Additive," *Scripta Materialia*, **58** 579-582 (2008).
- [14] X. Zhang, P. Hu, J. Han, L. Xu, and S. Meng, "The Addition of Lanthanum Hexaboride to Zirconium Diboride for Improved Oxidation Resistance," *Scripta Mater.*, **57** 1036-39 (2007).

- [15] T. A. Parthasarathy, R. A. Rapp, M. Opeka, and R. J. Kerans, "A Model for the Oxidation of  $ZrB_2$ ,  $HfB_2$  and  $TiB_2$ ," *Acta Materialia*, **55** 5999-6010 (2007).
- [16] K. Upadhyaya, Y. Jenn-Ming, and P. H. Wesley, "Materials for Ultrahigh Temperature Structural Applications", *Am. Cer. Soc. Bull.*, (Dec. 1997).
- [17] W. C. Tripp, H. H. Davis, and H. C. Graham, "Effect of an SiC Addition on the Oxidation of  $ZrB_2$ ," *Am. Ceram. Soc. Bull.*, **52** [8] 612-616 (1973).
- [18] A. Rezaie, W. G. Fahrenholtz, and G. E. Hilmas, "Evolution of Structure During the Oxidation of Zirconium Diboride in Air up to 1500°C," *J. Europ. Ceram. Soc.*, **27** 2495-2501 (2007).
- [19] F. J. Norton, "Permeation of Gaseous Oxygen through Vitreous Silica". *Nature*, **191**, 701 (1961).
- [20] J. A. Costello, R. E. Tressler, "Isotope Labeling Studies of the Oxidation of Silicon at 1000° and 1300°C", *J. Electrochem. Soc.*, **131**, pp. 1944 (1984).
- [21] R. H. Doremus, "Diffusion of Oxygen in Silica Glass", *J. Electrochem. Soc.*, **143**, 6, pp 1992 (1996).
- [22] J. Berkowitz-Mattuck, "High-Temperature Oxidation, Part III. Zirconium and Hafnium Diborides," *J. Electrochem. Soc.*, **113**, No. 9, pp908-14 (1966).
- [23] M. Schütze, *Protective Oxide Scales and Their Breakdown*, John Wiley & Sons, New York, 1997.
- [24] E. J. Opila, M. C. Halbig, "Oxidation of  $ZrB_2$ -SiC," *Ceram. Eng. Sci. Proc.*, **22** [3] 221-228 (2001).

- [25] F. Peng and R. F. Speyer, Unpublished work, 2008.
- [26] J. Han, P. Hu, X. Zhang, and S. Meng, "Oxidation Behavior of Zirconium Diboride-Silicon Carbide at 1800°C," *Scripta Mater.*, **57** 825-828 (2007).
- [27] A. Rezaie, W. G. Fahrenholtz, and G. E. Hilmas, "Oxidation of Zirconium Diboride-Silicon Carbide at 1500°C in a Low Partial Pressure of Oxygen," *J. Am. Ceram. Soc.*, **89** [10] 3240-45 (2006).
- [28] W. G. Fahrenholtz, "Thermodynamic Analysis of ZrB<sub>2</sub>-SiC Oxidation: Formation of a SiC-Depleted Region," *J. Am. Ceram. Soc.*, **90** [1] 143-148 (2007).
- [29] M. Opeka, I. Talmy, J. Zaykoski, "Oxidation-based Materials Selection for 2000°C + Hypersonic Aerosurfaces: Theoretical Considerations and Historical Experience," *J. Mater. Sci.*, **39** [19] 5887-5904 (2004)
- [30] Q. N. Nguyen, E. J. Opila, and R. C. Robinson, "Oxidation of Ultrahigh Temperature Ceramics in Water Vapor," *J. Electrochem. Soc.*, **151** [10] B558-B562 (2004).
- [31] I. G. Talmy, J. A. Zaykoski, M. M. Opeka, S. Dallek, "Oxidation of ZrB<sub>2</sub> Ceramics Modified with SiC and Group IV-VI Transition Metal Diborides," *Elec. Chem. Soc. Proc.*, **12** 144-158 (2001).
- [32] E. J. Opila, S. Levine, J. Lorincz, "Oxidation of ZrB<sub>2</sub>- and HfB<sub>2</sub>-based Ultra-high Temperature Ceramics: Effect of Ta Additions," *J. Mater. Sci.*, **39** [19] 5969-5977 (2004).
- [33] I. G. Talmy, J. A. Zaykoski, M. M. Opeka, and A. H. Smith, "Properties of Ceramics in the System ZrB<sub>2</sub>-Ta<sub>5</sub>Si<sub>3</sub>," *J. Mater. Res.*, **21** [10] 2593-99 (2006).

- [34] F. Peng, G. Van Laningham, and R. F. Speyer, "Thermogravimetric analysis of the oxidation resistance of  $ZrB_2$ -SiC and  $ZrB_2$ -SiC-TaB<sub>2</sub>-based compositions in the 1500–1900°C range," *J. Mater. Res.*, **26**, 1 (14 January 2011).
- [35] M. Gash, D. Ellerby, E. Irby, S. Beckman, M. Gusman, and S. Johnson. "Processing, Properties, and Arc Jet Oxidation of Hafnium Diboride/Silicon Carbide Ultra High Temperature Ceramics," *J. Mater. Sci.*, **39** 5925-37 (2004).
- [36] S. C. Zhang, G. E. Hilmas, and W. G. Fahrenholtz, "Pressureless Sintering of  $ZrB_2$  Ceramics," *J. Am. Ceram. Soc.* **91** [1] 26-32 (2008).
- [37] Y. S. Touloukian, *Thermophysical Properties of Matter*, Vols. 1 and 2, Plenum Press, New York, 1970.
- [38] G. Grimvall, *Thermophysical Properties of Materials*, Elsevier Science Pub. Co. Inc., New York, 1986.
- [39] W. D. Kingery, H. K. Bowman, and D. R. Uhlmann, *Introduction to Ceramics*, John Wiley and Sons, New York, 1976.
- [40] R. F. Speyer, *Thermal Analysis of Materials*, Marcel Dekker, New York, 1994.
- [41] L. Scatteia, D. Alfano, F. Monteverde, J. Sans, and M. Balat-Pichelin. "Effect of the Machining Method on the Catalycity and Emissivity of  $ZrB_2$  and  $ZrB_2$ -HfB<sub>2</sub>-Based Ceramics," *J. Am. Ceram. Soc.*, **91** [5] 1461-8 (2008).

- [42] R. J. Parker, R. J. Butler, C. P. Butler, and G. I. Abbott, "A Flash Method of Determining Thermal Diffusivity, Heat Capacity, and Thermal Conductivity," *J. Appl. Phys.*, **32** 1679-1684 (1961) .
- [43] T. R. Lee, Ph. D. Thesis, "Thermal Diffusivity of Dispersed and Layered Composites," Purdue University, University Microfilms International, 1977.
- [44] J. N. Sweet, "Data Analysis Methods for Flash Thermal Diffusivity Experiments," Sandia National Laboratories Report SAND89-0260 US-25, 1989.
- [45] M. W. Chase, Jr., Ed., *NIST-JANAF Thermochemical Tables*, 4th Ed., Monograph No. 9, Parts I and II, American Institute of Physics, Woodbury, NY, 1998.
- [46] D. R. Lide, Ed., *CRC Handbook of Chemistry and Physics*, 81st Ed., CRC Press, Boca Raton, FL (2001).
- [47] F. G. Keihn and E. J. Keplin, "High-Temperature Thermal Expansion of Certain Group IV and Group V Diboides," *J. Am. Ceram. Soc.*, **50** [2] 81-84 (1967).
- [48] R. G. Munro, "Material Properties of a Sintered  $\alpha$ -SiC," *J. Phys. Chem. Ref. Data*, **26** [5] 1195-1203 (1997).
- [49] G. V. Tsagareishvili, T. G. Nakashidze, J. S. Jobava, G. P. Lomidze, D. E. Khulelidze, D. Sh. Tsagareishvili, and O. A. Tsagareishvili, "Thermal Expansion of Boron and Boron Carbide," *J. of the Less-Common Metals*, **117** [1-2] 159-161 (1986).

- [50] K. Watari, H. Nakano, K. Sato, K. Urabe, K. Ishizaki, S. Cao, and K. Mori, "Effect of Grain Boundaries on Thermal Conductivity of Silicon Carbide Ceramic at 5 to 1300 K," *J. Am. Ceram. Soc.*, **86** [10] 1812-14 (2003).
- [51] G.A. Slack, "Thermal Conductivity of Pure and Impure Silicon, Silicon Carbide, and Diamond," *J. Appl. Phys.*, **35** 3460-66 (1964).
- [52] D.-M. Liu and B.-W. Lin, "Thermal Conductivity in Hot-Pressed Silicon Carbide," *Ceram. Int.*, **22**407-414 (1996).
- [53] M. Bouchacourt and F. Thevenot, "The Correlation Between the Thermoelectric Properties and Stoichiometry in the Boron Carbide Phase  $B_4C-B_{10.5}C$ ," *J. Mater. Sci.*, **20** 1237-1247 (1985).
- [54] K. E. Gilchrist and S. D. Preston: "Thermophysical Property Measurements on Some Neutron Absorbing Materials," *High Temp. High Press.*, **11** 643651 (1979).
- [55] Y. Nishi, Y. Arita, T. Matsui, and T. Nagasaki, "Isotope Effects on Thermal Conductivity of Boron Carbide," *J. Nuc. Sci.*, **39** [4] 391-394 (2002).
- [56] C. Wood, D. Emin, and P. E. Gray, "Thermal Conductivity of Boron Carbides," *Phys. Rev. B*, **31** 6811-6814 (1985).
- [57] R. P. Tye, and E. V. Clougherty, "The Thermal and Electrical Conductivities of Some Electrically Conducting Compounds," *Proceedings of the Fifth Symposium on Thermophysical Properties*, Newton, MA, September 30 - October 2, 396-401, 1970.

- [58] J. W. Zimmermann, G. E. Hilmas, W. G. Fahrenholtz, R. B. Dinwiddie, W. D. Porter, and H. Wang, "Thermophysical Properties of ZrB<sub>2</sub> and ZrB<sub>2</sub>-SiC Ceramics," *J. Am. Ceram. Soc.*, **91** [5] 1405-1411 (2008).
- [59] F. P. Incropera and D. P. DeWitt, *Fundamentals of Heat and Mass Transfer*, John Wiley and Sons, New York, 2002.
- [60] Smith, A.L., *The Coblenz Society Desk Book of Infrared Spectra, Second Edition*, The Coblenz Society: Kirkwood, MO (1982).

## VITA

Gregg Thomas Van Laningham was born 12 March, 1985, in Huntsville, Alabama. He came to a suburb of Atlanta, Georgia, at the age of four and, throughout his childhood and teenage years, desired to attend the Georgia Institute of Technology. He graduated from Parkview High School in Lilburn, Georgia, in May of 2003, and that Fall began undergraduate studies at Georgia Tech in the School of Materials Science and Engineering. In May of 2007, he earned his B.S. with highest honors. He spent the Summer of 2007 working in the laboratory of Dr. Robert Speyer, and that Fall began the graduate studies which would eventually lead to this dissertation.

As of the publication of this tome, Gregg lives in Atlanta, Georgia, with a cat named Buster and a dog named Gus.